Investigation of the unusual magnetic properties of hemo-ilmenite by neutron scattering

Master thesis

Erik Brok
Niels Bohr Institute
University of Copenhagen

December 1st, 2009

Resumé på dansk

I dette speciale undersøges de bemærkelsesværdige magnetiske egenskaber af hemo-ilmenit ($\alpha-Fe_2O_3$-$FeTiO_3$) med polariseret neutronspredning med et treaksespektrometer (TASP) og polariseret småvinkel neutronspredning (SANSPOL) på et stykke hemo-imlenit klippe fra de Norske fjelde. Resultaterne fra TASP eksperimentet viser at de cantede-antiferromagnetiske (CAFM) hæmatitspin drejer væk fra et påtryk felt og ikke når en mætning i felter op til 2 T. Dette er i modstrid med en model der kun tager højde for lamellar magnetisme. SANSPOL eksperimentet viser et hysteresesignal der mætter i et felt på omkring 0.5 T, hvilket er i overensstemmelse med magnetiseringsmålinger. At de magnetiske momenter vi ser i TASP eksperimentet ikke følger samme hysterese som magnetiseringsmålingerne antyder at det ikke er de samme momenter, som er ansvarlige for den høje magnetisering i hemo-ilmenit. Hvor vi, i TASP eksperimentet, ser rotationen af CAFM momenter, er det muligvis de lamellare momenter der ses i det magnetiske signal fra SANSPOL eksperimentet. I TASP eksperimentet observerede vi også et ferromagnetisk signal, som muligvis kommer fra de magnetiske momenter der er ansvarlige for den remanente magnetisering. På grund af kombinationen af dårlig opløsning i eksperimentet, dårligt kendskab til polarisationen i eksperimentet og prøvens sammensatte natur var det ikke muligt at få præcis information om dette signal. Det ville derfor være interessant at lave et nyt TASP eksperiment med bedre kollimering og kontrol af polarisationen. SANSPOL eksperimentet led under, at der ikke var en spin flipper monteret på instrumentet og af dårlig reproducerbarhed i data når polarisatoren blev taget ud og ind af beamet. Hvis et nyt SANSPOL eksperiment med spin flipper gennemføres vil der, på baggrund af det foreliggende eksperiment, være gode muligheder for at få afgørende information om de magnetiske strukturer i prøven.

Erik Brok
1. december 2009

Abstract

In this thesis the unusual magnetic properties of hemo-ilmenite ($\alpha-\mathrm{Fe_2O_3}$-$\mathrm{FeTiO_3}$) is investigated with polarised neutron scattering with a triple-axis spectrometer (TASP) and polarised small angle neutron scattering (SANSPOL) on a piece of hemo-ilmenite rock from Norway. The results from the TASP experiment show that the canted-antiferromagnetic hematite spins are rotating away from an applied field and is not saturated in fields up to 2 T. This is not in agreement with a model with only lamellar magnetism. The SANSPOL experiment shows a hysteresis signal that saturates in a field of about 0.5 T which is in agreement with magnetization measurements. The fact that the magnetic moments we see in the TASP experiment does not follow the same hysteresis as the magnetization measurements suggests that it is not the same moments as the ones responsible for the high magnetization of hemo-ilmenite. Where the TASP experiment shows the rotation of the CAFM moments the magnetic signal from the SANSPOL experiment may be an observation of the lamellar moments. In the TASP experiment we further observed a ferromagnetic signal which may come from the magnetic moments that are responsible for the remanent magnetization. Because of a combination of bad instrumental resolution, poor knowledge about the polarisation in th experiment and the complex nature of the sample it was not possible to get accurate information about this signal. It would therefore be interesting to perform a new TASP experiment with better collimation and polarisation control. The SANSPOL experiment suffered from the absence of a spin flipper on the instrument and from poor reproducibility when the polariser was taken in and out of the beam. Based on the present SANSPOL experiment it seems promising to perform a new experiment with a spin flipper in order to get information about the magnetic structures in the sample.

Erik Brok
december 1st, 2009

Contents

Chapter 1

Introduction

The mineral hemo-ilmenite is known to give an important contribution to anomalies in the magnetic field of the Earth. This is surprising because it is not obvious that hemo-ilmenite should show a net magnetic moment at all. The mineral consists of hematite, which is an antiferromagnet, and ilmenite, which is a paramagnet in the relevant temperature regime. These two magnetic structures together should not be able to produce a net magnetic moment. Understanding the magnetic properties of hemo-ilmenite is thus interesting from a geomagnetic, as well as a more fundamental physical point of view. Hemo-ilmenite rocks from Norway, Sweden and North America have been collected, and a variety of experiments have been conducted and have revealed that the samples indeed have a large and very stable magnetization.

In this thesis I will present neutron scattering experiments on a hemo-ilmenite sample from Norway. From the experiments we will get information about the magnetic structure of the sample. In the remainder of this chapter I will give a brief background about anomalies in the geomagnetic field in the region where the sample was collected. In chapter 2 an introduction to some important concepts in magnetism will be given. This will be followed by a description of some important properties of hemo-ilmenite and some of the ideas that are put forward to explain the magnetic properties in chapter 3. This will also include some information about the particular sample under investigation. The relevant theory of neutron scattering, polarised neutron scattering and small angle neutron scattering will be explained in chapters 4, 5, 6 and an explanation of the instruments used in the neutron scattering experiments are given in chapter 7. The procedures for the analysis of the data from the diffraction experiment and the results of this analysis is presented in chapters 8 and 9, followed by a description of the small angle neutron scattering experiment and a presentation of some preliminary results of this in chapter 10. A discussion of the results is given in chapter 11 and finally in chapter 12 is a summary of the conclusions and an outlook. Some informations that might be irrelevant to some readers, but on the other hand might be useful for others are given in the appendices A-C.

1.1 Magnetic anomalies

The magnetic field of the Earth is generated by the motion of liquid iron in Earth's outer core. However, it is perturbed by magnetic minerals in the crust. Both positive and negative anomalies are present and are caused by different rock minerals. Positive anomalies are induced in magnetic minerals by the present magnetic field of Earth. Negative anomalies were induced at a time where the direction of the magnetic field of Earth was different and this contribution to the magnetic field is thus a remanent magnetism.

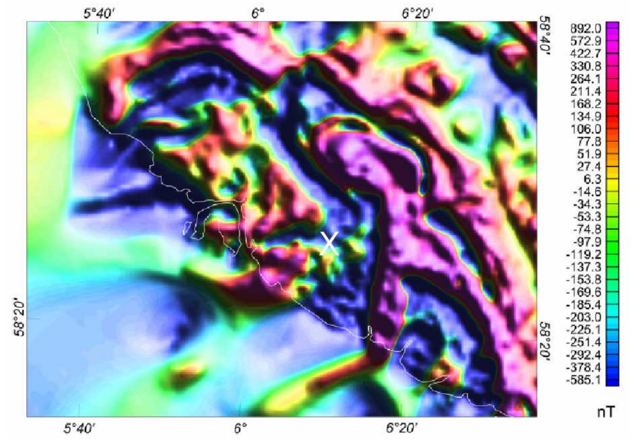

Figure 1.1: ***Aeromagnetic map of the South Rogaland region, Norway.*** *The magnetic field was measured from the air and shows large anomalies. Pink indicates strong positive anomalies (induced). Blue indicates strong negative anomalies (remanent). The approximate position of the 'Pramsknuten' dike, where our sample was collected, is marked with a white X. The white line close to the diagonal of the map is the coastline. The magnetic field is given as the difference from the IGF (1965) reference field of 52.000 μT (International Geomagnetic Reference Field). Figure from [1].*

The magnetic field in the South Rogaland region, Norway, has been measured from a small aeroplane and shows both positive (induced) and negative (remanent) anomalies. The anomalies have been mapped more precisely in a helicopter survey showing a contrast between magnetic highs and lows of about 6.000 μ T in a reported regional field of 50.027 μ T [2]. An aeromagnetic map of South Rogaland is given in fig. 1.1.

By comparison of the aeromagnetic data with detailed geological maps it is established that positive magnetic anomalies are prominently found in areas dominated by rocks containing multidomain magnetite (Fe_3O_4), whereas negative anomalies are found in areas with rocks dominated by the mineral "hemo-ilmenite" ($\alpha-Fe_2O_3$ - $FeTiO_3$). Similar observations have been made in North America. Samples from the South Rogaland region have shown a remanent magnetization of about 60 A/m [1] and the anomalies have been successfully modeled with this value [3]. Natural remanent magnetization (NRM) in rocks containing hemo-ilmenite has thus been identified as an important contribution to anomalies in the magnetic field of the Earth [4] and may well be the reason for the magnetic fields of planets like Mars that are no longer geologically active [3]. This magnetization was induced millions of years ago in magma and frozen when the magma was cooled and solidified.

The precise mechanism behind the NRM is yet unknown, but is believed to be connected to the lamellar structure of the material, which is intimately related to the exsolution process in which the hematite-ilmenite intergrowths were formed. In chapter 3 the magnetic structure of hemo-ilmenite will be discussed, as will some proposed explanations for the unusual magnetism, which I then further discuss in the analysis of the neutron data.

1.2 Acknowledgements

Before proceeding further it is time to thank all the important persons who helped me in various ways during the development of my thesis. First of all I thank my supervisors Kim Lefmann and Luise Theil Kuhn for getting me started on this project and for helping me in every stage in the development of my thesis. Further I owe thanks to Richard Harrison for participating in the experiments at TASP and SANS-I and for sharing with me his great knowledge of rock magnetism and also a special thank to Suzanne McEnroe for providing the sample without which there would have been no experiments. I thank Bertrand Roessli for taking part in the TASP experiment and for helping me calculate the resolution function of TASP. I thank Lise Arleth for helping me with the modeling of the SANSPOL experiment and the instrument responsibles of SANS-I for helping with the experiment. I am also grateful for the help of Bente Lebech with calculating structure factors and Niels Bech Christensen who helped with at several points in the data analysis.

Finally I wish to thank all my friends and fellow students at the University of Copenhagen for making the process of writing a thesis extremely enjoyable.

Chapter 2

Magnetism

In this chapter I will give a very brief account on basic magnetism. The theory of magnetism will not be discussed in detail but some basic concepts that are important for the system studied here will be explained. Magnetic moments in solids and some important interactions between them will be introduced. I will explain how magnetic ordering comes about and what the most important magnetic structures are. I will go into a little bit more detail with the case of antiferromagnetism since this type of magnetic order is known to be present in our system. The chapter will be based on Stephen Blundells textbook (ref. [5]), which should be consulted for further information. Finally, the magnetic structure of bulk hematite, hematite nano-particles and ilmenite will be presented.

2.1 Magnetic moments

The magnetic moment of a current loop is defined as

$$\boldsymbol{\mu} = I\mathbf{a}, \tag{2.1}$$

where I is the current in the loop and $\mathbf{a}$ is a vector with a magnitude equal to the area of the loop and direction normal to the loop and with the sign determined by the 'right hand rule'. Since currents come from motion of charged particles there is an intimate connection between the magnetic moments and the angular momenta of the particles. In solids the particles giving rise to magnetic moments are usually electrons. For an electron with orbital angular momentum $\mathbf{L}$ the magnetic moment is

$$\boldsymbol{\mu}_{\mathrm{l}} = \gamma\mathbf{L}, \tag{2.2}$$

where the constant γ is the so-called gyromagnetic ratio. To get an idea of the size of atomic magnetic moments one can calculate the magnetic moment for an electron (mass m_e, charge $-e$, velocity v) in a circular orbit of radius

r around a hydrogen atom. The angular momentum in the ground state is $m_e vr = \hbar$ and the current around the atom is $I = \frac{-e}{\tau}$, where $\tau = \frac{2\pi r}{v}$. The magnetic moment of the electron is

$$\mu = \pi r^2 I = -\frac{e\hbar}{2m_e} \equiv -\mu_B, \tag{2.3}$$

where $\hbar$ is Planck's constant reduced and $\mu_B = 9.274 \cdot 10^{-24}\mathrm{Am}^2$ is the so-called Bohr magneton. The Bohr magneton is a useful quantity when discussing atomic magnetic moments and these are often given in units of μ_B. The size of γ is seen from (2.2) and (2.3) to be $\gamma = -e/2m_e$.The spin of the electron, which is an intrinsic angular momentum, also contributes to the magnetic moment of the atom. The magnetic moment due to the electron spin is

$$\boldsymbol{\mu}_\mathbf{s} = -g\mu_B \mathbf{S}, \tag{2.4}$$

where $g = 2.0023$ is the so-called g-factor. When looking at a macroscopic sample there are many atoms with magnetic moments and one defines the magnetization $\mathbf{M}$, which is the magnetic moment per unit volume.

2.2 Magnetic interactions

When discussing the interactions that are responsible for magnetic ordering one can often ignore the magnetic dipolar interaction since it is usually much weaker than the other interactions.

2.2.1 Zeeman interaction

The Zeeman interaction that tends to align the magnetic moments with an applied field is important. For a magnetic field B along the z-direction the Zeeman Hamiltonian looks like

$$\hat{H}_Z = -g\mu_B B \sum_j S_j^z, \tag{2.5}$$

where the summation is over the magnetic moments in the system.

2.2.2 Exchange interaction

An interaction that is important for a large variety of magnetic structures is the so-called exchange interaction. The interaction is quantum mechanical in nature and the name comes from the fact that electrons are identical fermions and therefore must have an antisymmetric wave function under particle exchange. The requirement of an antisymmetric two-particle wave function means that if the spatial part of the wave function is symmetric then the spin part of the wave function must be an antisymmetric singlet state

(S=0) whereas a antisymmetric spatial wave function implies a symmetric triplet (S=1) state for the spin part. One defines the exchange integral (or exchange constant) J as

$$J = \frac{1}{2}(E_S - E_T), \tag{2.6}$$

where E_S and E_T are the energies of the singlet and triplet state respectively. The idea can be generalized to a many body system with the Hamiltonian of the exchange interaction being modeled by the Heisenberg model:

$$\hat{H}_H = -\sum_{\langle i,j \rangle} J_{ij} \mathbf{S}_i \cdot \mathbf{S}_j. \tag{2.7}$$

Where the $\langle i, j \rangle$ means that the summation is over nearest neighbours and $\mathbf{S}_i$ and $\mathbf{S}_j$ are the spins on site i and j. J_{ij} is the exchange integral for electrons on site i and j. When J_{ij} is positive the exchange interaction favors parallel alignment of spins whereas a negative J_{ij} favors antiparallel spin alignment.

Direct and indirect exchange

The exchange interaction can either be direct or indirect. The interaction is called direct exchange when it is between neighbouring atoms, and indirect exchange (or superexchange) when the exchange is mediated by some nonmagnetic ion. Indirect exchange is common in transition metal oxides where the exchange interaction between the magnetic metal ions are mediated by the nonmagnetic oxygen ion. The d-orbitals of the metal electrons overlap with the p-orbitals of the oxygen making it possible for electrons with antiparallel spin to 'jump' between the metal ions and thus be delocalized giving a lower kinetic energy. If the spins on the metal ions are parallel the mixing of states is prohibited by the Pauli principle and this kind of superexchange thus favors antiparallel spin alignment.

Dzyaloshinsky-Moriya interaction

A further type of exchange interaction is the so-called Dzyaloshinsky-Moriya (DM) interaction that comes about because of the mixing of the ground state of one ion with an exited state of another. The form of the DM interaction is

$$\hat{H}_{DM} = \mathbf{D} \cdot \mathbf{S}_i \times \mathbf{S}_j, \tag{2.8}$$

where $\mathbf{D}$ is a vector that lies parallel or perpendicular to the line connecting the two spins. The DM interaction is present in some antiferromagnets (including $\alpha{-}\mathrm{Fe_2O_3}$) and its effect is to tilt (cant) the antiferromagneticly ordered spins slightly away from the antiferromagnetic sublattice directions. This called canting can produce a small net magnetization.

2.2.3 Magnetic anisotropy

To take account for the interaction of the magnetic moments of individual atoms with the field of the surroundings (the crystal field), one introduces a magnetic anisotropy term to the Hamiltonian. The magnetic anisotropy energy will reflect that it is favorable for the magnetization (spins) to be in certain directions in the crystal. These are called easy directions. The magnetic anisotropy energy could be of the form

$$E(\theta) = KV\sin^2(\theta). \tag{2.9}$$

Where V is the volume of the system (particle), K is the magnetic anisotropy constant and θ is the angle between the magnetization vector and a so called easy axis in the crystal. In general there could be more than one easy direction as we will see is the case for hematite.

2.3 Magnetic Ordering

When the energies in the interactions between the magnetic moments in a solid are larger than the energies in the thermal fluctuations it becomes favorable for the system to order magnetically. For a given system the thermal energies depends on the temperature whereas the magnetic energies typically depend on the strength of an applied field and the exchange constants J_{ij}, but could also depend on other parameters like for example the pressure. This means that by changing for example the temperature one can tune the magnetic state of the system. The Hamiltonian for the magnetic interactions could be the sum of a Heisenberg Hamiltonian (2.7) and a Zeeman Hamiltonian (2.5) and possibly a DM Hamiltonian (2.8). The sign of the exchange integral determines whether the magnetic moments (spins) like to be parallel or antiparallel and the Zeeman term tends to align the moments with the applied field.

2.3.1 Ferromagnetism

Imagine for simplicity a two dimensional square lattice of identical spins with $J_{ij} = J =$ constant for nearest neighbours, and let the applied field be zero. When $J > 0$ the magnetic ground state is ferromagnetic, meaning that all the spins are parallel. At temperatures above a certain critical temperature T_C called the Curie temperature, thermal fluctuations dominate and the system is in a paramagnetic state with zero net magnetization. At $T < T_C$ the spins start to align parallel and the net magnetization is now nonzero. At T = 0 K there are no thermal fluctuations and all the spins point in the same direction. Because all the moments point in the same direction the period in the magnetic ordering is the same as that of the structural unit cell. This means that in a neutron scattering experiment ferromagnetic scattering will show up in the same positions in reciprocal space as the structural Bragg-peaks.

2.3.2 Antiferromagnetism

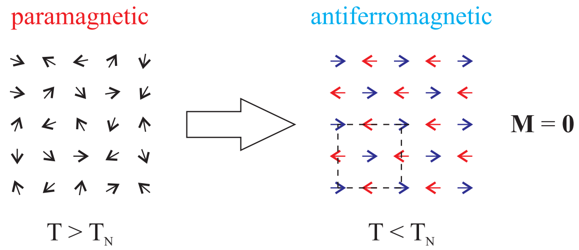

Figure 2.1: ***Antiferromagnetic order:*** *When the temperature drops below the Neél temperature the neighbouring spins align anti parallel. Spins in sublattice A (red) are pointing to the left and spins in sublattice B (blue) are pointing to the right and there is no resulting magnetization. The magnetic unit cell is twice the structural unit cell.*

Consider the same system as above, but with $J < 0$. The magnetic ground state is now antiferromagnetic (AFM), meaning that the spins on neighbouring atoms are antiparallel. For an antiferromagnet the critical temperature is called the Neél temperature (T_N) and the system is in a paramagnetic state for $T > T_N$ and an AFM state for $T < T_N$. The magnetizations on sub-lattices A and B (see fig. 2.1) are equal in magnitude but opposite in direction thus giving zero net magnetization:

$$\mathbf{M} = \mathbf{M}_A + \mathbf{M}_B = 0. \tag{2.10}$$

The differing spins on the two sub-lattices gives a magnetic unit cell that is larger than the structural unit cell. This means that antiferromagnetic peaks in a neutron scattering experiment can show up at points in reciprocal space where there are no structural peaks.

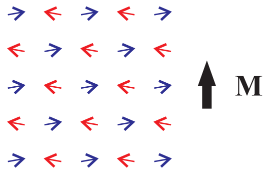

Figure 2.2: ***Canted antiferromagnetism:*** *In a canted antiferromagnet (CAFM) the spins rotate slightly away from the AFM sub-lattice direction giving a small net magnetization.*

In some materials the AFM order is perturbed by a DM interaction (2.8), making the spins in both sub-lattices rotate slightly away from the

AFM direction. This can give both sub-lattices a small moment in the same direction, leading to a small net magnetization (see fig. 2.2). This configuration is called canted antiferromagnetism (CAFM). The canting angle δ between the two sub-lattice magnetizations is typically of the order $\delta \approx 0.1°$.

Ferrimagnetism

Another important type of magnetic ordering is called ferrimagnetism. Ferrimagnetism is a mixture between ferromagnetism and antiferromagnetism. The ordering is similar to AFM with spins in different planes pointing antiparallel, but in a ferrimagnet the spins on the two antiferromagnetic sub-lattices are unequal (like in the right part of fig. 2.3) or only some layers align antiparallel (like in the left part of fig. 2.3). Either way the ferrimagnetic structure gives a nonzero magnetization and the Bragg peaks might show up on both the antiferromagnetic and ferromagnetic positions, depending on the period in the ordering of the moments.

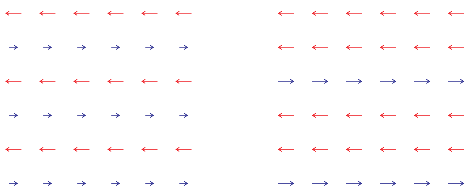

Figure 2.3: ***Two different types of ferrimagnetic order***

2.4 Magnetic structure of hematite

Hematite ($\alpha{-}Fe_2O_3$) has been extensively studied with a wide range of techniques. I will present some of the important data and all numerical values will be from the comprehensive work of A. Morrish in ref. [7]. The crystal structure of $\alpha{-}Fe_2O_3$ is the so called corundum structure ($R\bar{3}c$), which is a hexagonal structure (lattice parameters c = 13.772 Å and a = 5.038 Å), with alternating layers of Fe^{3+} ions bridged by O^{2-} ions (see fig. 2.4). The magnetic ground states of the ions in $\alpha{-}Fe_2O_3$ are determined by Hund's rules (see ref. [5]). Fe^{3+} has the outer shell structure $3d^5$, giving a magnetic ground state (in units of $\hbar$) of $S = \frac{5}{2}, L = 0, J = \frac{5}{2}$, where S, L and J are the spin, orbital and total angular momentum quantum numbers respectively. The outer shell structure of O^{2-} is $2p^6$ giving it a magnetic ground state of $S = L = J = 0$ and Fe^{3+} is thus the only magnetic ion. The effective moment of the ion in units of μ_B should be approximately

$$\mu_{\text{eff}} = g_J\sqrt{J(J+1)} = 2\sqrt{5/2(5/2+1)} \approx 5.92, \tag{2.11}$$

where the Landé g-factor is $g_J = 2$ in this case.

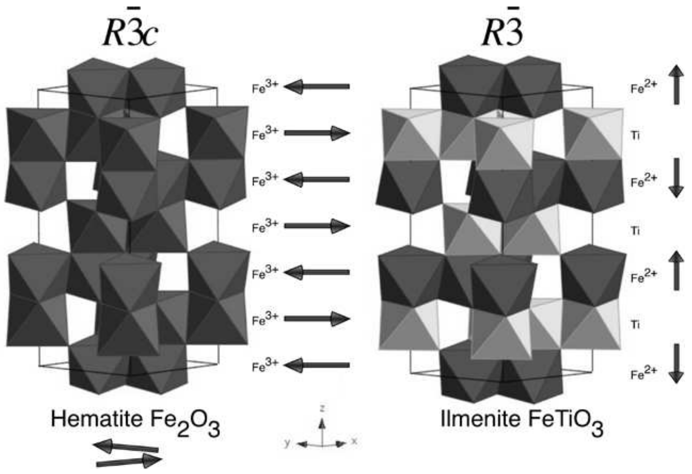

Figure 2.4: ***Crystal structure of** $\alpha-$**Fe**$_2$**O**$_3$ **and FeTiO**$_3$**. Left:*** *The magnetic structure of hematite for* $T_M < T < T_N$*. The Fe*$^{3+}$ *moments order antiferromagneticly in the a-b plane, but with a small in-plane canting giving a net magnetization.* ***Right:*** *The magnetic structure of ilmenite for* $T < T_N$*. The Fe*$^{2+}$ *moments order antiferromagneticly along the c-axis. Figure from [6]*

The Fe^{3+} ions in alternating layers interacts via superexchange interaction, bridged by the intermediate oxygen atoms. This makes $\alpha-$Fe$_2$O$_3$ order antiferromagneticly below a Néel temperature of $T_N \approx 955K$ (ref. [7]). The ordering of the Fe^{3+} ions in adjacent layers is thus AFM, while the in-plane order is FM. The AFM sublattice directions are in the basal plane (001), but the DM interaction gives the Fe^{3+} a small canting. The canting angle is reported in [7] to be 0.065° away from the AMF sublattice direction. The canting is in the basal plane and gives a magnetization of $2.10 \cdot 10^3 A/m$. A canting out of the plane has also been observed, but this is about a factor of 10^{-3} smaller than the already small in-plane canting [8].

F. J. Morin discovered in 1950 that there was an additional transition in hematite where the magnetization disappears [9]. At this so-called Morin transition the magnetic order changes to another AFM structure, where the sublattice spins are parallel and antiparallel to the crystallographic c - axis and with no canting. The Morin transition occurs at a temperature of $T_M \approx 263K$ for a macroscopic sample of pure $\alpha-$Fe$_2$O$_3$. The Morin temperature was observed to be lower for samples with impurities of for example titanium as well as in nano-sized hematite crystals. For hematite nano particles, T_M were observed to be significantly lowered for a particle size of less than 1μm [10] and for a particle size smaller than about 20 nm the Morin transition is found to be absent at temperatures down to that of liquid helium (4.2 K) [11]. The Morin transition is related to the magnetic anisotropy energy which can be expressed

$$\hat{H}_A = -\sum_i \left(\kappa_1 S_i^{x^2} + \kappa_B S_i^{z^2} \right), \tag{2.12}$$

where S^x is the spin along the c-axis and S^z is the spin along the easy axis in the basal plane. κ_1 and κ_B are the exchange constants (per atomic site). The basal plane anisotropy constant κ_B is positive and relatively small, meaning that the spins are relatively free to rotate in the basal plane (while maintaining the AFM - structure because of the Heisenberg interaction). The uniaxial anisotropy constant κ_1 is large compared to κ_B and determines whether the preferred spin direction is parallel or perpendicular to the c-axis. The Morin transition is triggered by a change of sign of κ_1, with $\kappa_1 < 0$ for $T > T_M$ and $\kappa_1 > 0$ for $T < T_M$ which happens at a lower temperature for nano particles. The temperature dependence of the anisotropy constants was demonstrated for hematite nano particles, by $q = 0$ spin-wave measurements in ref. [12].

2.5 Magnetic structure of ilmenite

The crystal structure of ilmenite ($FeTiO_3$) is similar to that of hematite ($R\overline{3}$, with lattice parameters c = 14.08 Å and a = 5.09 Å [13])), but with every other Fe layer replaced by a Ti layer. The ions in $FeTiO_3$ are Fe^{2+}, Ti^{4+} and O^{2-}. Fe^{2+} has outer shell structure $3d^6$, giving it spin 2 and angular momentum 2, while the the outer shell structure of Ti^{4+} is $3p^6$, giving it no net moment like the O^{2-}. The only magnetic ion in $FeTiO_3$ is thus the Fe^{2+} ion. If orbital quenching is assumed ($L = 0$) as is usually the case for transition metal ions the magnetic ground state of Fe^{2+} is not $S = 2$, $L = 2$, $J = 4$ as implied by Hund's rules, but $J = S = 2$ and $L = 0$. The effective moment is then approximately

$$\mu_{\text{eff}} = g_J \sqrt{J(J+1)} = 2\sqrt{2(2+1)} \approx 4.90. \tag{2.13}$$

The magnetic structure of ilmenite is AFM with moments on alternating Fe^{2+} layers pointing in opposite directions along the c-axis (see fig. 2.4). There may be a canting of about 1.6° away from the c-axis as presented in ref. [14]. The period of the AFM order in ilmenite is twice that of hematite because there is a Ti layer between the Fe^{2+} ions. This means that the superexchange has to interact via two layers of oxygen in stead of just one. Therefore it is not surprising that the AFM ordering of ilmenite occurs at a lower Néel temperature of $T_N \approx 55K$ [15].

Chapter 3

Hemo-ilmenite

The so called ‘hematite-ilmenite series’ is a naturally occurring rock mineral consisting of intergrowths of hematite and ilmenite. The chemical formula of the mineral can be expressed

$$(\mathrm{Fe_2O_3})_{1-x}(\mathrm{FeTiO_3})_x \quad , \quad 0 \leq x \leq 1, \tag{3.1}$$

where $x = 0$ represents pure hematite and $x = 1$ pure ilmenite. If the host is ilmenite ($x > 0.5$) the mineral is known as hemo-ilmenite, whereas rocks with hematite host ($x < 0.5$) are designated ilmeno-hematite. I will here go through the properties of the mineral that are most important for the understanding of the magnetic properties. Most of the considerations apply equally well to hemo-ilmenite and ilmeno-hematite samples, but since the sample studied here is of the hemo-ilmenite type, I will from now on discuss this material and only mention ilmeno-hematite, when the distinction is important. In the following I will explain some important features of the structure of hemo-ilmenite and then go on to explain the (unusual) magnetic properties and possible explanations for these. Finally some features about our particular sample will be mentioned.

The crystal structures of hematite and ilmenite is closely related and their lattice parameters similar (see sections 2.4 and 2.5). This makes it possible for the two phases to grow epitaxially together although there will be some strain in the system because the lattice parameters are not exactly the same.

There will be some $\mathrm{Fe^{3+}}$ in the ilmenite phase and $\mathrm{Ti^{4+}}$ and $\mathrm{Fe^{2+}}$ in the hematite phase. Mössbauer spectroscopy on hemo-ilmenite samples from Allard Lake, Canada resulted in an estimate of the $\mathrm{Fe^{2+}}/\mathrm{Fe^{3+}}$ ratio in hematite close to 0.2 and a $\mathrm{Fe^{3+}}/\mathrm{Fe^{2+}}$ ratio close to 0.06 [16]. Although this cation replacement is significant it does not provide an explanation for the observed magnetic properties.

Optical and electron microscopy have shown that the natural samples have a lamellar structure with inclusions of hematite lamellae in the ilmenite (and vice versa in ilmeno-hematite). Transmission electron microscopy (TEM) reveals that the lamellae grow in the (001) planes and have widths down to around unit cell size (1.4 nm) (see for example refs. [2] and [1]). The lamellae are shaped like flattened cigars. A TEM image of a hemo-ilmenite sample is displayed in figure 3.1. The TEM images show sharp boundaries between the lamellae and the surrounding host as well as strain 'shadows' that further indicates that the boundaries between the two phases are sharp. The lamellar structure is linked to the exsolution process, where magma was slowly cooled about a billion years ago, producing several generations of lamellae in different sizes as the temperature decreased.

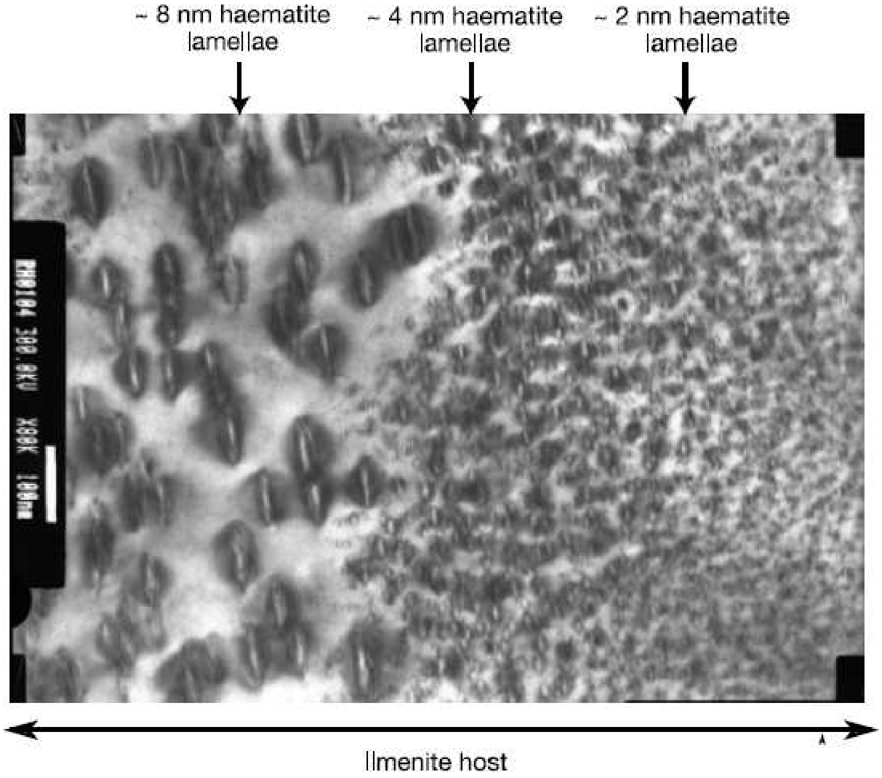

Figure 3.1: ***Transmission electron micrograph of hemo-ilmenite sample.*** *The sample is from an ore deposit in South Rogaland, Norway (see fig. 1.1). Three generations of hematite lamellae are visible, with thickness of about* $2\,nm$*,* $4\,nm$ *and* $8\,nm$*. Lamellae exist with thickness of up to millimeters. The white scale bar is* $100\,nm$*. Figure from [4].*

3.1 Magnetic properties of hemo-ilmenite

The ‘hematite-ilmenite’ system is extensively studied with methods such as electron microscopy, x-ray fluorescence spectroscopy (XRF), electron backscattering, Mössbauer spectroscopy as well as magnetic bulk measurements like susceptibility and magnetization measurements. The NRM of some good quality samples is reported in ref. [17] to be 1.4-4.2 $\cdot 10^{-3}$ Am^2/kg. [1] This magnetization was induced by the magnetic field of the Earth ($\approx 50\mu$T) during the exsolution process, and is much lower than the saturation magnetization.

The saturation magnetization is in general said to be too large to be explained only by the magnetic moment of hematite (2.1 kA/m or 0.40 Am^2/kg [7]). For example the saturation magnetization for our sample was measured to be 0.19 Am^2/kg [18]. Hematite constitutes 16.7% of the sample mass and can therefore only explain about one third of the magnetization. Ilmenite is paramagnetic at room temperature and the fact that a magnetization of this magnitude comes about is surprising. Measured hysteresis loops show that the saturation magnetization is reached at applied fields of 0.5 - 1 T (see fig. 3.2).

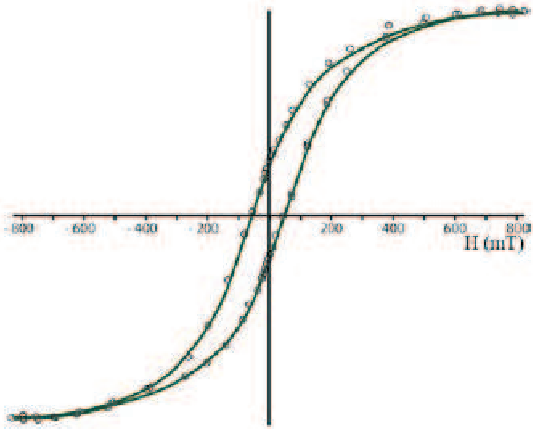

Figure 3.2: ***Hysteresis loop of hemo-ilmenite sample.*** *The hysteresis measurement shows that the sample magnetization is saturated at a field of about 0.8 T. Figure from [1].*

---

[1] This definition of the magnetization as the magnetic moment per unit weight is used because the sample masses are well known.

The coercivity of the samples is high compared to other rock minerals and many samples do not demagnetize in alternating fields of up to 0.1 T. The samples are about a billion years old and must thus have a high temporal stability. The coercivity in hemo-ilmenite samples is generally a little lower than in samples with hematite host. The samples demagnetize at temperatures around 530-650 $^{\circ}C$ [4] which is comparable to the Néel temperature of hematite ($682^{\circ}C$).

As the samples are natural they contain impurities that might be important for the magnetic properties. In particular the existence of magnetite (Fe_3O_4) inclusions could be important. Magnetite has a magnetic moment of around 480 kA/m [19] and is known to be responsible for magnetic anomalies. For some samples magnetite inclusions are explicitly ruled out as the explanation of the NRM, because such structures are not seen in the TEM images [6], while for other samples magnetite is believed to be present but only in small amounts [17]. It should also be noted that there is a significant amount of Ti in the hematite phase and the Morin transition may therefore be suppressed even for the largest lamellae. We have to study natural samples since it, to our knowledge, has not yet been possible to grow hemo-ilmenite samples with exsolution lamellae synthetically.

The contribution to the magnetization from canting of the Fe^{3+} moments is not nearly large enough to explain the high value of the NRM, unless some unusual mechanisms are present. The strain in the system can change the symmetry in the crystal slightly, and this could have a significant effect on the DM-interaction and thus on the canting. The strain will be most pronounced in the small lamellae because they have a larger surface relative to their volume. An increased canting, especially in the small lamellae might therefore be present in the system. To explain the saturation magnetization of the sample being three times that explainable by a hematite canting of $\theta = 0.065^{\circ}$ the canting would have to be three times as much. (The magnetization from the canting is proportional to $\sin(\theta)$ and the angle is small.)

Another possible explanation is that the magnetic moment comes from uncompensated spin in contact layers between the lamellae. This hypothesis is known as ‘lamellar magnetism’ and I will elaborate on that in the next section. In summary the mechanism behind the NRM is believed to be one of, or a combination of

- Canting of hematite moments
- Magnetic impurities
- Lamellar magnetism

In this list the magnetic impurities seems unlikely as the explanation, since the magnetic properties remain in very pure samples and seem to be linked to the coercivity and Curie temperature of hematite. Hematite spin canting gives a magnetization perpendicular to the AFM sublattice directions, whereas lamellar magnetism (see below) would give a magnetization parallel to the AFM sub-lattices.

3.2 Lamellar magnetism

The basis of the lamellar magnetism hypothesis is that the magnetism is intimately linked to the lamellar structure of the intergrowths. To study the dynamics of the exsolution process, Monte Carlo simulations of the cation ordering were performed and the results presented in several publications (see for example [4] and [6]).

The starting point of the simulation is a number of layers of randomly distributed cations and spins with a fixed total chemical composition. In each step of the MC procedure 2 random spins or ions are substituted, and the configuration is changed to the new one with a (Boltzmann) probability that depends on the free energy of the configuration. This procedure is repeated some 10^6 times until the system is in a equilibrium configuration.

Chemical interactions as well as magnetic exchange interaction between nearest and next nearest neighbours were simulated at a (virtual) temperature of 500 K and with periodic boundary conditions. The result of simulating such a model is shown in figure 3.3. The resulting structure is essentially pure lamellae of CAF hematite and PM ilmenite with a single contact layer between. The contact layer contains equal amounts of Fe^{2+} and Fe^{3+} with spins coupled antiferromagnetically to the hematite. One explanation of the emergence of contact layers, which is stated in [6], is that the contact layers will reduce charge imbalance on the oxygen ions and it may also reduce the strain in the surfaces between lamellae and host.

When the host is ilmenite the lamellae of hematite will always have an odd number of layers because the lamellae always will start and end on a former Ti layer of the ilmenite. The contact layers are not chemically part of either ilmenite or hematite, but couples antiferromagneticly to the hematite. The resulting structure is thus ferrimagnetic with a net moment in the basal plane from each lamella. The high stability and coercivity of the material might be understood on the basis of the coupling of the contact layers to the hematite.

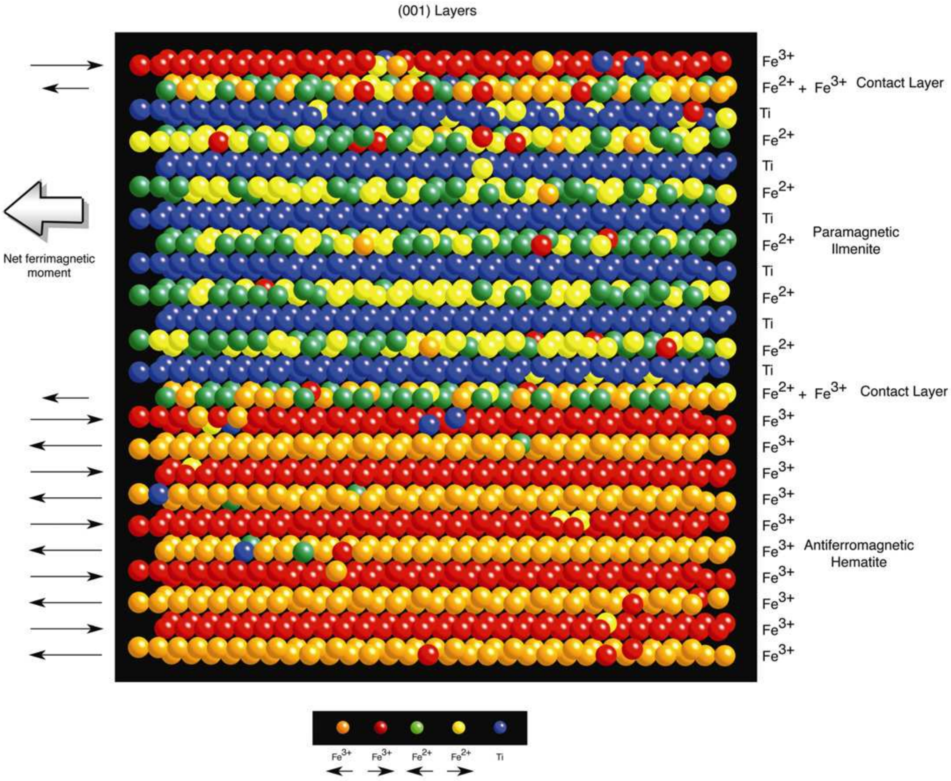

Figure 3.3: ***Monte Carlo simulation of the cation ordering.*** *In the bottom half is an essentially pure hematite lamellae and in the upper part an essentially pure ilmenite lamella. Between the lamellae 2 contact layers with uncompensated spins gives a ferrimagnetic substructure. Figure from [1].*

A net magnetization will only arise if the moments of the lamellae are aligned. The magnetic field (of Earth) at the time of exsolution may favor the formation of lamellae parallel to the field and this would be the origin of the NRM. The magnetization will be largest when the geomagnetic field is in the basal plane of the crystal and this will result in the highest number of aligned lamellae and thus the highest magnetization. Further the resulting magnetization will depend on the amount of surface layers in the system, which depends on how fine scale the lamella are, and thereby the exsolution process.

The situation is similar when the host is hematite, since the crucial thing is the contact layers between the phases. The main difference is that in an hematite host the direction of the lamellar moment is dictated by the position of the lamella in the host (whether it is started adjacent to a hematite layer with spin left or right). This means that the coercivity of the hematite host will in general be higher because the entire sample will have to be demagnetized in order to demagnetize the lamellar moments.

It is estimated that in extremely favorable conditions lamellar magnetism could generate magnetizations up to 55 kA/m [4], which is 28 times the saturation magnetization of pure hematite. The lamellar magnetism hypothesis is based on the MC simulations but still lack direct experimental evidence.

3.3 The sample

This work is based on experiments on a single sample of hemo-ilmenite from South Rogaland, Norway. The sample, named Pramsknuten 5-1 T, was collected in the 'Pramsknuten' dike and is an ilmenite host (84 % $FeTiO_3$) with exsolution lamellae of hematie (16 % Fe_2O_3). The sample weight is 1.9770 g and its dimensions are roughly $12\,\text{mm} \times 8\,\text{mm} \times 8\,\text{mm}$. A photo of the sample is presented in figure 3.4.

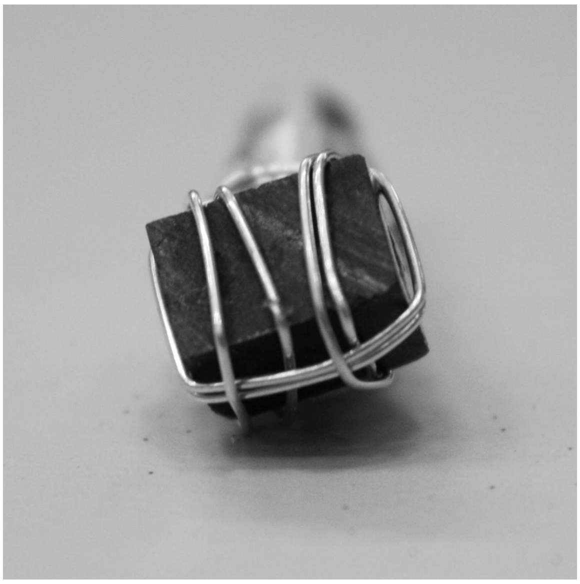

Figure 3.4: ***Photo of the sample.*** *In the photo the sample is tied to the sample holder for the SANS experiment with aluminium wire. In the TASP experiment the sample was glued to the holder. The crystallographic c-axis is at an angle of roughly 10° with respect to one of the long edges of the sample.*

The sample has been studied with various techniques and some of the results are presented in [17]. The composition of the sample is known from X-ray fluorescence spectroscopy (XRF) and electron microprobe (EMP) analysis and the list of impurities can be found in the reference. Most importantly no evidence for magnetite inclusions were found. Some important measured parameters for the sample are given in table 3.1.

m [g]	NRM [10^{-3}Am^2/kg]	M_s [Am^2/kg]
1.9770	2.613	0.19

Table 3.1: ***Some important sample parameters.*** *The values of the sample mass and NRM is from [17] and the value of the saturation magnetization* M_s *is from personal communication with Richard Harrison.*

Chapter 4

Neutron scattering

In this section I will go through the theory that is necessary to understand how a neutron scattering experiment works and how the results of the presented experiments should be understood. First some basic properties of neutron scattering is introduced and then I will proceed to describe scattering from a crystal, including magnetic scattering. I will not discuss inelastic scattering, since the experiments relevant to my thesis were elastic. The chapter will be strongly inspired by refs. [20] and [21].

4.1 Basics of neutron scattering

Before discussing scattering of neutrons from a crystal I will go through some basic concepts. The basic properties of the neutron, which makes it an important probe for investigating solid state phenomena will be discussed. I will also shortly describe how neutrons for scattering experiments are produced and delivered to the sample position with the desired properties. This will be followed by a description of how a (neutron) scattering experiment works and an introduction to important concepts like the scattering cross-section and the scattering vector.

4.1.1 Properties of the neutron

The neutron is, as the reader will know, a particle usually found in atomic nuclei. This has been known since James Chadwick's discovery of the neutron in 1932 [22]. Free neutrons come about as products of nuclear processes like fission and have a decay time of around 15 minutes.

The neutron consists of 3 quarks (udd), giving it 0 net charge and a spin of $\frac{1}{2}$. The mass of the neutron is slightly larger than that of the proton. Some basic properties of the neutron are listed in table 4.1.

Mass, m_N	$1.675 \cdot 10^{-27}$ kg
Charge	0
Spin	$\frac{1}{2}$
Magnetic dipole moment	$-1.913\,\mu_N$

Table 4.1: ***Basic properties of the neutron.*** *The nuclear magneton is* $\mu_N = \frac{e\hbar}{2m_P} = 5.051 \cdot 10^{-27} J/T$

Since the neutron is electrically neutral it does not interact with the charge of the electrons in atoms. Other probes, like x-rays, are sensible to the electron clouds around atoms, and therefore have a scattering amplitude that is roughly proportional to the atomic number of the scattering atom. The neutron is a nuclear particle and interacts with the atomic nuclei via the strong nuclear force. The scattering amplitude for neutrons vary across the periodic table and even between different isotopes of the same element. This makes the neutron a valuable probe for light elements that are difficult or even impossible to see with x-rays. The possibility of 'highlighting' a specimen with a selected isotope further gives the possibility to enhance certain features in the system that one wants to measure.

Another important difference between x-rays and neutrons is the energy of the probe. Where x-rays have energies of about 0.1-100 keV, the energies of the neutrons used in experiments are roughly in the range 0.1 - 500 meV, making it possible to measure small energy changes. With inelastic neutron scattering it is therefore possible to study important phenomena like lattice vibrations in crystals.

Neutrons are as much waves as they are particles and one refers to their wavelength as frequently as to their energy. The De Broglie wavelength λ of a neutron with mass m_n, velocity v and energy E is:

$$\lambda = \frac{h}{m_n v} = h\sqrt{\frac{1}{2m_n E}}, \tag{4.1}$$

where h is Planck's constant. It is seen that the energy range of 0.1 - 500 meV corresponds to a wavelength range of about 30 - 0.4 Å (corresponding to inter-atomic distances in solids.)

Another very important point is that the neutron has a magnetic moment. The 3 quarks that make up the neutron are responsible for making it a spin $\frac{1}{2}$ particle and thus eligible to interact with the dipolar field from unpaired electrons in magnetic atoms and the magnetic moments of nuclei. The neutron is therefore ideal to study magnetic structures. With the energies of the available neutrons in the meV range, the neutron is also well suited for measurements of magnetic excitations. Further the possibility of working with a beam of polarized neutrons makes it possible to distinguish between magnetic and nuclear contributions to the scattering, and to obtain the magnetic structure, including spin directions in a crystal.

Because neutrons interact rather weakly with matter, they can easily penetrate significant lengths of material. Neutron scattering experiments can therefore be done on samples inside cryostats, furnaces, magnets and other kinds of 'bulky' sample environments. Another benefit of the weakness of the neutrons interaction is that higher order effects like multiple scattering usually can be ignored. Further the weakness of the interaction means that the neutrons penetrate the sample deeply, and thus probe the bulk, rather than just the surface.

4.1.2 Production, moderation and delivery of neutrons for experiments

There are two ways of producing neutrons for scattering experiments. The classical method of producing neutrons is in the fission process of a nuclear reactor. Here heavy elements like ^{235}U are split into smaller nuclei, while expelling excess neutrons. This method gives a continuous flow of neutrons as long as the reactor is kept running.

Another way of producing a high flux of neutrons is the spallation technique, where protons are accelerated to an energy of 1-2GeV and into a target of liquid or solid heavy metal, like mercury or lead. When the heavy nuclei absorbs the high energy particles, they become very unstable and evaporates a large number of neutrons. Spallation sources are often pulsed, since it is easy to make a pulsed bunch of high energy protons and one can then use time of flight (TOF) techniques[1].

All the neutron scattering experiments presented here were performed using the SINQ spallation source in the Paul Scherrer Institute, Switzerland. This is a continuous spallation source with a lead target.

When the neutrons leave the spallation target (or the reactor) they have energies in the MeV range and need to be slowed down to lower energies. This is done by letting the neutrons pass through a vessel filled with for example heavy water at a temperature of 300 K (thermal neutrons) or liquid

---

[1] In a TOF neutron spectrometer one utilizes the different flight times of neutrons in a polychromatic pulse to determine the energies of the neutrons.

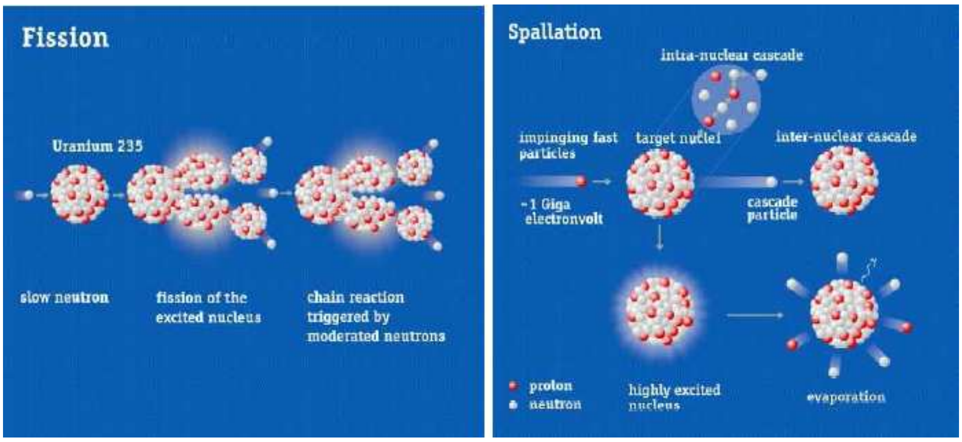

Figure 4.1: ***Production of neutrons:*** *Left: Neutrons are produced as byproducts in a fission process. Right: Neutrons are produced in a spallation process where high energy particles are accelerated into a target of heavy metal, which evaporates neutrons. Figure from [20]*

deuterium at a temperature of 25 K (cold neutrons). When the neutrons pass through the liquid they undergo multiple collisions, reducing their energy, until they are in thermal equilibrium with the moderator liquid.
When the neutrons have been moderated they should ideally have a Maxwellian wavelength distribution:

$$I(\lambda) = I_0 \lambda^{-5} \exp\left(-\frac{h^2}{2\lambda^2 m_n k_B T}\right), \tag{4.2}$$

where I_0 is a constant proportional to the power of the source, and k_B is Boltzmann's constant. This wavelength distribution is shown in figure 4.2 for a could source ($T = 25K$) and a thermal source ($T = 300K$). In reality the neutrons does not reach thermal equilibrium when they pass through the moderator and the description of the wavelength distribution by a single Maxwellian is not adequate. For the cold source at PSI, Switzerland the distribution is well described with the sum of 3 Maxwellians with temperatures $T_1 = 10K$, $T_2 = 59K$ and $T_3 = 275K$.

After the moderator the neutrons enter a 'guide', which is a tube that guides the neutrons from the moderator to the experiment, that is placed 10-100 m away from the source to reduce background. The guide usually has a rectangular cross-section of around 10 × 2 to 15 × 5 cm^2. The inside of the guide is coated with mirrors that have total reflection for neutrons with incident angles less than a small critical angle. The critical angle of total reflection depends on the wavelength of the neutrons and a typical coating material is Ni. Ni has a critical angle of $\theta_{c,Ni} = 0.0999°\text{Å}^{-1}\lambda$. The

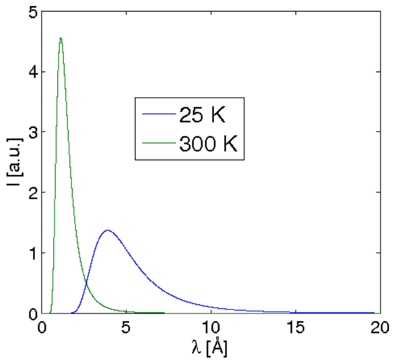

Figure 4.2: ***Wavelength distribution of moderated neutrons.*** *Ideally the distribution should follow a Maxwellian as in the figure, but in reality the situation is a bit more complicated because the limited size of the moderator does not allow the neutrons to reach thermal equilibrium.*

guide mirrors are often made of multilayer structures that enhances the reflectivity above the critical angle. The quality of a multilayer coating is usually specified by the so called m - value which specifies how much better then a pure Ni mirror the coating is. The formula for the critical angle becomes:

$$\theta_c = \theta_{c,Ni}\mathrm{m} = 0.0999^\circ \mathrm{\AA}^{-1}\lambda\mathrm{m}. \tag{4.3}$$

Neutrons with high divergence are absorbed by the guide walls since their incident angle is significantly larger then the critical angle. For a m = 2 guide and 4 Å neutrons as was used in the TASP experiment the critical angle and hence the divergence of the beam at the guide exit is $\theta_c = 0.8^\circ$.

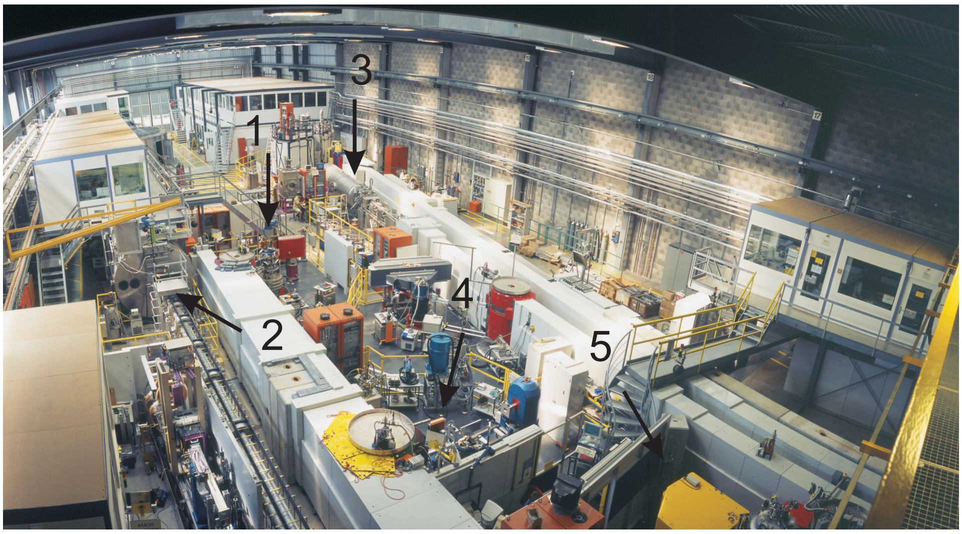

Figure 4.3: ***Experimental hall of SINQ, PSI, Switzerland.*** *The gray guides stretch through the experimental hall and deliver neutrons to the different instruments. The main part of my experiments was done on TASP and SANS-I. TASP can be seen by the end of the leftmost guide with its red detector sticking out (1). The collimation section of SANS-I is seen in the left part of the photograph ending in the detector tank under the hutch in the left side of the hall (2). Visible is also SANS-II (3) and Morpheus (4). Photo from the PSI homepage [23].*

4.1.3 Scattering of neutrons - The cross-section

In a neutron scattering experiment the quantity we measure is the number of neutrons scattered into a detector. We need some way to connect this number to the interaction of the neutrons with the sample. The starting point is the scattering cross-section σ, which is defined below

$$\sigma = \frac{1}{\Psi} \cdot \text{number of neutrons scattered per second.} \tag{4.4}$$

Where Ψ is the flux of neutrons on the sample (neutrons per area per second). Further one defines the differential scattering cross-section for scattering into a solid angle $d\Omega$ which is:

$$\frac{d\sigma}{d\Omega} = \frac{1}{\Psi} \frac{\text{number of neutrons scattered per second into}\, d\Omega}{d\Omega}. \tag{4.5}$$

As the detector only subtends a finite solid angle ($d\Omega$), this is the quantity that is actually measured in diffraction experiments. Obviously the total cross-section is the sum (integral) of the differential cross-section over all solid angles.

Now let us look at what happens with the neutron and the sample in the scattering process and get an expression for the differential scattering cross-section. The neutron can be described as a plane wave with wave vector $\mathbf{k}$ and position vector $\mathbf{r}$:

$$\psi(\mathbf{r}) = \frac{1}{\sqrt{Y}} \exp(i\mathbf{k} \cdot \mathbf{r}), \tag{4.6}$$

where Y is a normalization constant. When neutrons are scattered by a scattering system (sample) energy and momentum can be transfered between the neutron and the system changing the state of both. A fundamental result from quantum mechanics called Fermi's golden rule (see e.g. [24]) relates the number of transitions from one state to another to the matrix element of the initial and final states with the interaction potential. This together with the incident flux gives the differential scattering cross-section for scattering neutrons from initial state $|\psi_i\rangle$ to final state $|\psi_f\rangle$:

$$\frac{d\sigma}{d\Omega} = Y^2 \frac{k_f}{k_i} \left(\frac{m_n}{2\pi\hbar^2} \right)^2 \left| \left\langle \psi_i \left| \hat{V} \right| \psi_f \right\rangle \right|^2, \tag{4.7}$$

where k_i and k_f are the incident and final wave numbers, m_n is the neutron mass, and $\hat{V}$ is the interaction potential (operator). The normalization constant Y disappears because it also appears in the states ψ_i and ψ_f and when the scattering is elastic the expression is further simplified because the initial and final wave numbers are the same. In the following I will assume the scattering to be elastic.

4.1.4 The scattering length

For now I will neglect magnetic contributions to the scattering and consider the scattering to be purely nuclear. I will come back to magnetic scattering in section 4.2.3. For nuclear scattering the scattering potential (from the j'th nucleus at position $\mathbf{r}_j$) is the Fermi pseudo potential

$$\hat{V}_j(\mathbf{r}) = \frac{2\pi\hbar^2}{m_n} b_j \delta(\mathbf{r} - \mathbf{r}_j), \tag{4.8}$$

where b_j is a constant for the j'th nucleus, called the scattering length.
If we consider elastic scattering from a single nucleus fixed at position $\mathbf{r}_j$ and with scattering length b_j the matrix element from (4.7) can be calculated as

$$\begin{aligned} \left\langle \psi_f \left| \hat{V}_j(\mathbf{r}) \right| \psi_i \right\rangle &= \frac{2\pi\hbar^2}{m_n} b_j \int \exp(-i\mathbf{k}_f \cdot \mathbf{r}) \delta(\mathbf{r} - \mathbf{r}_j) \exp(i\mathbf{k}_i \cdot \mathbf{r}) d^3\mathbf{r} && (4.9) \\ &= \frac{2\pi\hbar^2}{m_n} b_j \int \exp(i\mathbf{q} \cdot \mathbf{r}) \delta(\mathbf{r} - \mathbf{r}_j) d^3\mathbf{r} && (4.10) \\ &= \frac{2\pi\hbar^2}{m_n} b_j \exp(i\mathbf{q} \cdot \mathbf{r}_j), && (4.11) \end{aligned}$$

where I have introduced the vector

$$\mathbf{q} = \mathbf{k}_i - \mathbf{k}_f, \tag{4.12}$$

called the scattering vector or the momentum transfer. The differential scattering cross-section is now seen to be simply

$$\frac{d\sigma}{d\Omega} = b_j^2, \tag{4.13}$$

which is independent of q. The scattering length is a fundamental nuclear quantity that varies between different nuclei and even between different isotopes of the same element. This is one of the reasons that neutron scattering sometimes can be used to investigate problems that can not be solved with x-ray scattering.

4.1.5 The scattering vector

The scattering vector $\mathbf{q} = \mathbf{k}_i$ -$\mathbf{k}_f$ (see fig. 4.4) is extremely important and will be used frequently throughout the rest of the thesis. It can be seen from the figure that for elastic scattering, where k_i=k_f, there is a simple relation between the scattering vector and the scattering angle.

$$q = 2k\sin(\theta), \tag{4.14}$$

where θ is half the scattering angle. In experiments the measured quantity is the scattering angle but in the data analysis one almost always works in reciprocal space (see section 4.2) and the identity (4.14) is useful when moving back and forth between real and reciprocal space.

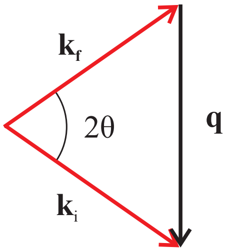

Figure 4.4: ***Scattering vector.*** *This scattering triangle shows the definition of the scattering vector* ***q****. The incoming and outgoing wave vectors are equal in magnitude and the depicted scattering event is thus elastic.*

4.1.6 Coherent and incoherent scattering

When discussing scattering from a larger ensemble of nuclei, like a crystal, it is important to distinguish between coherent and incoherent scattering. In a natural ensemble of nuclei there will be random variations in the scattering length from site to site because they are occupied by different isotopes or because the nuclei have nuclear spin giving a scattering length that varies with the spin and polarization direction of the neutrons. These random variations in scattering length gives rise to incoherent scattering. The incoherent scattering is isotropic and thus gives a uniform background on top of the coherent signal, which one usually wants to measure. The coherent scattering comes from the average value of the scattering length on each site and can give rise to interference effects giving distinct anisotropic scattering patterns. When I talk about scattering lengths and cross-sections I will always be referring to coherent scattering unless it is explicitly stated that the value is for incoherent scattering.

4.2 Scattering from crystals

In this section I will discuss the scattering of neutrons from a crystalline solid. I will start with ignoring the spin of the neutron (and the nuclei for that matter) and consider only coherent nuclear scattering. Most of the formalism developed here can be applied just as well to magnetic scattering, only with a different interaction potential and sometimes a different magnetic unit cell than the unit cell of the crystal structure.

A crystal is an array of atoms arranged periodically in a lattice that is a repetition of some, usually quite simple, unit cell. The basic crystal structures are covered in introductory courses on solid state physics and can be found in textbooks like [25].

When dealing with scattering experiments, Fourier analysis is an essential tool to understand the scattering pattern from the sample and it is very useful to work in the so called reciprocal space. The reciprocal lattice of a crystal lattice with primitive lattice vectors **a**, **b** and **c** is defined by the primitive vectors of the reciprocal lattice:

$$\mathbf{a}^* = 2\pi\frac{\mathbf{b}\times\mathbf{c}}{\mathbf{a}\cdot(\mathbf{b}\times\mathbf{c})}\,, \qquad \mathbf{b}^* = 2\pi\frac{\mathbf{c}\times\mathbf{a}}{\mathbf{a}\cdot(\mathbf{b}\times\mathbf{c})}\,, \qquad \mathbf{c}^* = 2\pi\frac{\mathbf{a}\times\mathbf{b}}{\mathbf{a}\cdot(\mathbf{b}\times\mathbf{c})}. \tag{4.15}$$

A reciprocal lattice vector is any vector $\boldsymbol{\tau}_{hkl} = h\mathbf{a}^* + k\mathbf{b}^* + l\mathbf{c}^*$, h, k and l being integers. The indices h, k and l are the so called Miller indices and are used to describe crystal planes as well as reciprocal lattice vectors. When one refers to reciprocal lattice units (r.l.u.) it simply means units of h, k

and l. The way crystal planes are indexed with Miller indices is described in textbooks like [25] and will not be explained here. The reciprocal lattice vector $\boldsymbol{\tau}_{hkl}$ is perpendicular to the plane with indices (hkl) and the spacing between the (hkl) planes is

$$d_{hkl} = \frac{2\pi}{|\boldsymbol{\tau}_{hkl}|}\,. \tag{4.16}$$

4.2.1 Bragg's law

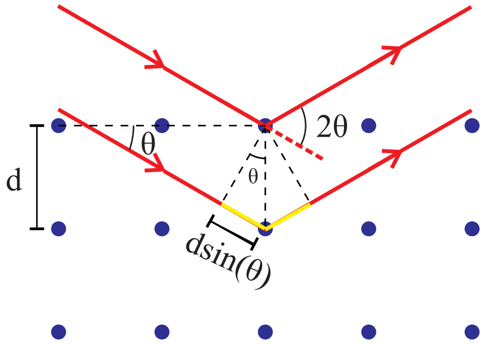

Figure 4.5: ***Bragg's law:*** *A neutron scatters off nuclei in different crystal layers. The condition for the wave scattered from the top layer to be in phase with the wave scattered from the second layer is that their difference in path length is an integer number of wavelengths. The difference in path length (yellow) is* $2d\sin(\theta)$*.*

Because a crystal is periodic it has the possibility to scatter radiation in phase and thus giving a strong scattering signal making it possible to obtain information about the crystal structure and the atoms in it. The condition for radiation scattered from different crystal layers to be in phase is that the difference in the path length traveled is an integer number of wavelengths (see fig. 4.5). This condition for constructive interference is known as Bragg's law (or the diffraction condition) and applies equally well to neutrons and x-rays. Bragg's law can be expressed as

$$n\lambda = 2d\sin(\theta). \tag{4.17}$$

Here $n\lambda$ is an integer number of wavelengths, d is the distance (d-spacing) between the scattering lattice planes and θ is the angle between the lattice plane and the incoming beam or in other words half the scattering angle. Elastic scattering from a crystal (diffraction) is often referred to as Bragg scattering and the peaks seen in the scans are called Bragg peaks. If we exchange $\frac{2\pi}{\mathrm{k}}$ for λ in (4.17) and use the identity (4.14) we obtain:

$$n\frac{2\pi}{k} = d\frac{q}{k}, \tag{4.18}$$

$$n\frac{2\pi}{d} = q. \tag{4.19}$$

Using (4.16) it is obvious that Braggs law now can be stated

$$n\boldsymbol{\tau} = \mathbf{q}, \tag{4.20}$$

where I have switched back to vector notation since $\mathbf{q}$, like $\boldsymbol{\tau}_{hkl}$ is perpendicular to the scattering crystal plane. This form of Braggs law states that the scattering from a set of crystal planes is in phase only when the scattering vector is equal to a reciprocal lattice vector $\boldsymbol{\tau}$. For this reason one often refers to the Miller indices of a scattering vector and I will do this when talking about different reflections in a crystal.

The situation with one atom in the unit cell (Bravais lattice), depicted in figure 4.5 is more simple then most real cases. Often there will be different atoms at different positions in the unit cell making a more complex interference pattern. For example destructive interference can sometimes extinguish some of the reflections that would otherwise be allowed by Bragg's law.

4.2.2 Elastic nuclear scattering cross-section

Now I will proceed to present the scattering cross-section for a non Bravais lattice with an arbitrary number of atoms in the unit cell. The elastic nuclear scattering cross-section for a collection of nuclei at positions $\mathbf{r}_j$ with scattering lengths b_j can be written (see equation 7.3 in [20])

$$\left.\frac{d\sigma}{d\Omega}\right|_{nucl.} = \exp(-2W)\left|\sum_j b_j \exp(i\mathbf{q}\cdot\mathbf{r}_j)\right|^2, \tag{4.21}$$

where $\exp(-2W(T))$ is the so called Debye-Waller factor that corrects for the fact that the nuclei are not fixed in position because of thermal vibrations. If the i'th atom (nuclei) in the j'th unit cell is at a position $\mathbf{r}_{i,j} = \mathbf{r}_j + \boldsymbol{\Delta}_i$, where $\mathbf{r}_j$ is the position of the j'th unit cell and $\boldsymbol{\Delta}_i$ is the position of the i'th atom in the unit cell, the elastic nuclear cross-section reads

$$\left.\frac{d\sigma}{d\Omega}\right|_{nucl.el.} = \exp(-2W)\left|\sum_{i,j} b_i \exp(i\mathbf{q}\cdot(\mathbf{r}_j + \boldsymbol{\Delta}_i))\right|^2 \tag{4.22}$$

$$= \exp(-2W)\,|F_N(\mathbf{q})|^2\left|\sum_j \exp(i\mathbf{q}\cdot\mathbf{r}_j)\right|^2, \tag{4.23}$$

where the nuclear structure factor $F_N(\mathbf{q})$ has been defined as

$$F_N(\mathbf{q}) = \sum_i b_i \exp(i\mathbf{q}\cdot\mathbf{\Delta}_i). \tag{4.24}$$

In an experiment one often wishes to determine the nuclear structure factor to get information about the positions of the atoms in the unit cell.

It can be shown that the lattice sum only contributes to the cross-section when the scattering vector is equal to a reciprocal vector. Intuitively it is easy to see that when this is the case the sum will contribute with a factor of N (N being the number of unit cells) and all the contributions from other scattering vectors will cancel because they are smeared over the entire unit sphere. The mathematical statement of this requirement, which is equivalent to the diffraction condition, comes from the calculation of the sum. With N unit cells of volume V_0 the unit cell sum looks like

$$\left|\sum_j \exp(i\mathbf{q}\cdot\mathbf{r}_j)\right|^2 = \mathrm{N}^2\sum_{\boldsymbol{\tau}}\delta_{\mathbf{q},\boldsymbol{\tau}} = \mathrm{N}\frac{(2\pi)^3}{V_0}\sum_{\boldsymbol{\tau}}\delta(\mathbf{q}-\boldsymbol{\tau}), \tag{4.25}$$

with the Dirac delta function representing the diffraction condition (Braggs law). The final version of the elastic nuclear cross-section is

$$\left.\frac{d\sigma}{d\Omega}\right|_{nucl.el.} = N\frac{(2\pi)^3}{V_0}\exp(-2W)\,|F_N(\mathbf{q})|^2\sum_{\boldsymbol{\tau}}\delta(\mathbf{q}-\boldsymbol{\tau}) \tag{4.26}$$

4.2.3 Magnetic neutron scattering

The magnetic moment of the neutron enables it to interact with the magnetic moments in solids and thus get information about the magnetic structure of a sample. The starting point is (4.7), but now we also have to take the initial and final spin of the neutron into account and we have to replace the Fermi pseudopotential with a magnetic interaction potential (to be defined in 5.11). In my experiments I have utilized polarized neutrons, which can be a great advantage when dealing with magnetic scattering. Therefore I will postpone the more thorough discussion of the cross-sections for magnetic scattering to section 5. Here I will briefly mention the result for elastic magnetic scattering and introduce a few new variables.

The elastic cross-section for magnetic scattering with unpolarized neutrons is (7.85 in [21])

$$\left(\frac{d\sigma}{d\Omega}\right)_{el} = e^{-2\mathrm{W}}\left(\frac{\gamma r_0}{2\mu_B}\right)^2 |\hat{\mathbf{q}}\times\{\langle\mathbf{M}(\mathbf{q})\rangle\times\hat{\mathbf{q}}\}|^2\,. \tag{4.27}$$

Here the constants $\gamma = 1.913$ and $r_0 = 2.818 \cdot 10^{-15}$ m are the gyromagnetic ratio and the classical electron radius and $\hat{\mathbf{q}}$ is a unit vector in the direction of $\mathbf{q}$. $\langle \mathbf{M(q)} \rangle$ is effectively the thermal average of the Fourier transform of the magnetic moment distribution and should not be confused with the (macroscopic) magnetization. If the scattering is due to spin only $\mathbf{M}(\mathbf{q})$ is

$$\mathbf{M}_s(\mathbf{q}) = -2\mu_B \int \boldsymbol{\rho}_s(\mathbf{r}) \exp(i\mathbf{q} \cdot \mathbf{r}) d\mathbf{r}, \tag{4.28}$$

where the electron spin density is

$$\boldsymbol{\rho}_s(\mathbf{r}) = \sum_i \delta(\mathbf{r} - \mathbf{r}_i)\mathbf{s}_i. \tag{4.29}$$

The result is similar if orbital angular momentum is included, with $\mathbf{M}_l(\mathbf{q})$ being effectively the Fourier transform of the current density of the orbital motion and $\mathbf{M}(\mathbf{q}) = \mathbf{M}_s(\mathbf{q}) + \mathbf{M}_l(\mathbf{q})$. $\mathbf{M}(\mathbf{q})$ is called the magnetic form factor.

We can make the important observation that the scattering depends only on the part of the magnetization perpendicular to the scattering vector. This rule applies for polarized neutrons as well and is extremely important for the geometrical setup of an experiment. One often defines the magnetic interaction vector as:

$$\mathbf{M}_\perp(\mathbf{q}) = \hat{\mathbf{q}} \times (\mathbf{M}(\mathbf{q}) \times \hat{\mathbf{q}}), \tag{4.30}$$

which is the component of $\mathbf{M}$ perpendicular to $\mathbf{q}$. Now I will proceed to the theory of a scattering experiment with polarized neutrons and arrive at the results that are important for the scattering experiments in this work.

Chapter 5

Polarised neutron scattering

When the neutron beam is polarised in a specific direction, it is possible to obtain additional information about magnetic structure as compared to a randomly polarised neutron beam. In this section I will go through the theory of scattering of polarised neutrons. The theory of elastic scattering of polarised neutrons was developed by M. Blume in 1963 [26] and a famous paper by Moon et al. in 1969 [27] further explained the basics of polarisation analysis for both elastic and inelastic scattering. My summary of the theory will be based on the ideas from these papers and by section 2.8.5. in ref. [28] by Bertrand Roessli and Peter Böni. I will continue to restrict my discussion to elastic scattering as the aim is to develop the theory necessary to understand my data.

5.1 Polarisation of the beam

The neutron is a spin $\frac{1}{2}$ particle and if a certain quantization direction (say the z - direction) is chosen the spin of a neutron can be described as either up (This will be denoted $|\uparrow\rangle$ or $\binom{1}{0}$) or down ($|\downarrow\rangle$ or $\binom{0}{1}$) with respect to that axis. If the neutron spins are not randomly oriented but are made to point preferably in a certain direction (by applying a magnetic field) we say that the beam is polarised. The polarisation of the beam along the z - direction can be defined as

$$p \equiv p^z = \frac{1}{s} \langle S^z \rangle . \tag{5.1}$$

The polarisation is a number in the range $-1 \leq p \leq 1$ and can be written in terms of the number of neutrons with spin up ($n_\uparrow$) and down ($n_\downarrow$) with respect to the polarisation axis:

$$p = \frac{n_\uparrow - n_\downarrow}{n_\uparrow + n_\downarrow}. \tag{5.2}$$

The polarisation can be expressed as a function of the probabilities of the neutrons to be up and down ($p_\uparrow$ and $p_\downarrow$):

$$p = p_\uparrow - p_\downarrow. \tag{5.3}$$

Since the spin of a spin $\frac{1}{2}$ particle is either up or down we must have $p_\uparrow + p_\downarrow = 1$ and we can write

$$p = p_\uparrow - p_\downarrow = 2p_\uparrow - 1 = -2p_\downarrow + 1 \tag{5.4}$$

and

$$p_\uparrow = \frac{1+p}{2}, \tag{5.5}$$

$$p_\downarrow = \frac{1-p}{2}. \tag{5.6}$$

One usually defines a quantity known as the flipping ratio (FR) which can be easily measured and can be used to obtain the experimental value of the polarisation. In experiments one typically aims at a perfectly polarised beam ($p = 1$). This is not obtainable in real life, but fortunately it is usually possible to correct for the imperfectly polarised beam when the flipping ratio is measured. The correction procedure is described in section 5.4. The flipping ratio is (not surprisingly) defined as

$$FR = \frac{n_\uparrow}{n_\downarrow} = \frac{p_\uparrow}{p_\downarrow} = \frac{1+p}{1-p}, \tag{5.7}$$

and the polarisation can be written in terms of the flipping ratio:

$$p = \frac{n_\uparrow - n_\downarrow}{n_\uparrow + n_\downarrow} = \frac{n_\uparrow/n_\downarrow - 1}{n_\uparrow/n_\downarrow + 1} = \frac{FR-1}{FR+1}. \tag{5.8}$$

5.2 Polarisation analysis

Let us assume for now that the beam is perfectly polarised with all neutron spins pointing up and let us look at the elastic scattering processes that can occur.

In the experiment we look at two different kinds of processes in which the neutrons interact with the sample:

- Non spin flip processes (NSF), where the spin states of the scattered neutrons are not changed by the sample ($|\uparrow\rangle \rightarrow |\uparrow\rangle$ or $|\downarrow\rangle \rightarrow |\downarrow\rangle$).
- Spin flip processes (SF), where the spin states of the scattered neutrons are changed by the sample ($|\uparrow\rangle \rightarrow |\downarrow\rangle$ or $|\downarrow\rangle \rightarrow |\uparrow\rangle$).

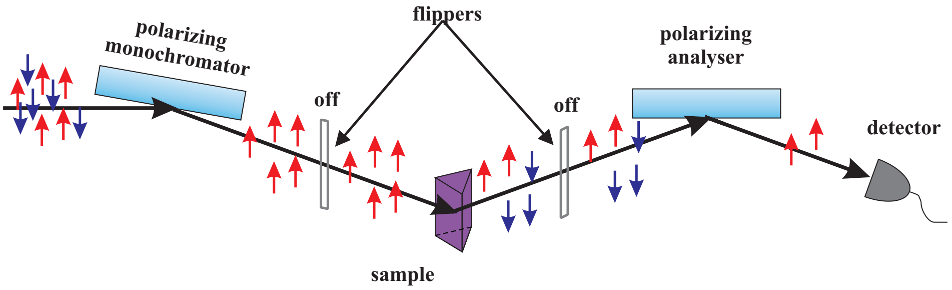

Figure 5.1: ***NSF experiment.*** *The neutrons are polarised in the monochromator so that all neutrons are* $|\uparrow\rangle$. *The polarised neutrons travel to the sample and interact with it in some way that may or may not flip the neutron spins. The scattered neutrons travel to the polarising analyzer and only the ones that are still* $|\uparrow\rangle$ *are reflected to the detector, giving the NSF intensity. Both flippers are switched off.*

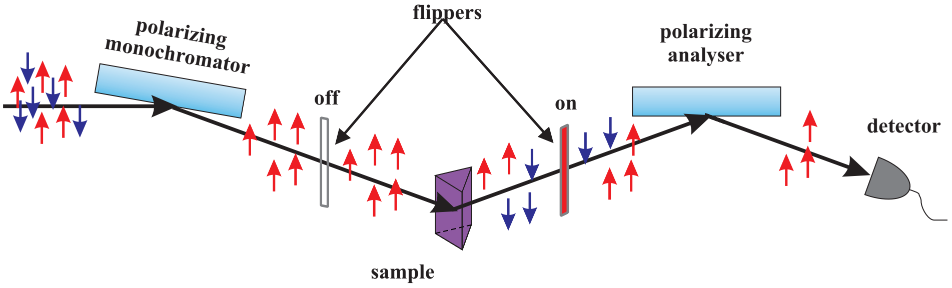

Figure 5.2: ***SF experiment.*** *The neutrons are polarised in the monochromator so that all neutrons are* $|\uparrow\rangle$. *The polarised neutrons travel to the sample and interact with it in some way that may or may not flip the neutron spins. After the sample the scattered neutrons travels through a spin flipper that rotates their spins by 180 °. When the scattered neutrons reach the polarising analyzer the neutrons that had their spin flipped by the sample are now* $|\uparrow\rangle$ *and are thus reflected to the detector, giving the SF intensity.*

In practice the experiment is done in such a way that for every $\mathbf{q}_{hkl}$ data point the intensity is measured twice. First the NSF intensity is measured and then the SF intensity. The NSF intensity is measured with a polarised neutron beam and a polarising analyser as seen in figure 5.1. The polarising analyser [1] only reflects the spin up neutrons into the detector and therefore only neutrons that were not flipped by the sample (NSF neutrons) are measured. This gives the NSF intensity.

To measure the SF processes a spin flipper between the sample and the analyser (or between monochromator and sample) is turned on. The flipper turns the spin of the scattered neutrons 180° and the neutrons that changed their spin state during the interaction with the sample are now the ones being reflected from the analyser to the detector (see fig.5.2). For technical details see the section about the TASP instrument (7.2). If one wants to distinguish $|\uparrow\rangle \rightarrow |\uparrow\rangle$ from $|\downarrow\rangle \rightarrow |\downarrow\rangle$ and $|\uparrow\rangle \rightarrow |\downarrow\rangle$ from $|\downarrow\rangle \rightarrow |\uparrow\rangle$, two spin flippers are necessary. In the present experiment only one flipper was used and we therefore only see the processes $|\uparrow\rangle \rightarrow |\uparrow\rangle$ and $|\uparrow\rangle \rightarrow |\downarrow\rangle$ (assuming total polarisation, $p = 1$).

5.3 Scattering cross-sections for polarised neutrons

Let us now see how the neutrons can interact with the sample and how the NSF and SF intensities give information about the sample. In general the scattering can be classified as either nuclear scattering or magnetic scattering (or sometimes both). I will assume the nuclear spin to be zero (I = 0) and treat nuclear scattering and magnetic scattering from the spins of unpaired electrons separately. When we take the spin of the neutron into account, the differential elastic cross-section is (from equation 4.7)

$$\frac{d\sigma}{d\Omega} = e^{-2\mathrm{W}} \left(\frac{m_n}{2\pi\hbar^2}\right)^2 \left|\left\langle \mathbf{k}_f \boldsymbol{\sigma}_f \left| \hat{V} \right| \mathbf{k}_i \boldsymbol{\sigma}_i \right\rangle\right|^2, \tag{5.9}$$

where the spin states $\boldsymbol{\sigma}_i$ and $\boldsymbol{\sigma}_f$ of the neutron before and after the interaction with the sample can be either $|\uparrow\rangle = \binom{1}{0}$ or $|\downarrow\rangle = \binom{0}{1}$.

5.3.1 Nuclear scattering

If we consider purely nuclear scattering, the potential in the matrix element is the Fermi pseudo-potential (4.8) and the matrix element that needs to be calculated is $\langle \boldsymbol{\sigma}_f \left| b_j \right| \boldsymbol{\sigma}_i \rangle$ (b_j being the scattering length). For the different possible spin states before and after the scattering this gives:

---

[1] A polarisation experiment can be done with a polarising monochromator and analyser as explained here. One could equally well use conventional monochromators and analysers together with polarising devices like benders and that is actually what was done in the TASP experiment,

$$\langle \sigma_f | b | \sigma_i \rangle = b \langle \sigma_f | \sigma_i \rangle = b\delta_{\sigma_f,\sigma_i} = \left\{ \begin{array}{l} b \left\{ \begin{array}{c} |\uparrow\rangle \rightarrow |\uparrow\rangle \\ |\downarrow\rangle \rightarrow |\downarrow\rangle \end{array} \right\} NSF \\ 0 \left\{ \begin{array}{c} |\uparrow\rangle \rightarrow |\downarrow\rangle \\ |\downarrow\rangle \rightarrow |\uparrow\rangle \end{array} \right\} SF \end{array} \right. , \tag{5.10}$$

where the Kronecker delta $\delta_{\sigma_f,\sigma_i}$ comes about because the spin states are orthogonal and normalized. Thus coherent nuclear scattering gives rise to NSF scattering only.

5.3.2 Magnetic scattering

If we consider magnetic scattering the (effective) potential is (see chapter 7 in [21]).

$$\hat{V}_m(\mathbf{q}) = -\frac{\gamma r_0}{2\mu_B} \boldsymbol{\sigma} \cdot \mathbf{M}_\perp(\mathbf{q}) = -\frac{\gamma r_0}{2\mu_B} \sum_\zeta \sigma_\zeta \cdot M_{\perp\zeta}(\mathbf{q}), \tag{5.11}$$

where $\zeta = x, y, z$. $\mathbf{M}_\perp(\mathbf{q})$ is the magnetic interaction vector defined in (4.30). σ_ζ are the Pauli matrices:

$$\sigma_x = \begin{pmatrix} 0 & 1 \\ 1 & 0 \end{pmatrix}, \sigma_y = \begin{pmatrix} 0 & -i \\ i & 0 \end{pmatrix}, \sigma_z = \begin{pmatrix} 1 & 0 \\ 0 & -1 \end{pmatrix}. \tag{5.12}$$

The matrix elements become (see fig. 5.3):

$$\left\langle \boldsymbol{\sigma}_f \left| \hat{V}_m(\mathbf{q}) \right| \boldsymbol{\sigma}_i \right\rangle = -\frac{\gamma r_0}{2\mu_B} \left\{ \begin{array}{cc} M_{\perp z}(\mathbf{q}) & |\uparrow\rangle \rightarrow |\uparrow\rangle \\ -M_{\perp z}(\mathbf{q}) & |\downarrow\rangle \rightarrow |\downarrow\rangle \\ M_{\perp x}(\mathbf{q}) - iM_{\perp y}(\mathbf{q}) & |\uparrow\rangle \rightarrow |\downarrow\rangle \\ M_{\perp x}(\mathbf{q}) + iM_{\perp y}(\mathbf{q}) & |\downarrow\rangle \rightarrow |\uparrow\rangle \end{array} \right. \begin{array}{l} \left.\begin{array}{c} \\ \\ \end{array}\right\} NSF \\ \left.\begin{array}{c} \\ \\ \end{array}\right\} SF \end{array} . \tag{5.13}$$

Now we can state the ground rule of magnetic scattering of polarised neutrons:

- The NSF intensity only gives information about *magnetic moments parallel to the polarisation direction.*
- The SF intensity only gives information about *magnetic moments perpendicular to the polarisation direction.*

This together with the more general rule that neutrons only see moments perpendicular to $\mathbf{q}$ forms the basis of what we can learn from polarisation analysis.

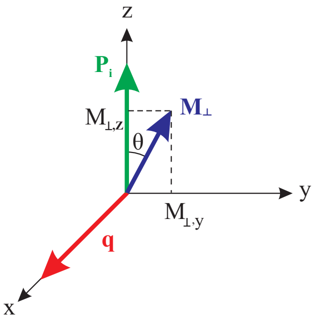

Figure 5.3: ***Experimental geometry.*** *The scattering vector* $\mathbf{q}$ *is along the x - axis, the incident polarisation* $\mathbf{P}_i$ *is along the z - axis and* $\mathbf{M}_\perp$ *is in the y-z plane with an angle* θ *with respect to the z - axis.*

The geometry in our experiment is shown in figure 5.3. The scattering vector $\mathbf{q}$ lies in the horizontal plane and is for simplicity placed along the x - axis. The polarisation direction $\mathbf{P}_i$ of the incident beam is along the positive z - direction, and $\mathbf{M}_\perp$ is in the y-z plane describing an angle θ with respect to the z - axis. This geometry makes it possible to obtain the components of the spin directions perpendicular to the scattering vector directly from the NSF and SF intensities. For a purely magnetic peak the NSF and SF cross-sections are (from eqs. (5.9) and (5.13)):

$$\sigma^{NSF} = CM^2_{\perp,z} = CM^2_\perp cos^2(\theta), \tag{5.14}$$

$$\sigma^{SF} = CM^2_{\perp,y} = CM^2_\perp sin^2(\theta), \tag{5.15}$$

where the constant C is the product of the prefactors in (5.9) and (5.13). The angle θ can be found from the NSF and SF intensities as:

$$\frac{\sigma^{SF}}{\sigma^{NSF}} = \frac{\sin^2(\theta)}{\cos^2(\theta)} = \tan^2(\theta). \tag{5.16}$$

Thus the components of the spin directions in the sample perpendicular to the scattering vector can be found from the ratio of SF and NSF intensities.

5.3.3 Combined nuclear and magnetic scattering

Sometimes it is not possible to study purely nuclear or purely magnetic scattering and one then has to take the combined scattering into account. In fact, the combined nuclear-magnetic scattering is the basics of most polarisation filters. The total polarisation dependent cross-section is (from section 2.8.5 in [28])

$$\sigma = F_N F_N^* + \mathbf{D}_\perp \cdot \mathbf{D}_\perp^* + \mathbf{P}_i \cdot (\mathbf{D}_\perp F_N^* + \mathbf{D}_\perp^* F_N) + i\mathbf{P}_i \cdot (\mathbf{D}_\perp^* \times \mathbf{D}_\perp)\,, \tag{5.17}$$

where $\mathbf{D}_\perp = \mathbf{D}_\perp(\mathbf{q}) = \frac{\gamma r_0}{2\mu_B}\mathbf{M}_\perp(\mathbf{q})$ is the magnetic interaction vector defined in a slightly different way than in section 4.2.3. The Debye-Waller factor has been ignored for simplicity. If the incident polarisation is $\mathbf{P}_i = 0$ this is reduced to a sum of the magnetic and nuclear scattering cross-sections. In an experiment with polarised neutrons $\mathbf{P}_i \neq 0$ and the two last terms can come into play. The term $\mathbf{P}_i \cdot (\mathbf{D}_\perp F_N^* + \mathbf{D}_\perp^* F_N)$ is the magnetic-nuclear interference term and is nonzero only for reflections that have both nuclear and magnetic scattering. The last term in the cross-section is the chiral term and is nonzero only when $\mathbf{D}_\perp \neq \mathbf{D}_\perp^*$ as is the case for helical structures. The polarisation of the scattered beam, $\mathbf{P}_f$ can be found from

$$\begin{aligned}\mathbf{P}_f \sigma = {} & \mathbf{P}_i F_N F_N^* \\ & + (-1)\mathbf{P}_i (\mathbf{D}_\perp \cdot \mathbf{D}_\perp^*) + \mathbf{D}_\perp (\mathbf{P}_i \cdot \mathbf{D}_\perp^*) + \mathbf{D}_\perp^* (\mathbf{P}_i \cdot \mathbf{D}_\perp) \\ & + \mathbf{D}_\perp F_N^* + \mathbf{D}_\perp^* F_N + i(\mathbf{D}_\perp F_N^* - \mathbf{D}_\perp^* F_N) \times \mathbf{P}_i \\ & + i\mathbf{D}_\perp \times \mathbf{D}_\perp^* \end{aligned} \tag{5.18}$$

From (5.17) and (5.18) we get the already stated result that purely nuclear scattering will leave the polarisation state of the beam unchanged. For an unpolarised incident beam one obtains from (5.17) (with $\mathbf{D}_\perp = \mathbf{D}_\perp^*$ and $F_N = F_N^*$)

$$\sigma = F_N^2 + D_\perp^2 \tag{5.19}$$

and from (5.18)

$$\mathbf{P}_f = \frac{2F_N \mathbf{D}_\perp}{\sigma} = \frac{2F_N \mathbf{D}_\perp}{F_N^2 + D_\perp^2}. \tag{5.20}$$

The beam will thus be fully polarised if $F_N^2 = D_\perp^2$ and the way a neutron beam is polarised in many experiments is exactly by utilizing materials that satisfies this condition.

5.4 Correction for imperfect polarisation

In a real experiment the polarisation of the beam is never exactly 1 and this means that some events that are really SF events are measured as NSF events and vice versa. We have to take this into account and correct our data to get the true values of σ^{NSF} and σ^{SF}. A simple way to correct for the imperfect polarisation of the beam is to measure the NSF and SF intensities of a purely nuclear peak and use this to calculate the flipping ratio (5.7) in the experiment. From the FR and the measured intensities one can find the true cross-sections in the following way.

If I^{NSF} and I^{SF} are the measured spin-flip and non-spin-flip intensities in the experiment and σ^{NSF} and σ^{SF} are the corresponding (true) cross-sections it is easy to see that:

$$I^{NSF} = \sigma^{SF} \cdot p_{\downarrow} + \sigma^{NSF} \cdot p_{\uparrow} \tag{5.21}$$

$$I^{SF} = \sigma^{SF} \cdot p_{\uparrow} + \sigma^{NSF} \cdot p_{\downarrow} \tag{5.22}$$

or

$$\begin{pmatrix} I^{NSF} \\ I^{SF} \end{pmatrix} = \begin{pmatrix} p_{\uparrow} & p_{\downarrow} \\ p_{\downarrow} & p_{\uparrow} \end{pmatrix} \begin{pmatrix} \sigma^{NSF} \\ \sigma^{SF} \end{pmatrix} \tag{5.23}$$

If we label these matrices (vectors) $\mathbf{I}$, $\mathbf{P}$ and $\boldsymbol{\sigma}$ we can get the (true) cross-section

$$\boldsymbol{\sigma} = \mathbf{P}^{-1}\mathbf{I}. \tag{5.24}$$

The matrix $\mathbf{P}$ can be written

$$\mathbf{P} = \frac{1}{2} \begin{pmatrix} 1+p & 1-p \\ 1-p & 1+p \end{pmatrix}. \tag{5.25}$$

The value of p can be calculated from the flipping ratio from (5.8) and $\mathbf{P}^{-1}$ can immediately be calculated. In order to correct for the imperfect polarisation of the beam, all we have to do is measure the flipping ratio, calculate $\mathbf{P}^{-1}$ and multiply this with the measured NSF and SF intensities to obtain the cross-sections.

The way FR is found experimentally is to measure a purely structural reflection ($\sigma^{SF} = 0$). FR is then (from 5.7 and 5.23) the ratio of the SF to the NSF intensity.

$$FR = \frac{I^{NSF}}{I^{SF}} \tag{5.26}$$

The actual calculation of the FR in the experiment is described in section 8.4 and proved a lot more difficult for the actual sample then the idealized procedure described above.

Chapter 6

Small angle neutron scattering

Small angle neutron scattering (SANS) is a technique that is suited for investigating structures on the nanometer scale. An introduction to SANS can be found in [20] and I will here give my own short introduction to SANS. The starting point is again (4.7), but because the scattering takes place at small angles some useful approximations will apply. In order to distinguish the magnetic from the nuclear signal the experiment should be performed with polarised neutrons. Such an experiment is called a SANSPOL experiment.

6.1 The SANS cross section

To begin with we will think of the scattering system as a collection of identical particles with a length-scale in the nanometer area. The differential elastic cross section for combined nuclear and magnetic scattering looks like.

$$\frac{d\sigma}{d\Omega} = \left| \sum_j \left(b_j - \frac{\gamma r_0}{2\mu_B} \boldsymbol{\sigma} \cdot \mathbf{M}_\perp(\mathbf{r}_j) \right) e^{i\mathbf{q}\cdot\mathbf{r}_j} \right|^2 . \tag{6.1}$$

If we choose the z-axis as quantization axis for the neutron spin this is reduced to

$$\frac{d\sigma}{d\Omega} = \left| \sum_j \left(b_j - \frac{\gamma r_0}{2\mu_B} \sigma_z M_{\perp z}(\mathbf{r}_j) \right) e^{i\mathbf{q}\cdot\mathbf{r}_j} \right|^2 . \tag{6.2}$$

With a polarisation $\mathbf{P}_i$ this gives the same as in (5.17) without the chiral term (which would follow from a thorough quantum mechanical derivation). If, in an experiment one measures the intensity with both positively and negatively polarised neutrons (I^+ and I^-) and subtracts these one gets two times the nuclear-magnetic interference term. In this way it is possible to get information about magnetic structures event when the magnetic cross-section is just a small perturbation to the structural. If we now define an effective magnetic scattering length as

$$b_{m,j} = \frac{\gamma r_0}{2\mu_B}\sigma_z M_{\perp z}(\mathbf{r}_j) \tag{6.3}$$

and divide the sum into one over the nuclei and spins in each particle and one sum over the N identical particles (like the usual unit cell- and lattice sums) we can proceed(following section 5.1 of [20]):

$$\frac{d\sigma}{d\Omega} = \left|\sum_j \left(b_j + b_{m,j}\right) e^{i\mathbf{q}\cdot\mathbf{r}_j}\right|^2 \tag{6.4}$$

$$= \left|\sum_J e^{i\mathbf{q}\cdot\mathbf{R}_J}\right|^2 \left|\sum_j \left(b_j + b_{m,j}\right) e^{i\mathbf{q}\cdot\mathbf{r}_j}\right|^2 \tag{6.5}$$

$$\equiv N\left|S(\mathbf{q})\right|^2 \left|\sum_j (b_j + b_{m,j}) e^{i\mathbf{q}\cdot\mathbf{r}_j}\right|^2, \tag{6.6}$$

where the structure factor $S(\mathbf{q})$ has been defined. If the positioning of the particles relative to each other is random (no interference) the structure factor is $S(\mathbf{q}) = 1$.

In SANS we only consider small scatting vectors, so that we can use the approximation that the phase of the exponential $e^{i\mathbf{q}\cdot\mathbf{r}}$ does not change significantly between neighbouring atoms. This condition can be stated

$$qa \ll 2\pi, \tag{6.7}$$

where a is the inter-atomic distance. When this assumption is true the sample will not scatter as a crystal, but as a continuum. The sum over the particles in 6.6 can be turned into an integral over the particle volume V. The scattering lengths will now be replaced by scattering length densities, which could be defined as

$$\rho = \frac{1}{V_0}\sum_{\text{f.u.}} b, \tag{6.8}$$

where the sum is over one formula unit with volume V_0. The SANS cross section now reads

$$\left.\frac{d\sigma}{d\Omega}\right|_{\text{SANS}} = N\left|S(\mathbf{q})\right|^2 \left|\int \left(\rho_b(\mathbf{r}) + \rho_m(\mathbf{r})\right) e^{i\mathbf{q}\cdot\mathbf{r}} dV\right|^2 \tag{6.9}$$

If the particles are in a solution with (constant) scattering length densities $\rho_{b,\text{solvent}}$ and $\rho_{m,\text{solvent}}$ these two extra terms have to be added to the cross section. We define the scattering length density contrasts with respect to the solvent as

$$\Delta\rho_b(\mathbf{r}) = \rho_b(\mathbf{r}) - \rho_{b,\text{solvent}} \quad , \quad \Delta\rho_m(\mathbf{r}) = \boldsymbol{\rho}_m(\mathbf{r}) - \rho_{m,\text{solvent}} \tag{6.10}$$

and note that the dimensions of the solvent is orders of magnitude larger than the size of the particles. Therefore the scattering from the solvent will be at so low q-values that it will not be observed in an experiment and can thus be ignored. The SANS cross section is therefore rewritten

$$\left.\frac{d\sigma}{d\Omega}\right|_{\text{SANS}} = N\left|S(\mathbf{q})\right|^2 \left|\int \left(\Delta\rho_b(\mathbf{r}) + \Delta\rho_m(\mathbf{r})\right) e^{i\mathbf{q}\cdot\mathbf{r}} dV\right|^2 \tag{6.11}$$

6.1.1 Useful approximations

Before proceeding to the model of SANS on hemo-ilmenite I will briefly mention two useful approximations known as the Guinier approximation and the Porod law, which are valid for small and large q respectively.

First it is noted that for monodisperse homogeneous particles the SANS cross section (6.11) can be reduced to

$$\begin{aligned}\left.\frac{d\sigma}{d\Omega}\right|_{\text{SANS}} &= N\left|S(\mathbf{q})\right|^2 \left|\left(\Delta\rho_b(\mathbf{r}) + \Delta\rho_m(\mathbf{r})\right) \int e^{i\mathbf{q}\cdot\mathbf{r}} dV\right|^2 \\ &\equiv NV^2 \left|S(\mathbf{q})\right|^2 P(\mathbf{q}) \left|\left(\Delta\rho_b(\mathbf{r}) + \Delta\rho_m(\mathbf{r})\right)\right|^2 ,\end{aligned} \tag{6.12}$$

where $P(\mathbf{q})$ is the so-called particle form factor.

$$P(\mathbf{q}) = \left|\frac{1}{V}\int dV e^{i\mathbf{q}\cdot\mathbf{r}}\right|^2 . \tag{6.13}$$

Just like one measures the structural and magnetic form factors in a diffraction experiment the particle form factor is what one measures in SANS. Of course some of the assumptions leading to the simplification in (6.12) may have to be lifted in a real system and this may complicate things considerably.

For really small values of the scattering vector, say $qR \ll 2\pi$, R being the particle radius, the following apply (see 5.1.6. in [20]):

$$P(q) \approx \exp\left(-\frac{1}{3}\left(qR_g\right)^2\right) , \tag{6.14}$$

where R_g is the objects radius of gyration. This is the so-called Guinier approximation. If on the other hand the angles are large, say $qR \gg 2\pi$, the Porod law applies and reads (see 5.1.7. in [20]):

$$P(q) \propto q^{-4} . \tag{6.15}$$

6.2 SANSPOL on hemo-ilmenite - a simple model

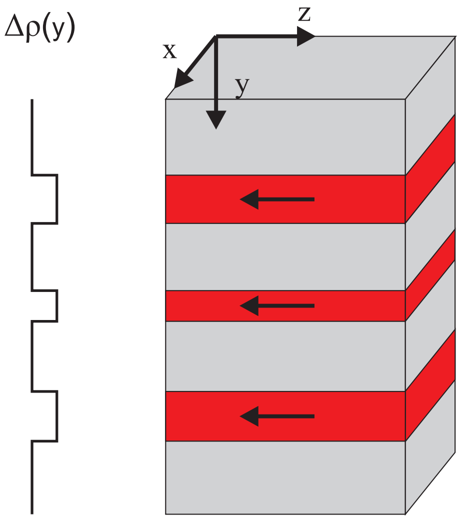

Figure 6.1: ***Model of the scattering length density in hemo-ilmenite.*** *The hematite lamellae (red) are assumed to be large flat sheets with some distribution of scattering length density. Between the hematite layers the ilmenite (gray) will play the role of the solvent in a SANS experiment. Different models of the scattering length density distribution in the lamellae can be applied.*

Because SANS probe nano scale structures it appears to be suited for investigating the magnetism in the lamellae in hemo-ilmenite. The ilmenite will then play the role of the solvent and the lamellae as the nano scale particles. To get some hints about how the experiment should be performed to obtain information about the magnetic structure of the lamellae, a simple model for the signal from SANS on hemo-ilmenite was developed. The model contains some very crude approximations and is by no means to be taken as an attempt to get an accurate simulation of the scattering.

The sample is assumed to be a stack of homogeneous flat layers of hematite and ilmenite stretching in the x- and z- directions (see fig. 6.1). This multilayer structure is of course a crude approximation to the real system, but has the great advantage that the scattering length density changes in only the y-direction. We assume that there is no correlation between the lamellae, meaning that the inter particle structure factor is one. The SANS intensity is then (assuming **q** is along the y-axis)

$$I(\mathbf{q}) = N \left| \int_{-\infty}^{+\infty} \left(\Delta\rho_b(y) + \Delta\rho_m(y)\right) e^{iqy} dy \right|^2 . \qquad (6.16)$$

The integral is simply the one dimensional Fourier transform of the sum of the nuclear and magnetic scattering length densities in the y-direction. To lift the assumption that the lamellae are of the same size, the scattering length density is convoluted with a size distribution $D(l)$ for the lamellae.

$$I(\mathbf{q}) = N \int_{d_{min}}^{d_{max}} D(l) dl \left| \int_{-\infty}^{+\infty} \left(\Delta\rho_b(y) + \Delta\rho_m(y)\right) e^{iqy} dy \right|^2 . \tag{6.17}$$

From TEM observation a rough estimate of the size distribution can be given [18]. The observation suggests that there are two generations of lamellae with average widths of around 1-2 nm and 20-30 nm respectively. There are also much larger lamellae, but these will not be seen in the SANS signal. As size distribution in the model a sum of the two Gaussian size distributions shown in figure 6.2 is used as a starting point. The amplitudes of the two Gaussians can be chosen at will.

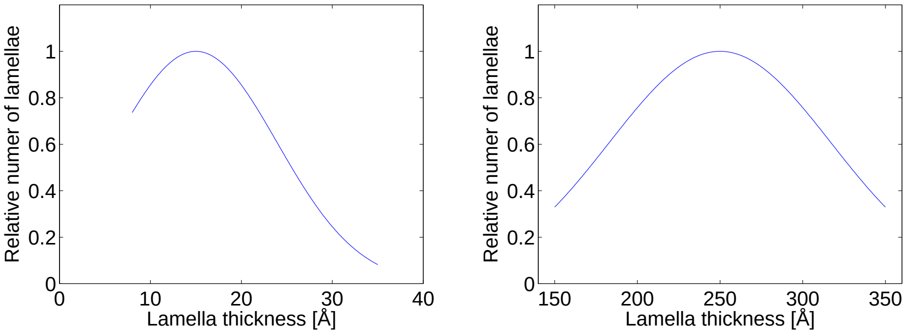

Figure 6.2: ***Size distribution of lamellae.*** *Two generations of lamellae with different characteristic sizes are assumed in the model.*

A central idea behind the model is to get an idea about whether or not a SANSPOL experiment can distinguish between different models for the magnetic structure of hemo-ilmenite. With this in mind all that is left is to make scattering length density profiles that represents different models and then calculate the scattering cross section 6.17. The nuclear scattering length density contrast $\Delta\rho_b(y)$ is zero in the ilmenite host and in the hematite lamellae it is simply given by the large difference in scattering length density between Ti and Fe: $\Delta\rho_b(y) = 9.45\text{fm} - (-3.438\text{fm}) = 12.89\text{fm}$ (p.f.u.) The magnetic scattering length density contrast is also with respect to the ilmenite host and will therefore change when the PM ilmenite is magnetized by an applied field.

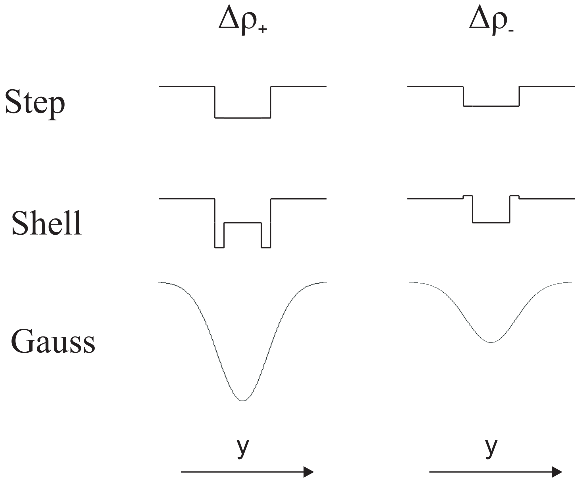

Figure 6.3: ***Scattering length density profiles of the model. Left:*** *The scattering length density profile as seen with a $|\uparrow\rangle$ neutron.* ***Right:*** *The scattering length density profile as seen with a $|\downarrow\rangle$ neutron.*

Three models were constructed for the scattering length density profiles of the lamellae (see fig. 6.3):

Shell: In this model the magnetic scattering length density is concentrated in narrow shells on the edge of the lamella. This is an attempt to model the profile of a lamellar magnetism model with the magnetization of the lamellae being concentrated in the interfaces with the ilmenite host.

Step: In this model the scattering length density profile is a step function, meaning that the scattering length density is homogeneous in the lamella. This model could for example apply to a magnetization being dominated by spin canting in the whole lamella.

Gauss: In this model both the nuclear and magnetic scattering length density profiles are Gaussians with FWHM equal to the lamellae thickness. This is an attempt to simulate a more diffuse interface between the lamella and the host.

A maximal value of $\Delta\rho_m$ can be estimated from the maximal $5/2\mu_B$ magnetic moment of Fe^{3+} of which there are two per formula unit giving a $\Delta\rho_m = 13.5$ fm (with no magnetization of the ilmenite). This was used as a starting value for the shell model. For the other models $\Delta\rho$ was normalized to the width of the lamella in order to get the same total lamellar moment.

The polarisation was $p = 0.97$ in all models. The modeling was done with MATLABs FFT (fast Fourier transform) function for a few different size distributions, values of scattering length densities and for shell thickness of 5 Å and 20 Å. In general the signature of the largest lamellae is a dip in the intensity curve in the lower q range, whereas the small lamellae give rise to more pronounced oscillations at high q. To distinguish the shell model from the step model one has to look at high q values and we will keep this in mind when performing the experiment. An example of the model with a shell thickness of $d_{\text{shell}} = 5$ Å, $\Delta\rho_m = 13.5$ fm, $\Delta\rho_b = 12.89\,\text{fm}$ in the lamella and the size distribution if fig. 6.2 is given in figs. 6.4 and 6.5.

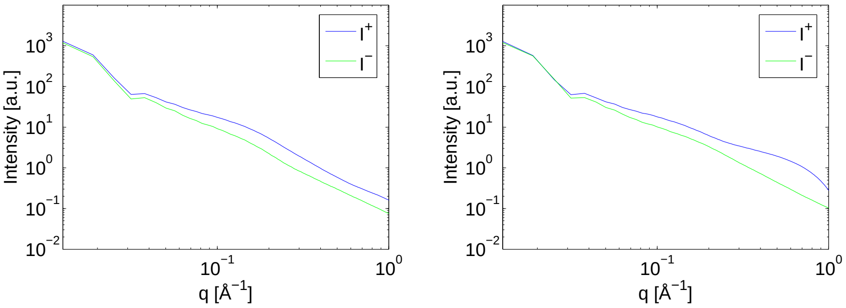

Figure 6.4: ***Model for SANSPOL signal from hemo-ilmenite.*** *The model is with $d_{shell} = 5$ Å, $\Delta\rho_m = 13.5$ fm, $\Delta\rho_b = 12.89$fm in the lamella and the size distribution of fig. 6.2.* ***left:*** *The step model.* ***right:*** *The shell model. The intensity profile from the two models are very similar. The dip around $q = 3 \cdot 10^{-2}$ Å^{-1} comes from the large lamellae.*

In the experiment on SANS-I we were unable to measure with both positively and negatively polarised neutrons as will be explained in section 10. The difference model in fig. 6.5 can be seen as an expectation for future experiments.

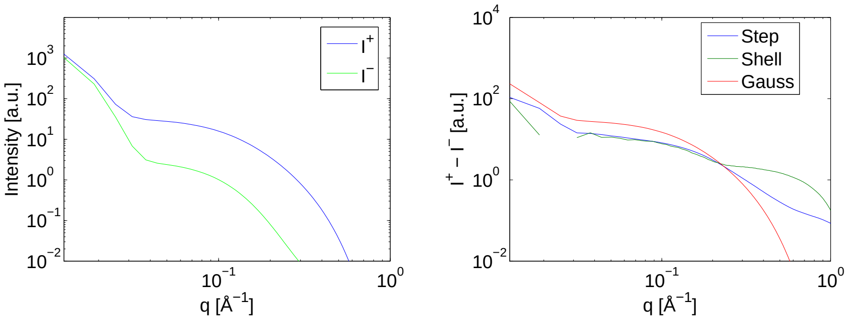

Figure 6.5: ***Model for SANSPOL signal from hemo-ilmenite.*** *The model is with* $d_{shell} = 5$ *Å,* $\Delta\rho_m = 13.5$ *fm,* $\Delta\rho_b = 12.89$ *fm in the lamella and the size distribution of fig. 6.2.* ***left:*** *The Gauss model. The intensity drops faster than the two other models.* ***Right****: The difference between scattering with the two polarisation states. To distinguish the step from the shell model one has to look at very low* q *or* q *larger than approximately 0.25* $Å^{-1}$*. The curve for the shell model is missing some points because the difference is negative at a few points around* $q = 2.5 \cdot 10^{-2}$ $Å^{-1}$*.*

Chapter 7

Neutron scattering Instruments

In this section I will explain the principles of how a triple axis spectrometer and a small angle neutron scattering instrument work. I will in some detail explain the TASP spectrometer and the SANS-I instrument at the Paul Scherrer Institute in Switzerland and how the configuration of the instruments was in my experiments. The MORPHEUS spectrometer is not very different from TASP and will only be described very briefly.

7.1 Triple Axis neutron Spectrometers

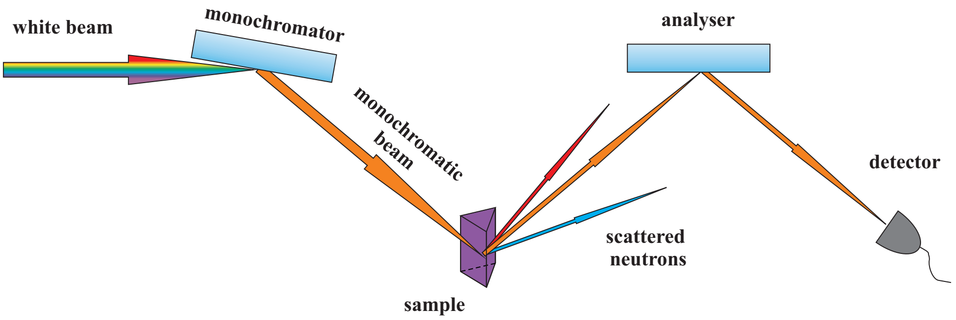

Figure 7.1: ***A Triple Axis Spectrometer (TAS).*** *This is the basic layout of a TAS. The white beam from the source enters from the left and is reflected by the monochromator to the sample, selecting one neutron energy to probe the sample with. The monochromatic beam is scattered by the sample by some interaction, and the analyser selects which energy is reflected to the detector.*

B. Brockhouse developed the technique of the triple axis neutron spectrometer (TAS) in the 1950ies [29], and since then it has been a widely used tool for investigating structures and dynamics of solids. Besides a neutron source the key elements of any TAS is the monochromator, the sample, the analyser, and the detector. Monochromator, sample and analyser can be rotated about their respective axes and thus constitute the three rotation axes in the TAS. The monochromator is a crystal that is oriented such that the neutrons of a chosen wavelength (energy) are Bragg reflected to the sample position. The analyser works in a similar way, but is placed between sample and detector. The analyser thus reflects scattered neutrons of a chosen wavelength to the detector. With this setup it is possible to measure both elastic and inelastic scattering in a wide momentum and energy space. The advantage of the TAS as compared to other neutron scattering instruments is that it, with a sufficiently high neutron flux from the source, enables the scientist to measure inelastic scattering from for example lattice vibrations (phonons) and magnetic excitations (spin waves). This has been widely utilized since the 1960ies.

Besides the monochromator and analyser crystals, there are a few key features that are common to most TAS's (and in general to neutron scattering instruments) and I will briefly mention some of the important ones here. A good reference for the more general features of triple axis spectrometers is [30].

7.1.1 Detector

The detector in a neutron scattering instrument in general works via some nuclear process that destroys the neutron and generates a current that can be amplified and measured in a counter. A common detector type is the ^{3}He detector, which is based on a chamber of a mixture of ^{3}He and some other gas like Argon. When neutrons enter the chamber they are captured by ^{3}He in the process:

$$n +^3 \mathrm{He} \rightarrow^3 \mathrm{H} + p + Energy. \tag{7.1}$$

The charged particles produced in the process have energy enough to ionize the Ar gas, and by applying a voltage difference between an anode and a cathode a cascade of charged particles is created, which can be amplified and detected. If an array of detectors is made, it is possible to get simultaneous information about the scattering in different positions, and one would have a so-called position sensitive detector (PSD).

7.1.2 Sample environment:

Due to the weak interaction of the neutron with matter it is possible to tailor the sample environment in various ways. The sample can be placed in cryostats or furnaces to control the temperature, inside large superconducting magnets or pressure cells to apply magnetic fields or pressure, etc.

7.1.3 Collimation sections:

There are often several collimators in a TAS to reduce the divergence of the beam and thus increase the spatial resolution of the instrument. In practice it can be done by a series of parallel sheets of heavily absorbing material or by small pinholes some meters apart.

7.1.4 Filters and monitors:

In order to get rid of higher order scattered neutrons the TAS is usually equipped with a filter that can be a block of beryllium which absorbs higher energy neutrons. (When a neutron with wavelength λ is Bragg reflected, so are neutrons with wavelengths $\lambda/2$, $\lambda/3$,... and these are called higher order neutrons). Usually there are a few monitors in strategic positions in the instruments. The monitors absorb a small fraction of the neutrons and counts the flux through different parts of the instrument. An advantage of the monitors is that one can count for a specified number of monitored neutrons in stead of counting for a specified time. In this way the scans will not be influenced by a unstable flux from the source during the measurement.

Besides the above mentioned, common features for all TAS's are radiation shielding blocks, shutters to control when the beam is on/off in the instrument and different kinds of focusing devices.

7.2 The TASP spectrometer at the Paul Scherrer Institute

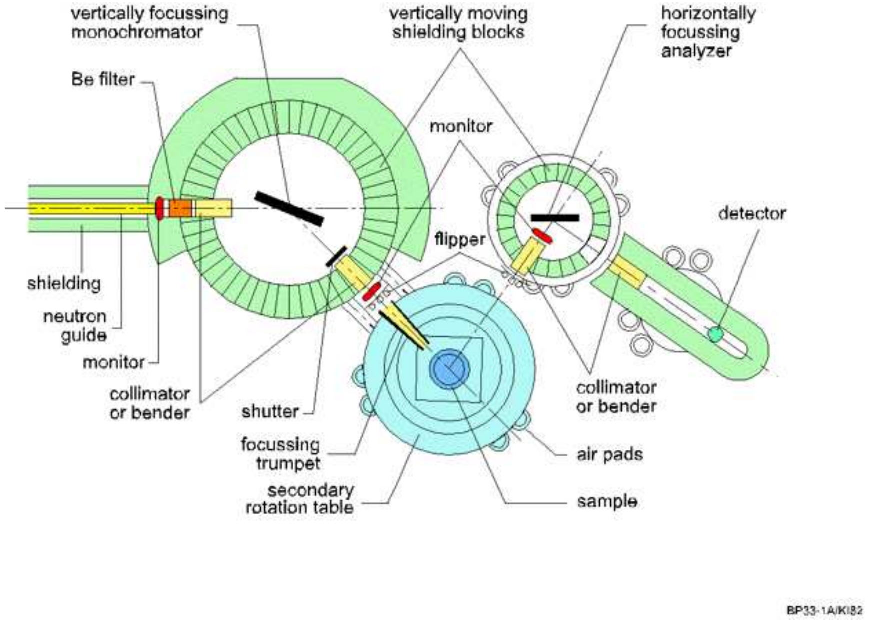

Figure 7.2: ***Layout of the TASP instrument.*** *The neutrons come from the could source and enters the instrument from the left. As the beam enters the spectrometer it passes through a beryllium filter, scatters off the monochromator and hits the sample. Between the monochromator and the sample a polarizing bender is inserted in order to hit the sample with a polarized beam. After hitting the sample the scattered neutrons, all with spin* $|\uparrow\rangle$*, are reflected by the analyser to the detector. Between sample and detector another bender is inserted in order to make sure only neutrons with spin* $|\uparrow\rangle$ *are detected. The sample is placed in a cryostat and a magnetic field to enable temperature and magnetic field control. In the beam path from monochromator to analyser there is a small magnetic field to maintain the polarization. Spin flippers are placed between monochromator and sample and between sample and analyser. Further details on the components of the spectrometer are described in the text. Figure from the TASP homepage. [31]*

TASP is a triple axis spectrometer, with the possibility to use polarization analysis (hence the abbreviation). In this section I will describe the parts of TASP that are important for the experiments that were performed on the hemo-ilmenite sample, and for my data analysis. The specifications of TASP is reported in ref. [32] and also on the instruments web page [31]. The layout of the spectrometer is given schematically in figure 7.2.

The cold neutrons used in the experiments are produced in the continuous SINQ spallation source and moderated in a moderator tank of liquid deuterium at a temperature of 25 K as described in section 4.1.2. The beam travels through a 54 m neutron guide before it hits the instrument. In the beginning of TASP the neutrons hit a monitor that measures the flux into the instrument and a beryllium filter that absorbs high energy neutrons.

To obtain a polarized beam a so called bender can be inserted in the beam. A bender is a stack of parallel polarizing supermirrors that are slightly bent to avoid line of sight from one end of the device to the other. This means that the neutrons have to make a reflection and thereby be polarized. The supermirrors in the benders are based on the fact that the critical angle of total reflection of a ferromagnetic film is given by (see [28] section 3.2)

$$\theta_c^{\pm} = \lambda\sqrt{N(b \pm p)/\pi}, \tag{7.2}$$

where N is the nuclear density, b is the nuclear scattering length, and p is the magnetic scattering length. The essence of (7.2) is that if one choses a material with $b = p$ only spin up neutrons $(+)$ will be reflected and the beam will therefore be polarized. Making a stack of different materials, a so-called supermirror, is a way of increasing the angle of total reflection. The bender before the sample makes it possible to hit the sample by a polarized beam (say all spins $|\uparrow\rangle$), and the bender after the sample makes it possible to detect only neutrons with a certain polarization direction ($|\uparrow\rangle$). The nuclear and magnetic scattering never exactly cancels and the polarization is therefore never 100%. This needs to be dealt with in the data analyzis (section 8.4).

In the entire instrument permanent magnets generate a small vertical guide field in the beam path and at the sample position a small magnetic field of is produced by a set of Helmholtz coils. In this way the polarization is maintained.

To perform polarization analysis, it is essential to be able to flip the spin of the neutrons. In TASP this is done with so called Mezei spin-flipper. There are two flippers, one placed between monochromator and sample and one between sample and analyser. The spin flippers, together with the polarizing monochromator and analyser makes it possible to see whether or not the neutron spins are flipped by interaction with the sample and this is the essence of polarization analysis. The principles of polarization analysis are described in section 5. The neutrons scattered from the analyser are detected by a ^{3}He detector. The instrument further includes collimation sections, monitors, shutters and focusing devices.

7.3 The MORPHEUS two-axis spectrometer

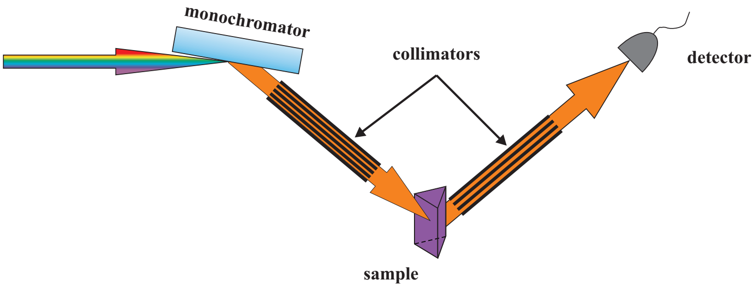

Figure 7.3: ***A two-axis spectrometer.*** *The layout of the two-axis spectrometer is like a TAS, but without the analyser. The white beam from the source enters from the left and are reflected by the monochromator to the sample, selecting one energy to probe the sample with. The monochromatic beam is scattered by the sample at an angle θ and the scattered neutrons are detected by the detector at an angle 2θ. If the scattering angle θ is equal to a Bragg-angle the scattering is elastic.*

I will here very briefly describe the MORPHEUS two-axis spectrometer which is a small instrument at the Paul Scherrer Institute, often used for aligning samples before experimenting on other instruments. Besides aligning my samples for the SANS experiment I used MORPHEUS to make a map of the $(00\bar{3})$ peaks of the sample in order to determine whether the sample is a single crystal or not.

A two-axis spectrometer is similar to a TAS except it does not have an analyser. A two-axis instrument is thus not suited for inelastic measurements. To resolve the (003) peaks better than in the TASP experiment, collimators were placed between guide and sample and between sample and detector. The collimators are simply closely placed parallel sheets of absorbing material. The neutrons with high divergence will hit the sheets and be absorbed whereas neutrons with low divergence will travel straight through the collimator without hitting the walls.

The MORPHEUS experiment was carried out with a wavelength of $\lambda = 4.717$ Å and collimations of 20' between guide and sample and 30' between sample and detector (meaning that neutrons with higher divergence than these values are absorbed). The (003) reflection was expected to be found at an angle of $\theta \approx 31°$ (from Braggs law) and it was indeed found close to this value. The 2θ angle was scanned around the peak center for a range of values of ω, which is the sample rotation. The result of the experiment is the map of the $(00\bar{3})$ peaks displayed in fig. 8.2.

7.4 Small angle neutron scattering instruments

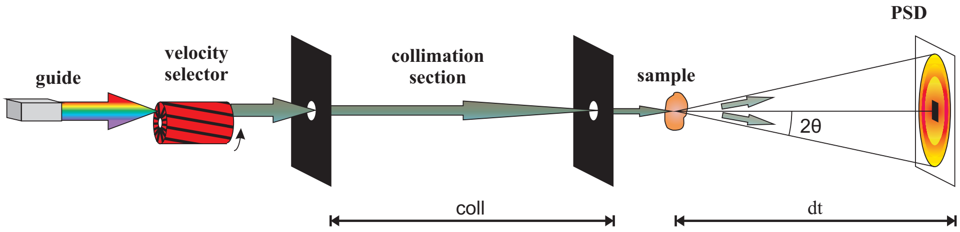

Figure 7.4: ***Layout of a SANS instrument.*** *The velocity selector is rotating at a speed of the order* 10^4 *rpm and absorbs neutrons with velocities that does not match the rotation speed. The collimation section consists of two pinholes that can be moved closer together or further apart, changing the collimation distance, coll. After the collimation section the beam reaches that sample, that could be inside a cryostat, a magnetic field or other environments. The scattering from the sample proceeds to the detector which is a PSD. The sample-detector distance dt can be adjusted to match the desired q-range.*

Small angle neutron scattering (SANS) is a technique that is suited for examining structures on the nanometer scale and is widely used especially for biological samples. The layout of a SANS instruments is quite simple and I will go through it in general terms here. In the next section I will describe the specific features of the SANS-I instrument in PSI. A sketch of the general layout is presented in fig. 7.4.

The instrument is placed at the end of a neutron guide that is fed by a cold source. The basic parts of a SANS instrument consists of a velocity selector, a collimation section, a sample in some sample environment and a detector inside a long evacuated tube.

Velocity selector: The first element of the instrument is a so-called velocity selector placed in the beam. The velocity selector is an axis with helical blades sticking out radially. The velocity selector is rotating at a speed (typically of the order 10^4 rpm) so that neutrons of a certain velocity (wavelength) passes through, whereas faster or slower neutrons are absorbed by the blades. The wavelength distribution is typically of the order $\frac{\Delta\lambda}{\lambda} \approx 10\%$.

Collimation section: After the velocity selector the beam enters the collimation section, which is simply two pinholes some meters apart. The distance between the pinholes can be adjusted by depending on how good collimation is needed. Typical collimation distances are 1 m - 20 m depending on the instrument.

Sample environment: Between the collimation section and the detector tube there is room for a variety of sample environments. Most importantly, when dealing with magnetic systems, the sample can be placed in a cryostat inside a magnetic field.

Detector: The detector is a PSD, which is placed inside an evacuated tube to avoid scattering in the air. To measure very small angles the detector has to be placed a distance of several meters away from the scattering sample. Therefore the detector tube is usually some 5- 20 m long. Usually the detector distance is matched to the collimation distance (since the angular resolution is limited by the collimation anyway). In the detector chamber there is a beam-stop that can be placed in front of the center of the beam to avoid burning the detector by hitting it with the direct beam.

Some SANS instruments also offer the possibility to work with polarised neutrons. The instrument will then be equipped with a polarising supermirror in the beam and possibly a spin flipper. The spin flipper gives the possibility of studying at the difference between the scattering signal from spin up and spin down neutrons.

7.5 The SANS-1 instrument at the Paul Scherrer Institute

The SANS-I instrument is the largest of the two small angle instruments at the Paul Scherer Institute. It has the option of working with a polarized beam and a spin flipper. I will give an account of the features of the instrument that is most important in order to understand the idea behind the hemo-ilmenite SANS experiment. A more thorough description of the instrument can be found in [34] upon which my description is based. Technical specifications of the instrument as well as experimental possibilities regarding sample environment can be found on the SANS-I homepage [33]. A photo of SANS-I is presented in figure 7.5.

The SANS-I instrument starts with a 43 cm gap in the guide, in which the velocity selector is placed together with the primary beam shutter and monitor. Opening or closing the shutter can then turn the beam on/off in the whole instrument and the monitor can be used to determine counting

Figure 7.5: ***Photo of the SANS-I instrument.*** *The telescopic tubes of the collimation section stretches parallel to the gray guide in the middle of the picture. The sample position is by the end of the collimation section. The beginning of the 20 m long detector tank is seen under the platform in front of the SANS-I control room. Photo from the SANS-I homepage [33].*

statistics. The rotation speed of the velocity selector can be adjusted up to 28300 r.p.m. giving an accessible wavelength range of 4.5 - 40 Å with $\frac{\Delta\lambda}{\lambda} = 10\%$.

The collimation section consists of sections of vacuum tube between 1 m and 4 m long that can be mounted in sequence with vacuum tight connections. The size of the pinholes can be varied by inserting apertures.

The ^{3}He detector (see 7.1.1) is a PSD with 128 × 128 pixels, each with a size of 7.5 × 7.5 mm^2. The PSD is placed on a rail in an evacuated steel tube and can be positioned at any position between 1 m and 20 m from the sample. Further, the detector can be displaced 50 cm in the horizontal direction if higher q values are desired. The maximal $q-$range for SANS-I is $6 \cdot 10^{-4}$Å^{-1} – 1.05 Å $^{-1}$. Beamstops of various sizes are placed in the evacuated tube and can be moved in and out remotely.

The sample can be placed in a wide range of environments and in the presented experiment it was placed in a cryostat inside the horizontal magnetic field of a 11 T superconducting magnet.

SANS-I has the capability of working with a polarized neutron beam. In ref. [35] the setup for SANSPOL on SANS-I is explained and characterized. I give a briefer explanation here and the reference should be consulted for elaborations.

To obtain a polarised neutron beam a polariser can be inserted in stead of the first collimation section, limiting the maximal collimation length to 15 m. The polariser is a v-shaped polarising Fe/Si supermirror that only transmits one spin state (see equation 7.2) and reflects the other. The transmitted beam that proceeds through the collimation section is polarised parallel to the beam direction. The efficiency of the polariser depends on the incident angle of the neutrons as well as the wavelength, and hence the polarisation of the beam at the sample position will depend on the collimation length. For wavelengths longer than 6 Å the polarisation is better than 97% for all collimation lengths. The transmission of the polariser is about 25% - 40% for wavelengths of 5 - 10 Å, for which the device was designed.

To maintain the polarisation there is a guide field of 1-2 mT in the flight path between polariser and sample. The guide field is obtained by magnetising iron plates by permanent FeNdB magnets. The instrument can be equipped with a radio frequency spin-flipper with an efficiency close to 100%. Unfortunately this can not be installed together with the 11 T horizontal magnet.

Chapter 8

TASP data analysis

In this chapter the methods to be used for the analysis of the TASP data will be discussed. First I will give a description of the experiment and subsequently an introduction to the resolution function of a TAS. Finally the procedures and assumptions used in the fitting procedure will be explained.

8.1 The hemo-ilmenite experiment on TASP

A polarised neutron diffraction experiment on the hemo-ilmenite sample was carried out in august 2005 by Luise Theil Kuhn, Richard Harrison, Kim Lefmann and Bertrand Roessli at the TASP instrument (see 7.2) in the Paul Scherrer Institute, Switzerland. My part of the work is the analysis of the data from the original experiment and is based on the original datafiles and the experimental log from the experiment.

The experiment was performed with a neutron energy of $E = 5.00$ meV ($k = 1.535\text{Å}^{-1}$, $\lambda = 4.05$ Å) in order to optimize the polarisation without loosing to much intensity. The instrument was equipped with PG(002) monochromator and analyser and with polarising benders. The divergence of the benders is about 80', so the collimation in the experiment was not good. To keep the polarisation of the neutrons vertical at the sample position large diameter solenoid coils (Helmholtz coils) generated a small vertical magnetic field (0.05 T) at the sample position. One spin flipper was used in order to distinguish SF and NSF processes. All scans were 2000 or 4000 monitor counts pr. point (corresponding to average counting times of about 11 s and 22 s pr. point) and the displayed results will be normalized to the monitor counts (cnts/mon).

8.1.1 Sample environment

The sample, which was glued to an aluminum holder, was placed in a cryostat inside the field of a superconducting magnet. The range of magnetic fields in the experiment was 0.05 T - 2.0 T. The temperature range in the experiment was 4 K - 290 K. The experiment started with the 4 K measurements followed by measurements at 100 K, 200 K and 290 K. During the experiment there were problems with the temperature control meaning that the temperature in the experiment was not well defined. The uncertainty in the temperature was maximally 2 K and for most scans much smaller, but some measurements were performed at different temperatures than stated in the log (some of the 100 K scans were really at 90 K and some of the 290 K scans were really at 275 K). This is however not important since no measurements were performed close to any phase transitions.

In the early stages of the experiment there was an incident where the field of the superconducting magnet dragged a part of the polarisation guide away from its position. The polarisation guide was returned to its position and the experiment was continued with the magnetic field kept under 2 T to avoid a repetition of the accident. The polarisation guide may not have been placed in exactly the same way as before and there is a chance that the flipping ratio after the incident was not exactly the same as before. Only a very few scans were performed before the incident and may thus have been under slightly different conditions than in the main part of the experiment.

8.1.2 Experimental geometry

The geometrical parameters that are important for the interpretation of the measurements are the direction of the applied field, the neutron polarisation and the crystallographic axes of the sample. The geometry in the experiment is explained in figure 8.1

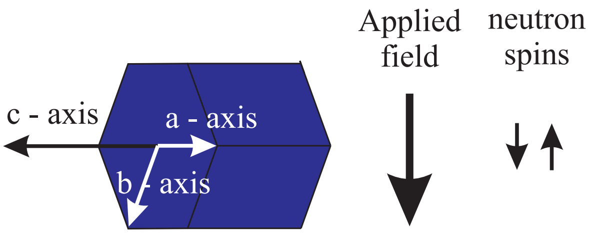

Figure 8.1: ***Experimental geometry:*** *The applied field and the neutron polarisation are both vertical. The crystallographic c-axis is horizontal. All (h0l) reflections can now be measured by rotating the sample around a vertical axis. The a-c plane will be horizontal and thus perpendicular to the neutron polarisation (and the field) at all times.*

8.1.3 Hemo-ilmenite reflections

In hemo-ilmenite there is several Bragg reflections from both hematite and ilmenite that can be measured with neutrons. The reflections that were measured in the TASP experiment are listed in table 8.1. Both structural and magnetic reflections were measured to study both the crystal- and magnetic structure of the sample.
According to the experimental log the measured reflections are the ones listed in table 8.1. It seems very likely that during the alignment of the crystal the $(00\bar{3})$ peak was mistaken for the (003) peak, and consequently the units of the reciprocal lattice have during the experiment have been $(hk\bar{l})$ instead of (hkl). This mistake will be corrected in the rest of the thesis. In addition, the data analysis revealed that the structural ilmenite (101) and $(10\bar{2})$ reflections are close to the hematite reflections we set out to measure. The structure factors of ilmenite and hematite were calculated by Bente Lebech and are quoted in appendix A.

The structural reflections should give rise to NSF scattering only, whereas the magnetic reflections can in general give rise to both NSF and SF scattering. The experimental geometry and the direction of the spins in the sample determine the ratio of the NSF to the SF signal. An applied field can change the spin directions in the sample and thus change the intensity of magnetic reflections, while a magnetic field should have no effect on the structural reflections.

(hkl)-log	(hkl)-corrected	hem/ilm	s/m	q [Å^{-1}]
(003)	$(00\bar{3})$	ilm	s	1.34
(003)	$(00\bar{3})$	hem	m	1.37
$(10\frac{1}{2})$	$\left(10\frac{\bar{1}}{2}\right)$	ilm	m	1.44
(102)	$(10\bar{2})$	hem	s	1.70
$(10\bar{1})$	(101)	hem	m	1.51

Table 8.1: ***Hemo-ilmenite reflections:*** *List of the ilmenite (ilm) and hematite (hem) reflections measured in the TASP experiment according to the experimental log. The peaks are either structural peaks (s) or antiferromagnetic peaks (m). It seems that the index l should be replaced with -l (because some of the measured reflections are actually forbidden, while the reflections with the replacement of l with -l is a strong reflection) and this will be done throughout the rest of the thesis.*

Structural $(10\bar{2})$ hematite and $(00\bar{3})$ ilmenite reflections: The structural hematite reflection should give rise to only NSF scattering and the plan was to use this reflection to determine the FR. However, there might be a small SF signal because of canting in the hematite, which would produce a ferromagnetic component. This can make it more difficult to obtain a value for the FR. The same is true for the $(00\bar{3})$ ilmenite reflection, but ilmenite is not known to be prone to canting in the same way as hematite. The ilmenite $(00\bar{3})$ reflection is very close to the magnetic hematite $(00\bar{3})$ reflection in q-space and this may complicate the data analysis.

Magnetic $\left(10\frac{\bar{1}}{2}\right)$ ilmenite reflection: The antiferromagnetic ilmenite $\left(10\frac{\bar{1}}{2}\right)$ reflection is expected to show up only for temperatures below the Néel temperature of ilmenite ($T_N \approx 55K$) and should be predominantly SF scattering since the AFM sublattice directions in ilmenite is along the c - axis, which is perpendicular to the neutron polarisation. If the ilmenite spins are canted a small NSF signal might turn up.

Magnetic $(10\bar{1})$ **and $(00\bar{3})$ hematite reflections**: The two magnetic hematite reflections are expected to be present at all temperatures in the experiment. The ratio of the NSF/SF signals will give information about the directions of the hematite spins. We might see a change in the intensities as a function of temperature if lamellae of different sizes undergo Morin transition at different temperatures.

8.2 The resolution function

In an experiment on a TAS the measured quantity is not simply the (differential) scattering cross section, but the convolution of the scattering cross section with the resolution of the spectrometer. In expressions like (4.7) it is assumed that neutrons with some fixed k_i and k_f are measured, but in an experiment there will always be some spatial divergence and some final distribution of energies of the neutrons. To get a sufficient flux on the sample it is necessary to work with a limited collimation and to use mosaic crystals for monochromator and analyser. The distribution of energies and momenta around some values, ω_0 and q_0 can be described by the spectrometer's resolution function, of which I will give a short description here. A much more thorough description can be found in chapter 4 of ref. [30] on which my presentation of the subject is based.

The resolution function is conveniently described as a function of $\Delta\mathrm{E}$, $\Delta\mathrm{q}_{||}$, $\Delta\mathrm{q}_{\perp}$ and $\Delta\mathrm{q}_z$, where $\Delta\mathrm{E}$ is the energy distribution, $\Delta\mathrm{q}_{||}$ is the momentum distribution in the direction of the scattering vector (q_0), $\Delta\mathrm{q}_{\perp}$ is the momentum distribution perpendicular to the scattering vector, but in the scattering plane (horizontal), and Δq_z is the vertical momentum distribution. It is often assumed that Δq_z is decoupled from the other parameters and this is especially valid for elastic measurements. If we ignore the vertical resolution the resolution function can be described as an ellipsoid in $(\Delta E, \Delta q_{||}, \Delta q_{\perp})$ space. Often, the mosaicity distribution of the monochromator and analyser as well as the transmission of the collimators are assumed to be Gaussian and the resolution function of the spectrometer is then assumed to be a 4d-Gaussian.

There are two main reasons why one wants to know the resolution function of a spectrometer. One is to optimize the experiment by scanning in directions where the resolution is good. The other is to be able to understand the data from an experiment better. If the resolution function is known, one can distinguish between features in a measured signal that come from the sample and features that come from the instrumental resolution. If the resolution function is Gaussian then the measured signal from a Bragg reflection will also be a Gaussian, unless there are features in the sample that obscure the shape. The shape of the signal could be changed by finite size broadening or by contamination from other reflections than the one under investigation, or by inelastic signals. Let us for now assume the signal to be Gaussian and the scan to be longitudinal (along q). The measured signal will then be a Gaussian with center $C = q_0$, amplitude A, determined by the scattering cross section and some width W (see appendix B). If the width is equal to the instrumental resolution $W = \Delta q_{||}$ the peak is said to be resolution limited. If the crystal is small (nano sized) then the unit cell sum for scattering vectors close to the diffraction condition will not average to zero as for a crystal of infinite size. This means that the peak can be broadened according to the Scherrer formula (See e.g. section 13.1 in ref. [36]):

$$B(2\theta) = \frac{K\lambda}{Lcos(\theta)}, \tag{8.1}$$

where $B(2\theta)$ is the broadening due to an average crystal size of L in the direction of $\mathbf{q}$. The constant K depends on the shape of the system and is close to 1. I will use the value K =0.94, which is for a spherical scatterer (for a cube $K = 1.00$). If the observed resolution (width) is W_{obs} and the instrumental resolution (width) is $W_{\text{instr}} = \Delta q_{||}$, the broadening is (assuming Gaussian broadening)

$$W_{\text{instr}}^2 + B^2 = W_{obs}^2. \tag{8.2}$$

In our sample we have an unknown distribution of lamella sizes. Lamellae of different sizes might have different strain and different anisotropy constants and may therefore respond differently to for example an applied field. The strain in the lamellae will also cause a broadening of the signal, but this will not be investigated in this experiment. In our sample we have a distribution of hematite lameallae with sizes down to about 1-2 nm and we can therefore expect the hematite peaks to be finite-size broadened. The ilmenite is believed to behave much more like a bulk system and we shall expect no broadening in the ilmenite peaks.

8.2.1 Computing the resolution function

I attempted calculating the resolution function of TASP using the MATLAB programme Rescal available at the ILL homepage [37]. Rescal is known to reproduce the experimental resolution to within 2 standard deviations. This was confirmed by an unpublished comparison of Rescal and other programmes with experimental data carried out at ILL [38]. The results should thus not be considered as an accurate result, but rather as a good starting point for the data analysis.

In Rescal I computed the resolution using 'Popovici's' method, which besides collimation and mosaicity takes the size of the optical elements as well as focusing effects into account. The instrumental parameters needed for the calculations were supplied by Bertrand Roessli and are tabulated in appendix C. The resolution of TASP is assumed to be Gaussian, and since all the scans in the experiment were longitudinal (along $\mathbf{q}$) the only resolution parameter I need for the data analysis is $\Delta q_{||}$ which will then be the width of the measured peaks if they are resolution limited. It turns out that the measured widths were considerably smaller than the widths from Rescal. The width can not be smaller than the instrumental resolution and the values from Rescal must therefore be wrong. Attempts to calculate the resolution with the Restrax programme gave similar results and it therefore it seems likely that the instrumental parameters used for the calculations are wrong. In the data analysis the calculated widths will be useless and we will have to treat the widths as free parameters in the fitting procedure. The calculated resolutions for the measured reflections (see table 8.1) are presented in table 8.2.

8.3 Sample monocrystalinity

From the initial attempts to fit the data we suspected that the sample might not be a single crystal. We therefore performed a short experiment on the MORPHEUS spectrometer. With much better collimation than in the TASP experiment we mapped out the $(00\bar{3})$ peak to try and resolve the signal from the supposed different crystals.

The result of the MORPHEUS experiment is the colour plot displayed in figure 8.2. The ilmenite peak and the hematite peak is easily distinguishable with the brighter one being the ilmenite peak. If you look at the data more

(hkl)	$\Delta q_{\|\|}\left[10^{-2}\text{Å}^{-1}\right]$	$\Delta q_{\|\|}\,[10^{-2}\text{r.l.u.}]$	$\Delta q_l[10^{-2}\text{r.l.u.}]$
$(00\bar{3})$	1.971	4.32	4.32
$(10\frac{1}{2})$	1.906	1.480	6.62
$(10\bar{2})$	1.709	2.25	2.01
$(10\bar{1})$	1.866	1.748	1.236

Table 8.2: ***Calculated resolution parameters.*** *$\Delta q_{||}$ is the resolution along the scattering vector. It is given in units of $\mathring{A}^{-1}$, which is the value obtained directly from Rescal and converted to [r.l.u.], which will be the unit I use in the data analysis. All scans in the experiment are longitudinal, but I will in general plot the scattering as a function of q_l and therefore the projection of $\Delta q_{||}$ on q_l is needed and is therefore given in the final column. Except for the $(00\bar{3})$ the experimental widths were found to be significantly smaller than the calculated widths and the calculated widths must therefore be wrong.*

carefully you can see a ‘shoulder’ on both peaks. This can be explained by the sample consisting of two crystals that are tilted slightly (0.6°) with respect to each other. Unfortunately, the alignment of the crystallographic a- and b-axes in the experiment was not known and it is therefore not possible to determine the relative orientation of the two crystals. However, as the difference in scattering vector between the ilmenite and hematite peaks is in the q_l direction it can be seen by the figure that the tilting of the two crystals relative to each other is close to perpendicular to the q_l axis, which is a line between the top points of the two peaks.

The conclusion from the MORPHEUS experiment is that there are two crystals in the sample. One is tilted about 0.6° relative to the other. During the data analysis we shall keep in mind that the sample is not a single crystal and although the crystals are close to each other we might see double peaks in the data. Here it is important to note that the sample is a natural piece of rock which can not be expected to be a perfect crystal and the mosaicity of the crystals may be almost the same size as the splitting of the two crystals. Naturally the splitting of the crystal might be visible in some scan directions only.

8.4 Determination of flipping ratio

In the analysis of the TASP data the fits will be nonlinear least squares fits, performed with the MATLAB programme MFIT available on the homepage

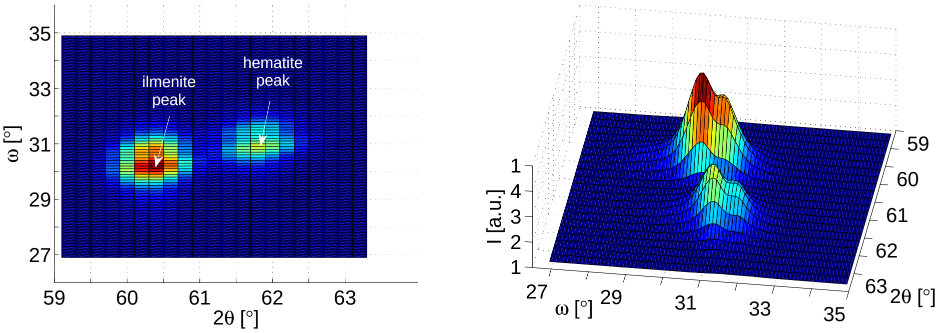

Figure 8.2: ***Map of the (00$\bar{3}$) peaks.*** *ω is the sample rotation angle and 2θ is the detector angle.* ***Left:*** *Top view of the (00$\bar{3}$) peaks. The positions of the ilmenite and hematite peaks are marked, and the line connecting them is the q_l direction.* ***Right:*** *Surface plot of the (00$\bar{3}$) peaks. The 'shoulders' on the peaks indicate that there are two crystals in the sample at an angle of about $0.6°$ relative to each other.*

of the Institute Laue Langevin [37]. All amplitudes are normalized to the number of monitor counts (cnts/mon) per point in the scan.

The FR is determined as the ratio of the NSF and SF intensities of a purely structural peak. As the peak is entirely structural there would be no SF signal if the polarisation was perfect. The FR is calculated as

$$FR = \frac{I^{NSF}}{I^{SF}} = \frac{A^{NSF} \cdot W^{NSF}}{A^{SF} \cdot W^{SF}}. \tag{8.3}$$

Where the A^{NSF} and A^{SF} are the amplitudes and W^{NSF} and W^{SF} the widths of the Gaussian fit to the raw NSF and SF data. The FR might depend on the applied field and should therefore be calculated for a range of fields.

8.4.1 FR from the (10$\bar{2}$) peak.

The structural (10$\bar{2}$) hematite peak was measured in order to be able to determine the experimental FR. As an example the FR is calculated from the (10$\bar{2}$) peak at a magnetic field of B = 2.0 T and a temperature of T = 4 K. The raw data with a Gaussian fit is shown in the left part of figure 8.3. Here is should be noted that the fit is to a single Gaussian. At a later point in the analysis it was realized that the peak is really a double peak because the ilmenite (10$\bar{2}$) peak is close to the structural (10$\bar{2}$) hematite peak. This is however not a problem for the data analysis because the (integrated) intensities are well represented by fit to a single (broader) Gaussian and because the error would be the same in the SF and NSF signal. A significant

SF intensity is clearly present. The FR is calculated from (8.3) and is found in this particular scan to be:

$$FR = \frac{1.3056 \cdot 0.02514}{0.344 \cdot 0.0245} = 3.89 \tag{8.4}$$

and the corresponding polarisation is $p = \frac{FR-1}{FR+1} = 0.591$. Inserting this in (5.25) gives the correctional matrix :

$$\mathbf{P}^{-1} = \left(\frac{1}{2} \begin{pmatrix} 1.591 & 0.409 \\ 0.409 & 1.591 \end{pmatrix} \right)^{-1} = \begin{pmatrix} 1.346 & -0.346 \\ -0.346 & 1.346 \end{pmatrix}. \tag{8.5}$$

When $\mathbf{P}^{-1}$ is multiplied to the data we get the corrected spectrum, which is shown to the right in figure 8.3. When the FR was calculated from the $(10\bar{2})$ intensity it for different fields it showed variations from FR around 5 at the lowest fields (B = 0.05 T) to FR around 4 for B = 2 T like in the example. This corresponds to polarisations in the range around 0.60 - 0.67. When the FR values obtained from the $(10\bar{2})$ peak was used to correct data from other reflections it became apparent that there was a problem: The correction introduces data points with negative counts as seen in figure 8.4. This is of course unphysical and have to be rejected. In order to get rid of the unphysical data the FR has to be larger than the values obtained from the $(10\bar{2})$ peak.

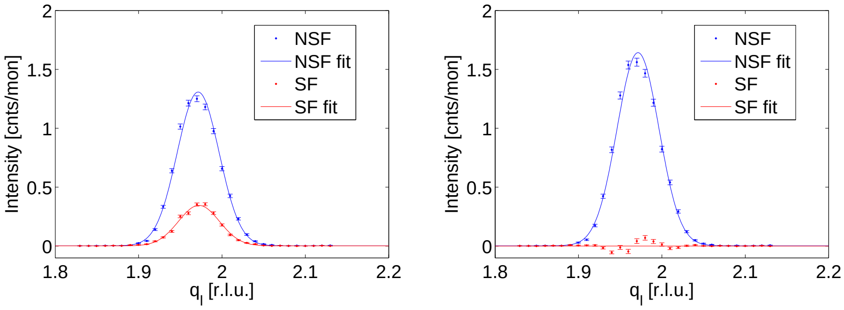

Figure 8.3: ***Polarization correction.*** *Intensity of $(10\bar{2})$ peak at a magnetic field of $B = 2.0$ T and a temperature of $T = 4$ K.* ***Left:*** *Uncorrected intensity.* ***Right:*** *Intensity corrected with $FR = 3.89$. When the peak is corrected all the intensity is NSF as it should be for a purely structural peak.*

We can conclude that our assumption of pure NSF scattering from the $(10\bar{2})$ peak was false and that there in fact is a magnetic signal in the supposed structural $(10\bar{2})$ peak. This is interesting and I will get back to that in section 9.3. For now we will have to think of another way of determining the FR.

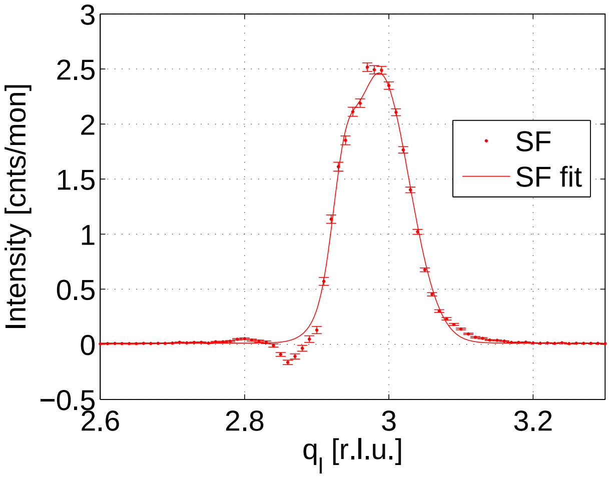

Figure 8.4: ***Unphysical data*** *Intensity of the* $(00\bar{3})$ *peak at a magnetic field of* $B = 2.0$ *T and a temperature of* $T = 290$ *K. The data is corrected with* $FR = 3.89$ *corresponding to the calculated value at the given field (see fig. 8.3). The correction have introduced unphysical data points as some of the points are significantly below zero.*

The magnetic signal in the $(10\bar{2})$ peak might have to do with canting in the hematite and there might be some effects of the finite size of the smaller lamellae giving unusual magnetic properties. The ilmenite is believed to behave as bulk ilmenite and if we measure an ilmenite peak at a temperature where the ilmenite is paramagnetic we will not see a magnetic contribution from canting. We have measured the ilmenite (101) and $(00\bar{3})$ peaks and either one could in principle be used. The $(00\bar{3})$ peak scatters about 3 times as strongly as the (101) peak and is chosen as our best candidate as a structural ilmenite peak that can be separated from the close-lying hematite peak in order to get the FR.

The FR can be found from scans of the $(00\bar{3})$ peak by requiring that the structural ilmenite peak is NSF only and fitting the corrected SF peak to a hematite peak only and do this for a range of values of the FR. The value that gives the best fit will then be the one to use for the correction. The quality of the fits will be evaluated from the reduced χ^2:

$$\tilde{\chi}^2 = \frac{\chi^2}{\nu}, \tag{8.6}$$

where $\nu = N - n - 1$ is the number of data points (N) minus the number of fitted variables (n) minus one. The value of $\tilde{\chi}^2$ should be as close to 1 as possible.

The procedure of determining the FR from the $(00\bar{3})$ peak is complicated because it is a combination of the magnetic $(00\bar{3})$ hematite peak and the structural $(00\bar{3})$ ilmenite peak (the situation would be similar if the (101) reflection were used). The two $(00\bar{3})$ reflections have respective scattering vectors of $q_{ilm} = 1.34\text{Å}^{-1}$ and $q_{hem} = 1.37\text{Å}^{-1}$ and this means that they are difficult to resolve with the experimental resolution in the TASP experiment (0.02 Å^{-1}). Before we can fit the $(00\bar{3})$ signal properly we have to take into account that the sample is not monocrystallinic and we therefore might have to double the number of Gaussians in the fit. I will go through the fitting procedure for the $(00\bar{3})$ peak in some detail in the following section. As the $(10\bar{2})$ and (101) peaks are also double peaks the following can in addition serve as a general example of how the fitting procedure goes.

Fitting the $(00\bar{3})$ peaks

As a start model we use 4 NSF Gaussians and 2 SF Gaussians in order to account for both the hematite and ilmenite peaks as well as the two crystals in the sample (see fig. 8.2). Before any assumptions about the fitting parameters are made the parameters of the 4 NSF Gaussians could be as displayed in table 8.3. A common background is added to the sum of the four Gaussians, giving 13 free parameters.

Fortunately we can make some assumptions about the fitting parameters and get some constraints on these. The ratio between the intensities of the scattering from the two parts of the crystal are assumed to be the same for hematite and ilmenite and we can thus introduce a new variable γ:

Amplitudes	A_{h1}	A_{h2}	A_{i1}	A_{i2}
Centers	C_{h1}	C_{h2}	C_{i1}	C_{i2}
Widths	W_{h1}	W_{h2}	W_{i1}	W_{i2}
Background	BG			

Table 8.3: ***Fitparameters for 4 Gaussians.*** *Subscripts h and i denotes parameters for the hematite and ilmenite peaks respectively.*

$$\frac{A_{h1}}{A_{h2}} = \frac{A_{i1}}{A_{i2}} = \gamma \tag{8.7}$$

We also assume that the distance in q-space between the two hematite peaks is the same as the distance between the two ilmenite peaks. This assumption again makes it sensible to introduce a new variable δ:

$$C_{h1} - C_{h2} = C_{i1} - C_{i2} = \delta \tag{8.8}$$

Amplitudes	A_h	A_i	
Centers	C_h	C_i	
Widths	W_h	W_i	
Common	γ	δ	BG

Table 8.4: ***Fitting parameters for 4 Gaussians with constraints.*** *Subscripts h and i denotes parameters for the hematite and ilmenite peaks respectively. These parameters will be the fit parameters for the NSF fit. The SF fit will have only the hematite parameters and the common parameters γ, δ and the background BG.*

The values of γ can be estimated from fig. 8.2 to approximately 0.7 and the size of δ can be given an upper limit by noting that it is significantly smaller than the distance between the hematite and ilmenite peaks ($q_i - q_h$ = 0.03 Å^{-1} ≈ 0.05r.l.u.). The next assumption is that the width of the two hematite Gaussians should be the same, as should the width of the two ilmenite Gaussians. The widths comes from the instrumental resolution and possibly from some broadening effect which is assumed to be the same for the two crystal pieces. We can now reduce the number of variables in the NSF fit from 13 to 9 and get the parameters in table 8.4. In the SF fit will be the 3 hematite parameters and the 3 common parameters only.

Finally we note that the experimental resolution as well as the sample geometry is the same in a NSF as in a SF experiment. This means that the widths and centers of the hematite peaks should be the same in the SF as in the NSF signal. The fitting can now start with the SF data, from which we can get the positions and widths of the hematite peaks. When the NSF data is fitted the hematite widths and centers will no longer be free variables and the ilmenite positions and widths can be determined. Before we can find FR we should determine the values of γ and δ in order to avoid changing too many parameters at a time. It turns out that if δ is a free variable in the fit it will converge to a value larger than the difference in the positions of ilmenite and hematite, which is not consistent with the splitting of the two crystals. The fit is in stead performed with δ as a constant and repeated for a range of δ values. The value of $\tilde{\chi}^2$ can then be evaluated as a function of δ in order to find out if there is a local minimum for a smaller δ-value. An example of a fit with $\delta = 0.015\,$r.l.u. is given in fig 8.5. In figure 8.7 $\tilde{\chi}^2$ is plotted against δ for a constant $FR = 6$.

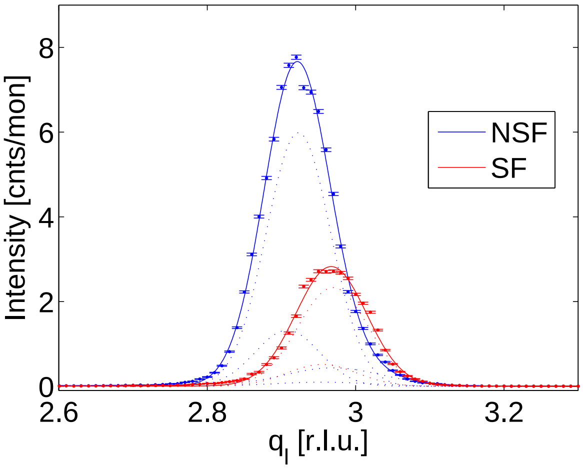

Figure 8.5: ***Fitting the (00$\bar{3}$) peak with 4 NSF and 2 SF Gaussians.*** *The data is taken at T = 100 K and B = 2 T. The dotted lines are the 4 NSF Gaussians (blue) and the 2 SF Gaussians (red). The solid blue (red) line is the sum of the NSF (SF) Gaussians. A constant $\delta = 0.015 r.l.u.$ was used. The quality of the fits is given by $\tilde{\chi}^2_{NSF} = 27.4$ and $\tilde{\chi}^2_{SF} = 20.0$.*

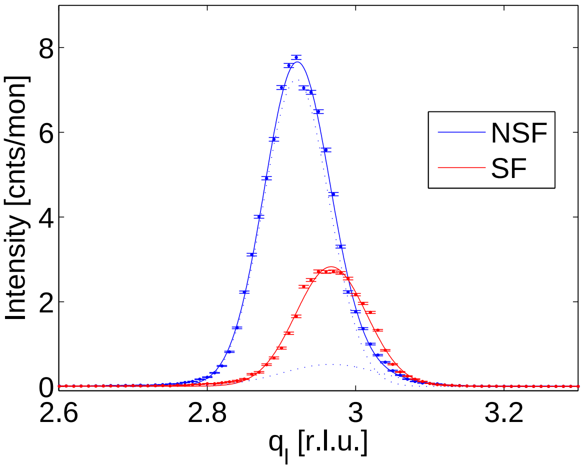

Figure 8.6: ***Fitting the (00$\bar{3}$) peak with 2 NSF and 1 SF Gaussian.*** *The data is taken at T = 100 K and B = 2 T. The dotted lines are the 2 NSF Gaussians and the solid blue line is their sum. The quality of the fits is given by $\tilde{\chi}^2_{NSF} = 27.6$ and $\tilde{\chi}^2_{SF} = 19.7$.*

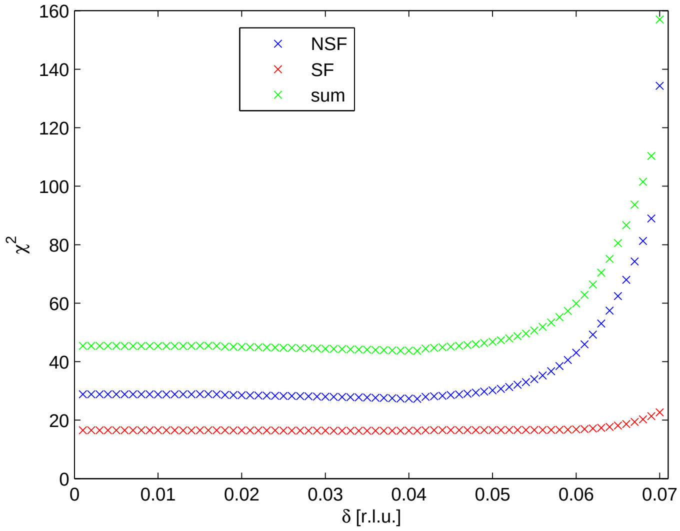

Figure 8.7: $\tilde{\chi}^2$ ***vs*** δ*: The quality of the SF fit represented by the value of* $\tilde{\chi}^2$ *is constant for* $\delta \leq 0.06$*. The* $\tilde{\chi}^2$ *of the NSF fit is constant for* $\delta < 0.04$*. This data is from the same scan as in figs. 8.5 and 8.6, but the same trend apply for all scans.*

There is no difference in the quality of the fit between a small nonzero δ value and zero and this indicates that the spitting of the two crystals can not be seen in the $(00\bar{3})$ peak with the present resolution. From now on the $(00\bar{3})$ peak will therefore be fitted with 1 SF Gaussian and 2 NSF Gaussians (same procedure as described above with constant $\gamma = \delta = 0$). The same scan as in fig. 8.5 is fitted in this way in fig. 8.6. The results for the other measured reflections are similar and the dual-crystallinity of the sample is thus not visible in the TASP data. In general, the $(00\bar{3})$ peak has a flat-top-shape and does not seem to be perfectly well fitted with a Gaussian. There must be some other explanation for the odd shape of the $(00\bar{3})$ SF peak as well as the asymmetry of the other SF peaks. This will not be included in the fitting and this might introduce a systematic error in the data analysis.

8.4.2 Determining the FR from the $(00\bar{3})$ peaks

Now all that is left is to perform the fitting routine described above for a range of values of the FR. The value of the FR that gives the smallest $\tilde{\chi}^2$ for the SF fit will be chosen. Unfortunately the FR values obtained in this way gives unphysical data, when used in the polarisation-correction. On closer inspection, some points in the SF peak, at the low-q side of the peak deviate systematically from the Gaussian shape. This might introduce a systematic error that gives a lower $\tilde{\chi}^2$ for an unphysical FR than for the true value. In some scans the systematic deviation from the Gaussian shape extended from about $q_l = 2.75$ r.l.u. to about $q_l = 2.85$ r.l.u. and in other scans it extended all the way out to 2.6 r.l.u. (See fig. 8.8.) It was therefore attempted to find the FR from the $(00\bar{3})$ SF scans with the anomalous part cut out of the data.

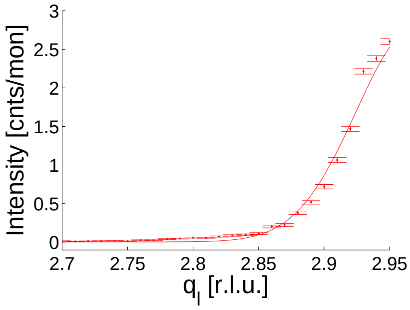

Figure 8.8: ***Deviations from the Gaussian shape:*** *In the left side of the SF peak the data points are systematically above the Gaussian fit. This might be the explanation for the to low value of the FR.*

The values of the flipping ratio found with different methods are plotted in fig. 8.9. We assume that a field effect on p would scale as B^2 since it must be an even function, hence the field-dependence of FR will be $FR = FR_0(1 + \alpha B^2)$ (Simply expand the expression for FR as a function of p.) There are only 2 points at 1 T and they seem to be a bit off. Therefore we take the average of the blue and green points on 0.05 T and 2 T respectively and fit a parabola with top point in B = 0. This is just a procedure to obtain a value for the FR that can be used in the analysis. I believe the procedure to be better than using a constant FR. The resulting expression is.

$$FR(B) = -0.37B^2 + 6.61 \tag{8.9}$$

Now the FR to be used in the analysis will be as in table 8.5. The large variation in the values of FR in figure 8.9 shows that the polarisation in the experiment was not well controlled and some degree of systematic error is believed to be introduced in the data during the FR correction.

B [T]	0.05	0.25	0.50	0.75	1.0	1.2	1.4	1.6	1.8	2.0
FR	6.61	6.59	6.52	6.40	6.24	6.08	5.88	5.66	5.41	5.13

Table 8.5: ***Flipping ratio versus magnetic field.*** *These FR values, calculated from (8.9) will be used in the data analysis.*

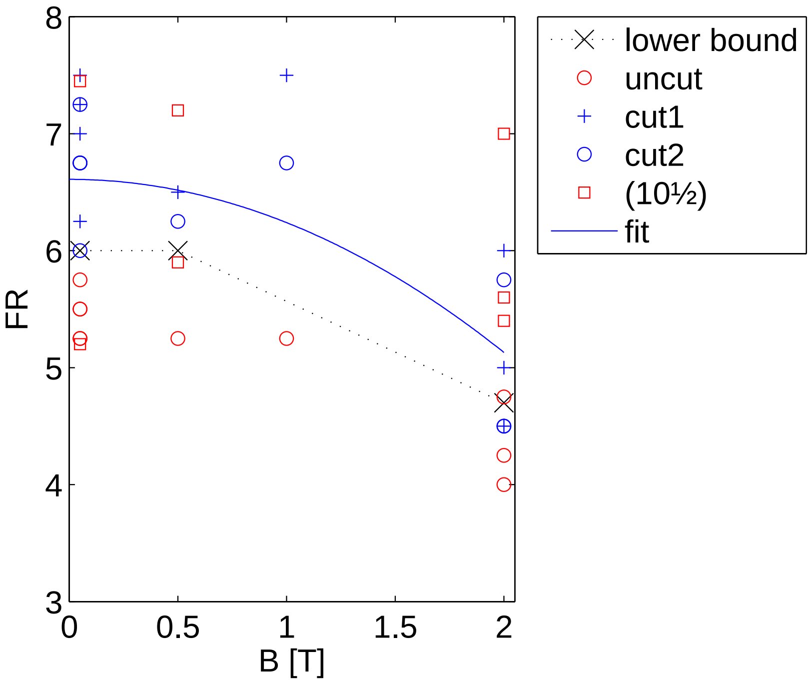

Figure 8.9: ***FR as a function of applied field****: The 'lower bound' values are the lowest values of the FR that does not give obviously unphysical results (negative counts) and are obtained from fits of the $\left(10\frac{\bar{1}}{2}\right)$ peak. The red circles are the FR values obtained from the fit to the uncut $(00\bar{3})$ SF data and are generally below the lower bound and therefore disregarded. The blue points are the FR values obtained by fitting to the $(00\bar{3})$ SF data with the anomalous points omitted. In cut1 points in the range $q_l = 2.75 - 2.85$ r.l.u. are omitted, while all values below $q_l = 2.85$ r.l.u. are omitted in cut2. The $\left(10\frac{\bar{1}}{2}\right)$ points are obtained by requiring that the supposed second order structural peak in the data (see section 9.4) should have the same intensity in all fields. The uncertainty on these points are however so large that they are not believed to give information of much value. The solid blue line is a fit to average of the blue points at $B = 0.05$ T and $B = 2$ T. The points at 0.5 T and 1 T are not used in the fit because there are too few points and the 1 T points would probably give an overestimate of the FR*

Chapter 9

TASP - Results

In this chapter I will present the results of the TASP experiment. Before presenting the results from measurements of the different reflections I will give some general comments:

Like the $(00\bar{3})$ peak, the (101) and $(10\bar{2})$ peaks are double peaks, with an ilmenite peak at slightly lower q than the hematite peak. The (101) hematite peak is magnetic, and although the $(10\bar{2})$ hematite peak is structural there is a magnetic contribution to the signal as we have seen in section 8.4.1. We can therefore start the fitting with the SF peak and the fitting procedure described for the $(00\bar{3})$ peak in section 8.4.1 will therefore also apply to these peaks. The magnetic $\left(10\frac{\bar{1}}{2}\right)$ ilmenite peak is fitted with a single Gaussian.

Peak widths:
The widths of the measured peaks should not depend on temperature or applied field. However, the fitted widths do show some dependence of field. This must be because of systematic errors and will not be investigated further. For each reflection the average width will be found from the fit and the fitting routine will be repeated with the width of the Gaussian constrained to the average value.

Peak positions:
The positions of the peaks should not depend on field, but might change with temperature because of thermal expansion of the crystal. The variation in the peak positions in our experiment is around 0.2% and is roughly the same in all scan directions. The peaks do not generally move towards lower q for higher temperatures as would be the case if the crystal expanded. If the positions did move with thermal expansion the change should be largest in the $(00\bar{3})$ scans because the length of the c-axis is expected to change more than the other shorter directions. (A change in c of about 1% and in a (or b) of about 0.01% on changing the temperature from 24° C to 1050° C has

been reported in ref. [39].) The peak positions will not be examined further and will be considered constant.

9.1 Results for the $(00\bar{3})$ peaks

Examples of fits to the $(00\bar{3})$ scans are given in fig. 9.1. In general the SF peak seems stretched and quite flat on the top and the fits to a Gaussian is therefore not good. Upon very close inspection there is an anomalous feature on the left side of the peak where the fit is not very close to the data points (see fig. 8.8). The NSF peak fits reasonably well to a sum of a (hematite) peak with same width and position as in SF and an (ilmenite) peak with position and width as free parameters.

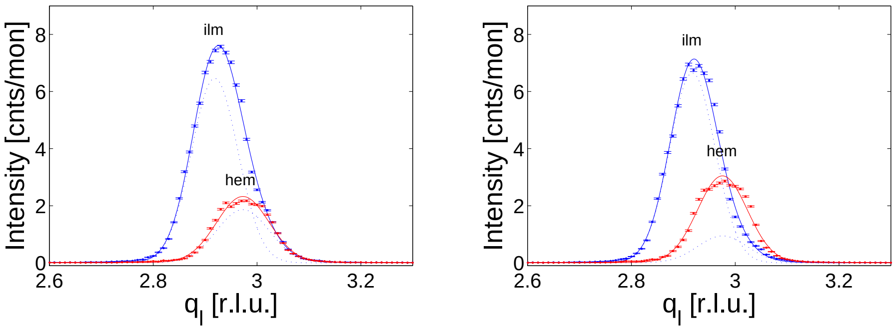

Figure 9.1: ***Scans of the*** $(00\bar{3})$ ***peak at T = 100 K: Left:*** *Intensity at B = 0.05 T and corrected with FR = 6.6.* ***Right:*** *B = 2 T and corrected with FR = 5.1. The red line is the SF fit. The dotted blue lines are the two NSF Gaussians and the solid blue line is their sum. The quality of the fits are represented by* $\tilde{\chi}^2_{NSF} = 27$ *and* $\tilde{\chi}^2_{NSF} = 34$ *for the NSF fits and* $\tilde{\chi}^2_{SF} = 17$ *and* $\tilde{\chi}^2_{SF} = 22$.

The fitted widths depend slightly on the applied field, which is believed to be because of systematic errors. The average widths for the hematite $\langle W_{\text{hem}} \rangle$ and ilmenite $\langle W_{\text{ilm}} \rangle$ peaks are found as

$$\langle W_{\text{hem}} \rangle = 0.049 \pm 0.002\,\text{r.l.u.},$$
$$\langle W_{\text{ilm}} \rangle = 0.0434 \pm 0.0009\,\text{r.l.u.}$$

Which corresponds to an average broadening of the hematite of (assuming $W_{\text{instr}} = W_{\text{ilm}}$)

$$B = \sqrt{\langle W_{\text{hem}} \rangle^2 - \langle W_{\text{ilm}} \rangle^2} = 0.022\,\text{r.l.u.} = 0.030\,\text{Å}^{-1} = 0.0097\,\text{rad}.$$

From the Scherrer formula (8.1) this can be translated to an average particle size of $L = 44$ nm along the c-direction.

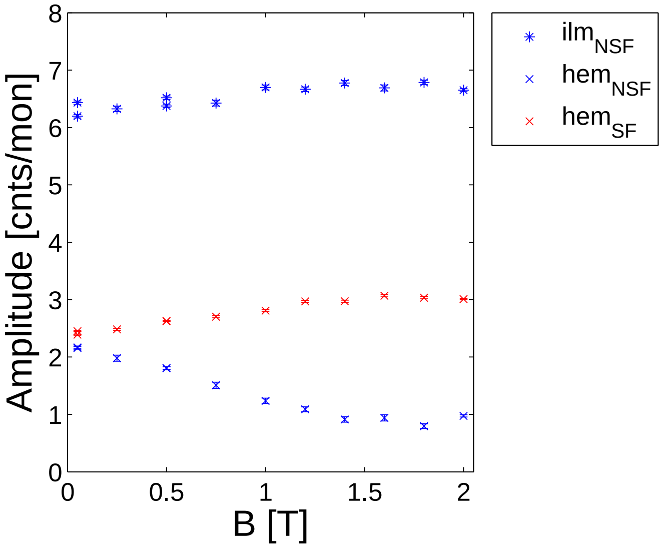

Figure 9.2: ***Amplitudes of the*** $(00\bar{3})$ ***peaks at*** T ***= 200 K.*** *The amplitude of the ilmenite peak increases slightly with field. The magnetic hematite signal has a SF amplitude that increases with the applied field, whereas the NSF decreases. This indicates that the hematite spins are turning away from the field. Note that the ilmenite and hematite signals cannot be compared directly since their widths are different. The trends are similar for all temperatures.*

The fitted amplitudes are displayed in fig. 9.2 for $T = 200$ K and show a systematic dependence on field. The amplitude of the ilmenite peak has some field dependence, which is unexpected. In the hematite peak the SF signal increases with field and the NSF signal decreases, indicating that the magnetic moments become more perpendicular to the applied field. Scans at all temperatures (4 K - 290 K) show similar trends, but slightly different overall SF and NSF amplitudes. The fitted amplitudes of the hematite peaks for all temperatures are displayed in figure 9.3. The trends are the same as in fig. 9.2, except that the amlitudes shift systematicly with temperature. Two of the scans have amplitudes that deviate significantly from amplitudes of scans at similar fields and temperatures. The deviation of these scans (with $B = 0.05$ T, $T = 290$ K and $B = 2$ T, $T = 4$ K respectively) is likely due to some problem in the experiment, rather than a real physical effect from the sample.

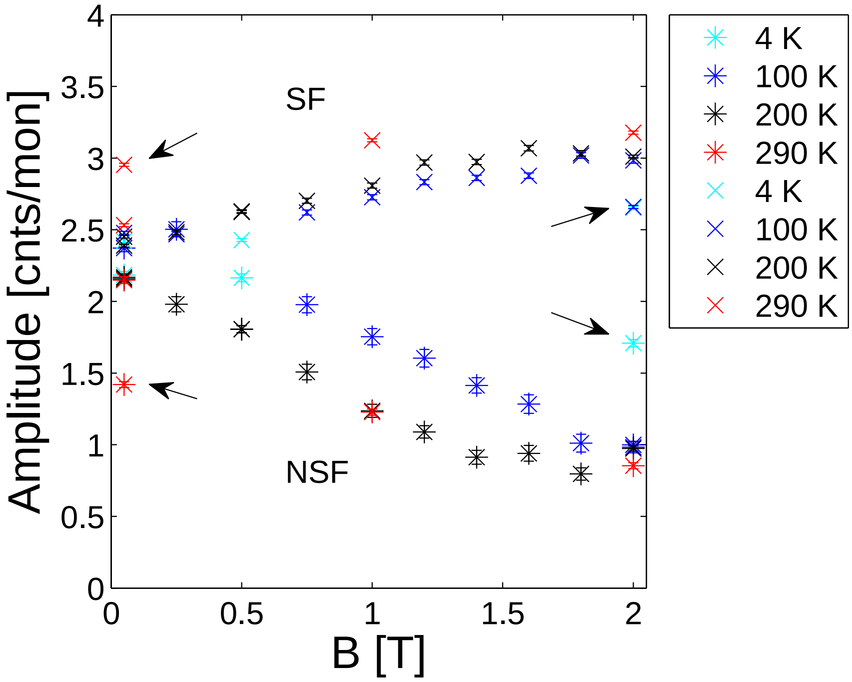

Figure 9.3: ***Amplitudes of the*** $(00\bar{3})$ ***heamtite SF and NSF peaks.*** *The SF amplitude increases and the NSF amplitude decreases with field, indicating that the spins are turning away from the field. Two points (arrows) in both the SF and NSF data deviate significantly from scans at similar fields and temperatures and there may be a problem with those scans. There is a systematic dependence on temperature, where the scans at 4 K and 100 K have systematic different amplitudes than scan at 200 K and 290 K.*

From (5.16) the ratio of the hematite- SF to NSF intensity can be translated to the average angle of the hematite spins with respect to the the vertical, which is the direction of the applied field. This angle θ is displayed in fig. 9.4 as a function of the applied field. The spins start out at an angle of about 45° to the vertical and turn away from the field as it is increased, reaching an angle of about 60° at a 2 T field. As a function of temperature θ is increasing with a jump of a few degrees in going from 100 K to 200 K. Apart from two points that seem anomalous (same scans as the deviating points in fig. 9.3) the field-dependence is similar for all temperatures but the angle is generally about 3° larger for the 200 K and 290 K scans than for the scans at 4 K and 100 K.

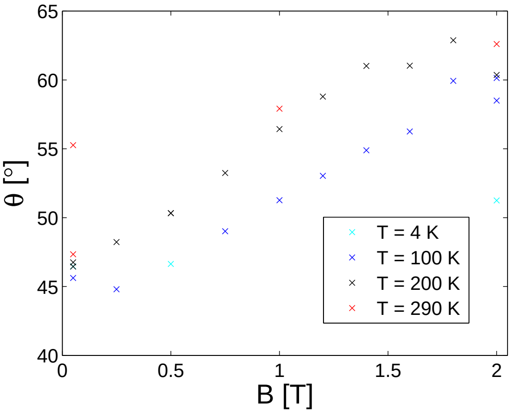

Figure 9.4: θ ***as derived from the*** $(00\bar{3})$ ***peak.*** *θ is the angle of the average spin orientation to the applied field, perpendicular to the scattering vector. The spins start out in an angle of about 45° and then rotate when the field is applied reaching an angle of about 60° at a field of 2 T. The angle increases more or less linearly with the field except for the two 'anomalous' points. If these points are disregarded the angles are systematically about 3 ° larger for the 200 K and 290 K scans than for the scans at 4 K and 100 K.*

Because of the obvious different spin angles at different temperatures the amplitudes as a function of temperatures are plotted for a few values of the applied field in fig. 9.5. The trend is that the SF amplitudes increase slightly with temperature, whereas the NSF amplitudes decrease with temperature.

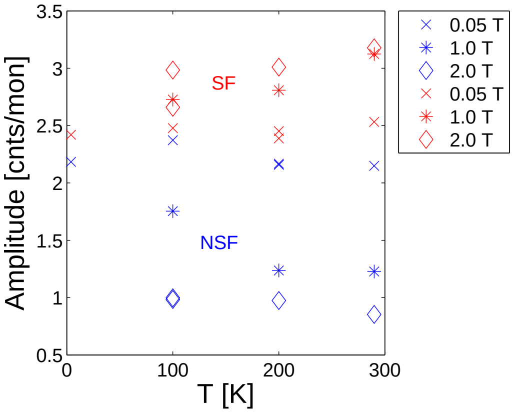

Figure 9.5: ***Temperature dependence of the fitted amplitudes at some selected fields.*** *The SF amplitude increase with temperature and the NSF amplitude decrease with temperature. The two anomalous scans are omitted. Errobars are same size as or smaller than the points.*

9.2 Results for the (101) peaks

Examples of the fit of the (101) peak at B = 0.05 T and B = 2 T is given in fig. 9.6. For a few scans the fit did not converge and these scans were omitted in calculating the average widths. The average widths were found to $\langle W_{\text{hem}} \rangle = 0.0094 \pm 0.0007\,\text{r.l.u.}$ and $\langle W_{\text{ilm}} \rangle = 0.0084 \pm 0.0004\,\text{r.l.u.}$ and after constraining the fit to these widths all fits converged.

The fitted amplitude of the SF peak is almost constant with field meaning that the amount of spins perpendicular to both the scattering vector and the polarisation does not change much with field. The amplitude of the ilmenite peak depends strongly on the magnetic field, indicating significant systematic errors. The field dependence of the ilmenite peak means that some of the scattering from the magnetic hematite reflection is interpreted by the fit as part of the ilmenite peak. This means that the fitted NSF hematite amplitude is not really a measure of the intensity of the magnetic reflection and it would be pointless to interpret anything from its intensity.

As for the $(00\bar{3})$ peak the (101) peak is not fitted excellently by the Gaussian fits. Both the SF and NSF peaks are slightly asymmetric. In the high-q end (the hematite end) of the NSF scans the data points deviate systematically from the fit.

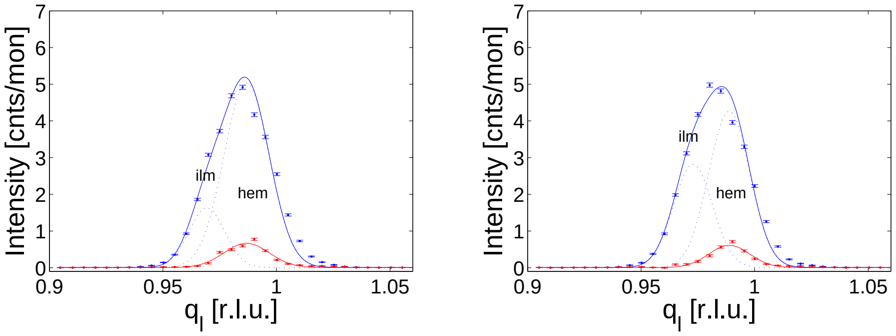

Figure 9.6: ***Scans of the (101) peak at T = 100 K: Left:*** *Intensity at B = 0.05 T and corrected with FR = 6.6.* ***Right:*** *B = 2 T and corrected with FR = 5.1. The red line is the SF fit. The dotted blue lines are the two NSF Gaussians and the solid blue line is their sum. The quality of the fits are represented by* $\tilde{\chi}^2_{NSF} = 64$ *and* $\tilde{\chi}^2_{NSF} = 12$ *and* $\tilde{\chi}^2_{SF} = 12$ *and* $\tilde{\chi}^2_{SF} = 9$*. The data is not well represented by the Gaussian fits and especially in the hematite end of the NSF peak the data deviate systematically from the fit. The amplitudes of the fit to the ilmenite peak are very different in the 0.05 T and 2.0 T scans, which is unexpected.*

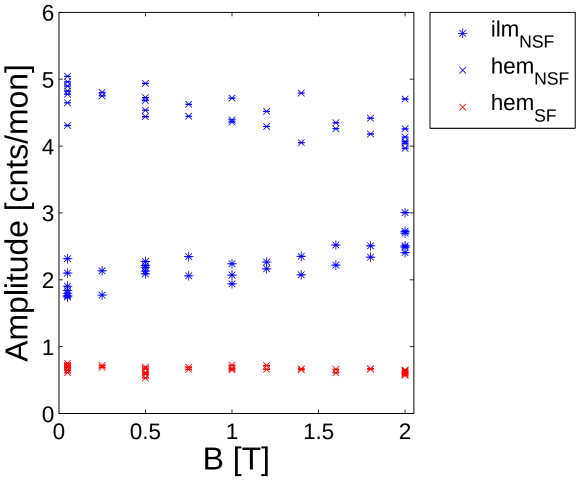

Figure 9.7: ***Amplitudes of the (101) peaks.*** *The amplitude of the structural ilmenite peak depends heavily on field, which is unphysical. Part of the NSF hematite intensity has clearly been picked up by the fit as part of the ilmenite signal and no of the fitted NSF amplitudes can thus be trusted. The SF amplitude, which is more or less constant is purely a signal from the magnetic hematite peak. The amplitudes of the hematite and ilmenite peaks can not be compared directly because the widths are different.*

9.3 Results for the $(10\bar{2})$ peaks

Examples of fits of the $(10\bar{2})$ peaks are shown in fig. 9.8. The average fitted widths are $\langle W_{hem} \rangle = 0.018 \pm 0.002\,\mathrm{r.l.u.}$ and $\langle W_{ilm} \rangle = 0.0156 \pm 0.0012\,\mathrm{r.l.u.}$.

While the small SF signals are fitted well with a Gaussian the NSF data once again deviate systematically from the fit in the hematite side of the peak. The SF amplitude is constant with field, while the amplitude of the ilmenite NSF peak increases with field and the hematite NSF amplitude decreases. Once again the only information that can be extracted from the NSF amplitudes is that the fit is not good enough.

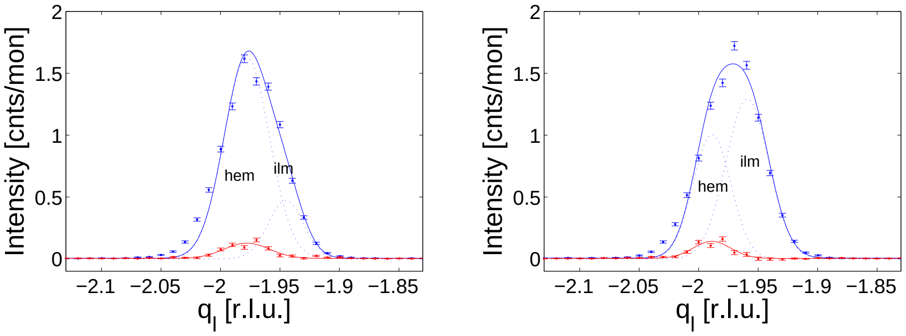

Figure 9.8: ***Scans of the $(10\bar{2})$ peak at $T = 100$ K: Left:*** *Intensity at B = 0.05 T and corrected with FR = 5.13* ***Right:*** *B = 2 T and corrected with FR = 6.6. The red line is the SF fit. The dotted blue lines are the two NSF Gaussians and the solid blue line is their sum. The quality of the fits are represented by $\tilde{\chi}^2_{NSF} = 21$ and $\tilde{\chi}^2_{NSF} = 15$ and $\tilde{\chi}^2_{SF} = 2.5$ and $\tilde{\chi}^2_{SF} = 1.7$. The NSF fits depends heavily on fieldThere clearly is a tail in the data on the hematite side of the NSF peak that is not well represented by the fit.*

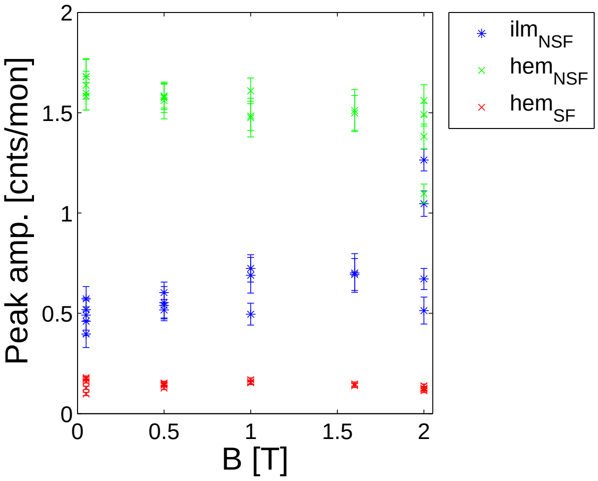

Figure 9.9: ***Amplitude of the (10$\bar{2}$) peaks.*** *The amplitude of the ilmenite NSF peak increases slightly, while the amplitude of the hematite NSF peak decreases slightly with field. The SF amplitude is constant. The amplitude of the ilmenite and hematite peaks can not be compared directly because the widths are different.*

9.4 Results for the $\left(10\frac{\bar{1}}{2}\right)$ peak

The antiferromagnetic $\left(10\frac{\bar{1}}{2}\right)$ ilmenite peak was scanned at a few temperatures below and above the Néel temperature (55 K). A few examples of such scans are given in figs. 9.10 and 9.11. Below T_N all the scattering is SF indicating that the spins are aligned perpendicular to the field. Above T_N the SF intensity has disappeared. A small NSF signal is present and is believed to be second order scattering from the structural ilmenite (20$\bar{1}$) reflection. This feature should be present below the Néel temperature as well, but is for unknown reasons not seen in the scans.

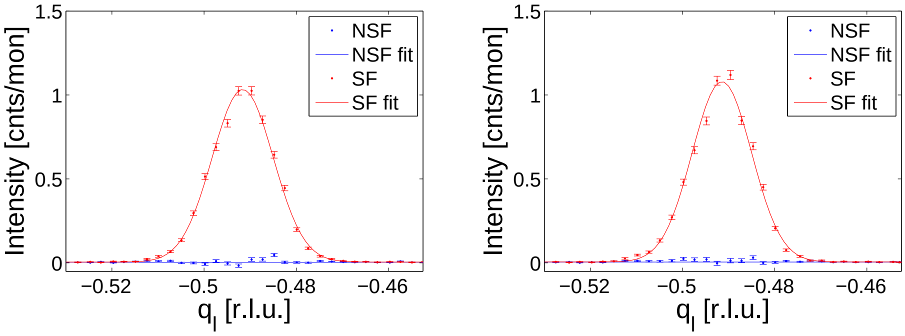

Figure 9.10: ***Scans of the ilmenite*** $\left(10\frac{\bar{1}}{2}\right)$ ***peak at*** $\boldsymbol{T = 4}$ ***K: Left:*** *Scan at* $B = 0.05$ *T,* $\tilde{\chi}^2 = 2.5$*.* ***Right:*** *Scan at* $B = 2$ *T,* $\tilde{\chi}^2 = 2.5$*. All the scattering is SF.*

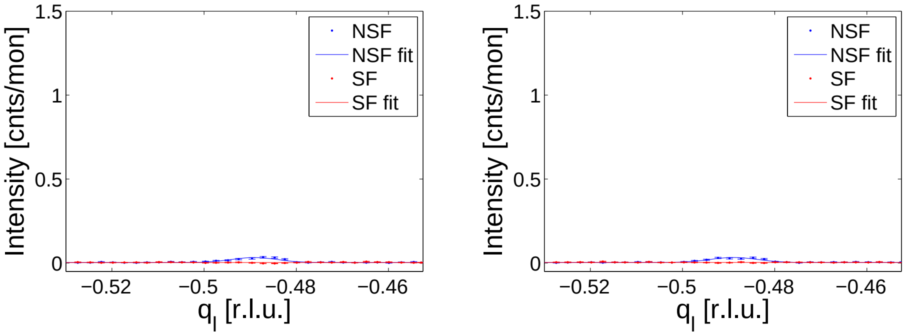

Figure 9.11: ***Scans of the ilmenite*** $\left(10\frac{\bar{1}}{2}\right)$ ***peak at*** $\boldsymbol{T = 200}$ ***K: Left:*** *Scan at* $B = 0.05$ *T.* ***Right:*** *Scan at* $B = 2$ *T. We are above the Neél temperature and the SF signal is gone. A small NSF signal is present.*

Chapter 10

The hemo-ilmenite experiment on SANS-I

A SANSPOL experiment on the hemo-ilmenite sample was performed in the summer of 2009, and in this chapter I will explain the setup of the experiment and how the experiment actually was performed. Because of the fixed deadline of this thesis I have not managed to dig deep into the analysis of the data from the experiment, but I will present some of the data and give a preliminary discussion of what we see in the data.

10.1 The experiment

The experiment was performed from july 23th to july 27th 2009 by Richard Harrison, Kim Lefmann and Erik Brok on the SANS-I instrument, PSI, of which a description can be found in section 7.5. The instrument was equipped with the Fe/Si supermirror polariser, that can be taken in and out of the beam in order to measure with polarised and unpolarised neutrons. The polarization axis is parallel to the beam. The sample was tied to an aluminium holder (see fig. 3.4) and aligned in the beam with the c-axis horizontal and the lamellae parallel to the beam. In summary, the geometry in the experiment was like in figure 10.1.

The sample was placed in a cryostat inside the field of an 11 T superconducting magnet. However, because of lack of time only measurements at $T = 290$ K were performed. Measurements were performed in fields in the range 0 T - 9 T. Unfortunately, no spin flipper was equipped in the experiment, so we could only measure with neutrons polarised in one direction and with unpolarised neutrons.

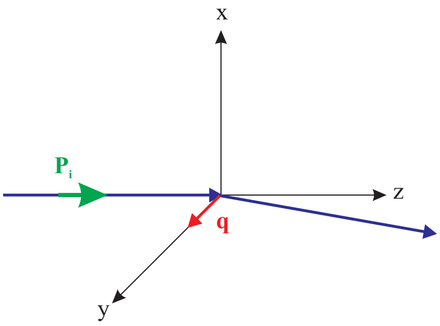

Figure 10.1: ***Geometry in the SANSPOL experiment.*** *The beam is parallel to the z- axis, which is also the polarisation axis. The scattering vector is along the y axis, and the (001) plane of the lamellae is in the x-z plane. The applied field is along the z-axis.*

In all but a very few measurements, neutrons with $\lambda = 5$ Å were used. A few $\lambda = 8$ Å measurements were also performed to extend the q-range, but suffered from larger absorption in the sample. In order to get both high and low q-values detector distances of 2 m, 6 m and 18 m and a range of suitable collimation settings (mostly 3 m, 8 m and 15 m) was used. These collimation lengths were used to optimize the flux on the sample and the divergence. Detector distances shorter than 2 m could not be used in the experiment.

Without the spin flipper we could not directly study the difference between I^+ and I^- and we therefore decided to measure with polarised and unpolarised neutrons in all data points to make it possible to take the difference between I^0 and I^+. We would thus get the same information as we set out to, but the difference signal would be halved.

Unfortunately, the measurements turned out not to have a good reproducibility. The irreproducibility when moving the polariser in/out of the beam was of the order of 0.5%, which is unfortunate when we want to measure a small magnetic signal in the background of a large structural signal (see fig. 10.3). In the remainder of the experiment we therefore measured differences within the same configuration with polariser on, only changing the field.

Examples of the measurements are displayed in fig. 10.2. The beam-stop is seen in the middle and the scattering from the sample stretches horizontally. The effect of the lamellae is clearly seen, especially for low q (larger lamellae), where the scattering is most anisotropic.

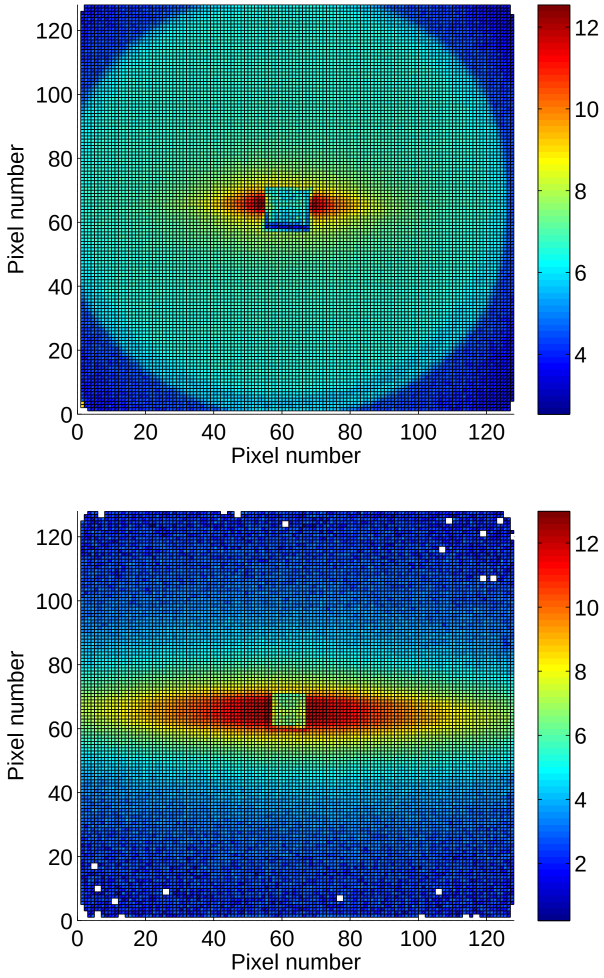

Figure 10.2: ***SANSPOL data from the PSD at B = 9 T. Top:*** *High q measurement, dt = 2 m and coll = 3 m.* ***Bottom:*** *Low q measurement, dt = 18 m and coll = 15 m. The beam-stop is in the center. The asymmetric scattering pattern is the signature of the lamellae and is most distinct in the low q measurement. The data is corrected for the detector efficiency. The plot is in logarithmic scale*

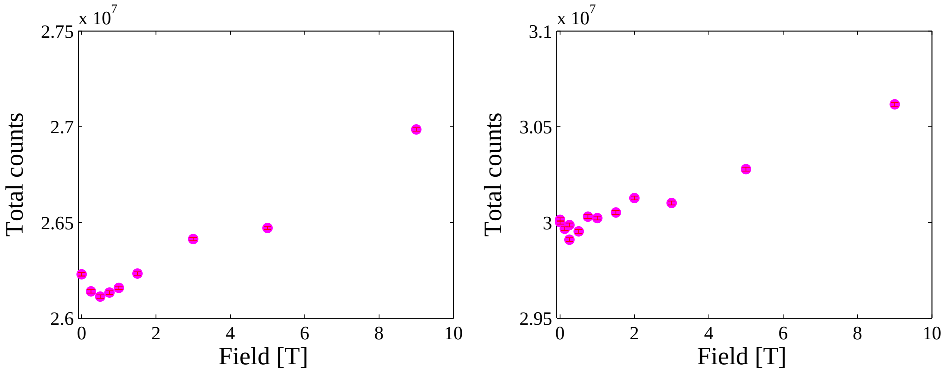

Figure 10.3: ***Total counts on the PSD. Left:*** *High q data, dt = 2 m, coll = 3 m. The total number of counts on the PSD decreases for fields up to 0.5 T and then increases monotonously.* ***Right:*** *Low q data, dt = 18 m, coll = 15 m. The variations in the low field data are large, but there may be a decrease in the signal at low fields. For larger fields the number of counts increases.*

The total number of counts on the PSD as a function of field (see fig. 10.3) gives an idea about the magnetic signal from the system. For the high q measurements (dt=2) the intensity decreases in fields up to about 0.5 T and then increases monotonously up to the maximal field of 9 T. The magnetization of the ilmenite can be expected to produce a signal that is linear with field. If the 'jump' between 3 T and 5 T is ignored the slope of the curve is constant and the linear magnetization is probably what we see. The difference between 3 T and 5 T is probably because of the irreproducibility of the signal, perhaps a slight movement of the sample. For the high q measurements the trend is less clear because of large irreproducibilities, but at least the linear magnetization of ilmenite seems to be followed.

In order to compare with the model of section 6.2 the q_x-dependence of the data is fitted with a Gaussian in the vertical direction on the PSD and the amplitude of the Gaussian is plotted against the q_y-value. This is displayed for a field of 9 T in fig. 10.4. The low q data resembles the Guinier behaviour (6.14), whereas the higher q data (the part where the curve is linear) resembles the behaviour described by the Porod law (6.15). The high q data ($q > 0.1$ Å^{-1}) shows interesting features which are presently not understood. There are clearly possibilities in the analysis of the SANSPOL data but in the rest of this thesis I will concentrate on discussing the presented results from the TASP and SANS-I experiments.

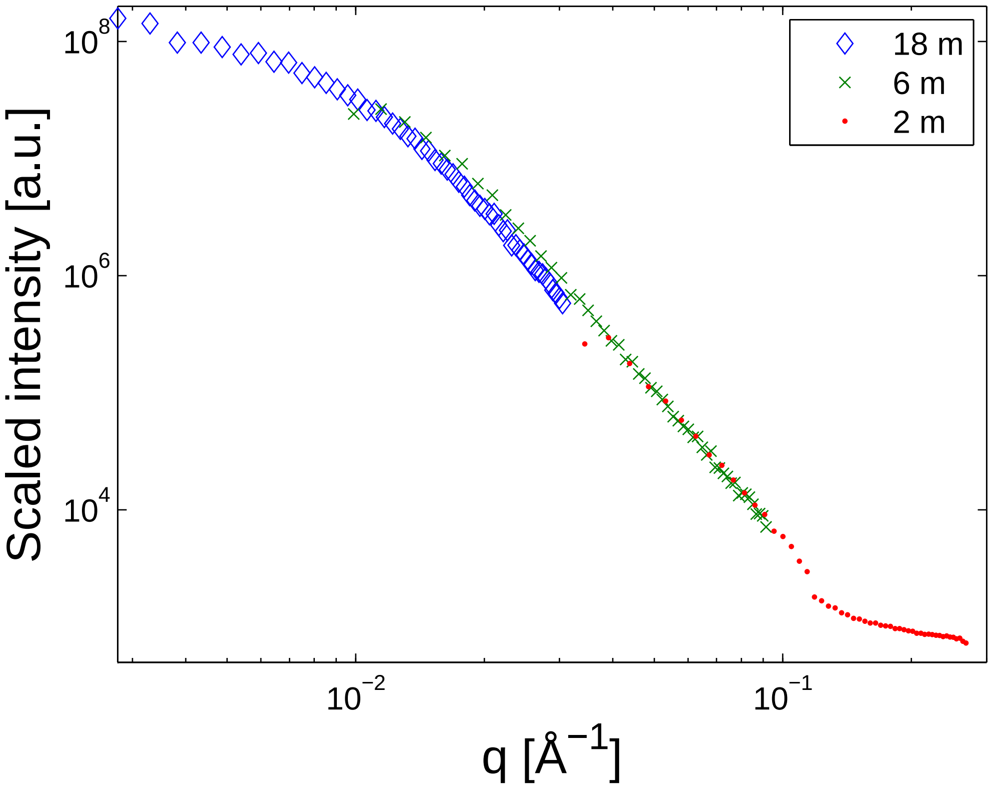

Figure 10.4: ***Intensity vs*** *q_y. The intensities are obtained from Gaussian fits across the PSD in the x-direction as explained in the text. The measurements are taken with polarised neutrons meaning that the intensity is the one refered to as I^+ in the models of section 6.2. The intensities of the measurements at 6 m and 18 m detector distance are scaled to match that of the 2 m data.*

Chapter 11

Discussion

In general, the analysis of the TASP data was complicated both because of the nature of the sample and the way the experiment was performed. Because of the similar lattice constants for hematite and ilmenite, the structural peaks from the ilmenite were difficult to resolve from the magnetic peaks from hematite. The hematite peaks are not as well represented by the Gaussian fits as the ilmenite peaks. In some scans it clearly seems like the hematite peak has a tail extending away from the Gaussian. This could be because the broad size distribution of the lamellae includes nano-sizes giving a broadening of the peak that is not Gaussian.

Because of the uniaxial anisotropy, the hematite spins are confined to the basal plane (except for perhaps a tiny out of plane canting) and are therefore perpendicular to the $(00\bar{3})$ scattering vector. This means that for this reflection $\mathbf{M}_{\perp}(\mathbf{q}) = \mathbf{M}(\mathbf{q})$ and the total spins are seen rather than just a projection. The c-axes of hematite and ilmenite differ more than does their in-plane axes, meaning that the separation between the two $(00\bar{3})$ peaks are better than for the (101) peaks. This means that the best way to get information about the directions of the hematite spins is from the $(00\bar{3})$ peak.

The first observation when analysing the $(00\bar{3})$ data was that there are two scans that deviate from the rest. Their amplitudes are very different from scans at similar (in one case the same) temperatures and fields. By inspection it is verified that the difference is in fact in the scans and not in the fitting. There is no obvious explanation of these anomalous points. One explanation could be that a false value of the applied field was noted in the log, but this has been controlled and is not the case. The anomalous point at 0.05 T could be explained by a hysteresis effect, since the measurements just before the anomalous one was in high fields. However, this seems unlikely since we do not see the hysteresis effect at other temperatures. The point at 2 T was one of the earliest scans in the experiment and may have been performed under slightly different experimental conditions because of the incident where the polarisation guide was moved by the field. The scan might therefore have been done with a slightly different flipping ratio.

The measured broadening of the hematite peak gives an average size of the lamellae of 44 nm in the c-direction, which is consistent with observations from microscopy [2] [1]. However, as the broadening is found from the Gaussian fits which does not represent the data perfectly the value may not be accurate.

The data from the SANSPOL experiment is not fully analysed yet. The absence of a spin flipper in the experiment means that we were unable to take the difference between I^+ and I^-. Further the irreproducibility in the experiment when taking the polariser in/out of the beam meant that we were also unable to take the difference between I^+ and an unpolarised beam (I^0). We still have the possibility to take differences between measurements at different fields in order to get information about the magnetic structure. This possibility has not been pursued yet, but I expect the irreproducibility in the experiment to be a problem. It would be interesting to do a new SANSPOL experiment with a spin flipper equipped.

In the further analysis of the SANSPOL data the q-dependence of the intensity should be investigated and especially the high q end could give information about the magnetization of the lamellae.

11.1 Field- and temperature-dependence

The field-dependence in the $(00\bar{3})$ ilmenite peak could be a physical effect, but may as well be ascribed to systematic errors in the experiment and the data analysis. The increasing intensity in the ilmenite can not be caused by magnetization of the PM ilmenite since it does not depend on temperature.

The most significant information we can draw from the (101) scans is that the SF amplitude does not change noticeably with field or temperature. This means that the amount of spins perpendicular to both the field and the scattering vector is constant. From scans of the much stronger $(00\bar{3})$ hematite reflection the average direction of the hematite spins are found to start out at an angle close to 45° for the low applied field of 0.05 T and rotate away from the field as it is increased, reaching an average angle of about 60° at a 2 T field. It is unclear whether the system is beginning to saturate at 2 T. The average orientation of the spins in the basal plane is seen in the $(00\bar{3})$ scans, whereas the (101) SF scans gives the projection of these perpendicular to the (101) scattering vector and the field. (Plus perhaps a component from canting in the c-direction, but this is extremely small). The observations from the (101) and $(00\bar{3})$ magnetic hematite peaks does thus not agree well. A probable explanation is that the flipping ratio used for the correction is not correct. A small change in FR would change the small NSF signal in the (101) peak significantly and could explain the differing observations. The $(00\bar{3})$ peak is believed to be the most reliable because the intensity is larger and because an erroneous FR value would be less significant here.

Scans of the $(10\bar{2})$ peak show that there is a constant magnetic contribution in the structural hematite peak. Because the signal is present at the position of the structural peak it is ferromagnetic in type. This is an important observation, because it may be a direct observation of the moment responsible for the remanent magnetization. The SF signal is constant with field, which means that the spins that make up the ferromagnetic signal are either unaffected by the 2 T field or that they are already fully rotated at the 0.05 T field. This observation does not agree well with bulk measurements of the hysteresis, which indicates that the magnetization of the sample should saturate somewhere around 0.5 T. Once again is seems probable the data is corrected with a wrong value of the FR and this is probably the reason that a rotation of the spins is not seen. If an other (the true) value of the FR was used the signal would depend on the applied field and the rotation of the moments could be investigated. This would give a hint of the origin of the ferromagnetic moment. The ferromagnetic signal can not come from moments in the contact layers between lamellae since such a signal would not show up in the structural peaks.

There is no evidence of a Morin transition in the system since this would be seen as simultaneous drops in the SF and NSF amplitudes of the magnetic $(00\bar{3})$ peaks when lowering the temperature. It can be assumed that some Ti is present in the hematite and we also know that there are finite size effects in the system. As discussed in section 2.4 both are known to suppress the Morin transition and the absence of the transition is therefore reasonable.

Scans of the ilmenite $\left(10\frac{\bar{1}}{2}\right)$ peak show that the ilmenite is AFM ordered at $T = 4$ K and not at $T \geq 100$ K, which is consistent with a Néel temperature of $T_N \approx 55$ K as measured by others [15]. No NSF signal is observed indicating that there is no canting in ilmenite in the direction of the field. The small NSF signal for larger temperatures is believed to be second order scattering from the $(20\bar{1})$ structural ilmenite peak and should be present in all $\left(10\frac{\bar{1}}{2}\right)$ scans. We do not see the signal below T_N and this may indicate that some other effect is in play. It could be explained by a weak magnetic signal from a magnetic ordering with same period as the magnetic order in

AFM ilmenite, but with spins in the direction of the field. The absence of the peak for low fields could also be explained by the polarisation correction. Under the Néel temperature the second order signal would only be a very small contribution on top of a much larger signal from the AFM scattering. In fact the errorbars on the AFM signal is of the same size as the second order signal for higher temperatures and it thus seems likely that the signal is lost in the FR Correction.

The temperature dependence of the magnetic $(00\bar{3})$ amplitudes show that there is a difference in the spin directions of a few degrees between temperatures of 100 K and 200 K. A similar trend is seen in the (101) scans. I have no good explanation for this effect, but note that in the experiment the scans were performed in 'temperature order', meaning that the effect could be because of the history in the experiment. -Perhaps something uncontrolled happened in the experiment or in the sample right around the time of changing from 100 K scans to 200 K scans. If the effect does not originate from experimental errors but is a real effect of the sample it gives a hint of the energy range for turning the spins. (energy comparable to $200\mathrm{K} \cdot k_B$)

11.2 Origin of the moment?

CAFM hematite moments are expected to align with the AFM sublattice directions perpendicular to the field and the small canting moment along the field (see fig. 11.1) whereas a lamellar moment is expected to align with the field. For a system where the only spins are those of CAFM hematite the spins would be expected to start out at an average angle of 45° to the field and gradually rotate to an angle close to 90° (provided the canting is small). This model is consistent with the observations from the diffraction experiment (TASP). For a system with only lamellar moments the moments would also be expected to start out with an average angle of 45° to the field, but the net moments in the lamellae would make the lamellar moments align with the field and the angle should decrease. This is in contrast with the observations.

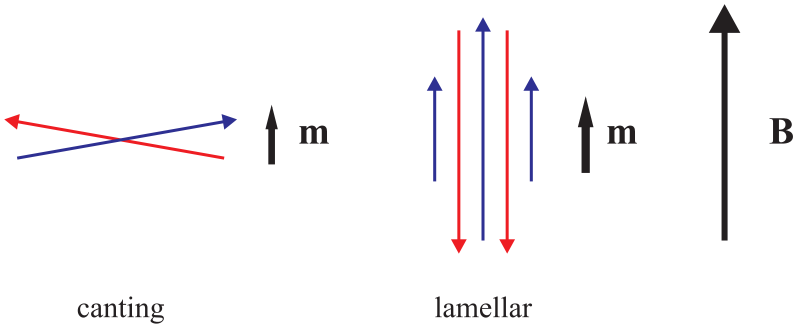

Figure 11.1: ***Canted and lamellar moments align with the applied field.*** *The blue and red spins are in alternating Fe^{3+} cation layers. The CAFM heamtite moments are expected to align with the canting moment along the field and the AFM sublattice directions perpendicular to the field. Lamellar moments are expected to align with the net lamellar moment and the AFM sublattice directions parallel to the field.*

However, in hysteresis measurements on similar samples the magnetization starts to saturate at fields of around 0.5 T, while in our diffraction experiment the spins continue to rotate until an applied field of at least 2 T. This indicates that the rotating spins we are measuring in the diffraction experiment are not the same as the ones that saturate in the hysteresis measurements. The reason is probably that in the hysteresis measurements the small lamellae with relatively most uncompensated lamellar moments are seen, whereas the diffraction experiment mainly sees the larger lamellae because they take up most of the sample volume.

In the SANSPOL experiment we see a decrease in the total intensity for fields up to about 0.5 T followed by an linearly increasing signal from the magnetization of the ilmenite. This decreasing intensity for 0 - 0.5 T fields could be a signature of the same hysteresis as in the bulk measurements. In the SANSPOL experiment the signal comes from the average scattering length density over a few unit cells, meaning that the AFM order of the hematite is not seen. The magnetic signal therefore comes from an average magnetization and it seems very likely that it is the same one as in the bulk measurements.

Chapter 12

Summary and outlook

From the experiments some interesting conclusions about the magnetic structure of the hemo-ilmenite sample can be drawn. It was established that there is a ferromagnetic signal from the hematite that does not originate from moments in contact layers. The rotation of the AFM hematite spins was away from the field and there was no observation of saturation at fields up to 2 T. This is not in agreement with a model that is dominated by lamellar magnetism, but could be explained by canting of the hematite moments. The lamellar magnetism hypothesis, as presented in [4] and [6], can not explain the data alone. The canting of the hematite spins has to be taken into account and could be an important contributor to the magnetization of the natural samples.

The SANSPOL experiment shows a hysteresis that saturates at a field of around 0.5 T which is similar to observations in bulk measurements [1]. This hysteresis signature is most prominent at high q which indicates that it is associated with the smallest of the lamellae. This signal is probably the scattering from the magnetic structures that make up the magnetization of the sample and could hence be important for the understanding of the NRM.

A model where both canting and lamellar magnetism is important may be the explanation for the magnetic properties of hemo-ilmenite. The diffraction signal shows the rotation of the CAFM spins whereas the SANSPOL signal may be a signature of the lamellar magnetism.

Because of the rather poor resolution in the TASP experiment it was nearly impossible to separate the close lying ilmenite and hematite peaks meaning that the amount of information that could be extracted from the data was limited. The fact that there was no good way to obtain the polarisation in the experiment from the data was a problem that may have introduced systematic errors in the data analysis.

12.1 Outlook

It would be interesting to perform a new polarization analysis experiment on the same sample with better resolution than in the present experiment and with a better control of the polarisation. The scattered intensity from the sample is high, so the experiment could be done in a few days. With better resolution and knowledge about the experimental FR it should be possible to make more firm conclusions and to answer some of the remaining open questions. It would be very interesting to measure the spin directions in higher fields and try to determine the saturation angle of the hematite spins. This could give important information about the amount of canting- and lamellar moments in the system.

With better resolution, the hematite and ilmenite peaks would be well separated and a more thorough analysis of the signal could begin. If a model that fitted the hematite peaks better than the Gaussian was used it should be possible to extract further information about the lamellae. For example, by following the field dependence of the Lorentzian-like tail on the hematite peak, one might get information about whether or not the very small lamellae responds differently to applied field, than do the larger bulky ones. It would also be interesting to see whether the temperature dependence of the spin directions found in the TASP experiment was reproduced.

In order to understand the magnetic properties of the system, the actual size distribution of the lamellae would be interesting to determine. This could also be a help for data analysis in future experiments. It should be possible to get information about the size distribution from the SANS data.

On the background of results from the present SANSPOL experiment a new experiment with a spin flipper seems very promising. In order to get information about the magnetic structures that makes up the magnetization of the sample the experiment should concentrate on fields below 1 T and high q values. A spin flipper can be equipped on SANS-I together with a 1 T electromagnet, which should be ideal for the experiment.

Strain along the c-axis in the lamellae might be very important for the magnetic properties and it would therefore be valuable to have information about the degree of strain in the system. The strain could be determined by hard synchrotron x-ray diffraction to high q values, at least out to $(00\bar{1}2)$.

Combining all these informations, one could hope to answer the puzzle of the large magnetization of hemo-ilmenite.

Appendices

Appendix A

Structure of ilmenite and hematite

h	k	l	j	F^2	q [Å^{-1}]
0	0	3	2	3758.56	1.2689
1	0	1	6	691.654	1.48725
1	0	-2	6	841.331	1.65789
1	0	4	6	240.165	2.21256

Table A.1: ***Structural reflections of ilmenite.*** *As calculated by Bente Lebech in the Crystallographica programme. I quote the first few reflections only. Here j is the multiplicity of the reflection and F is the structure factor.*

h	k	l	j	F^2	q [Å^{-1}]
1	0	-2	6	1599.49	1.70483
1	0	4	6	7669.61	2.32469

Table A.2: ***Structural reflections of hematite.*** *As calculated by Bente Lebech in the Crystallographica programme. I quote the first few reflections only. Here j is the multiplicity of the reflection and F is the structure factor.*

Appendix B

Gauss distribution

The definition of a Gaussian distribution is:

$$G(x) = Ae^{\frac{(x-C)^2}{2\sigma^2}}. \tag{B.1}$$

The width W at full width half maximum is related to the standard deviation σ by:

$$W = 2\sqrt{2\ln 2}\,\sigma \tag{B.2}$$

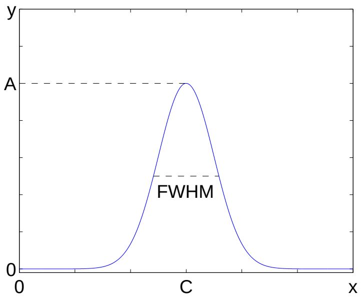

Figure B.1: ***Gaussian distribution.*** *The amplitude A, center C, and the width at falf maximum, FWHM is marked.*

Appendix C

Resolution parameters for RESCAL

The parameters needed to calculate the resolution function in the TASP experiment with the Rescal programme [37]. The parameters are named as in Rescal. Table C.1 are the sample parameters, collimation parameters and other parameters to be read in to the 'Parameters' window in Rescal. The parameters for the specific scan is for a scan of the (003) reflection and should be changed if the resolutin function is to be calculated at other positions in q-space. In table C.2 are the parameters to be read in to the 'Instrument' window of Rescal.

DM	3.354	DA	3.354	ETAM	40.000	ETAA	40.000
ETAS	120.000	SM	-1.000	SS	1.000	SA	-1.000
KFIX	1.553	FX	2.000	ALF1	80.000	ALF2	80.000
ALF3	80.000	ALF4	80.000	BETA1	400.000	BETA2	400.000
BETA3	400.000	BETA4	400.000	AS	5.038	BS	5.038
CS	13.772	AA	90.000	BB	90.000	CC	120.000
AX	1.000	AY	0.000	AZ	0.000	BX	0.000
BY	0.000	BZ	1.000	QH	0.000	QK	0.000
QL	2.950	EN	0.000	DH	0.000	DK	0.000
DL	0.010	DE	0.000	GH	0.000	GK	0.000
GL	1.000	GMOD	1.000				

Table C.1: ***Values of the Rescal 'parameters' variables***

1.000	% =0 for circular source, =1 for rectangular source
3.500	% width/diameter of the source (cm)
10.000	% height/diameter of the source (cm)
1.000	% =0 No Guide, =1 for Guide
10.000	% horizontal guide divergence (minutes/Angs)
10.000	% vertical guide divergence (minutes/Angs)
1.000	% =0 for cylindrical sample, =1 for cuboid sample
1	% sample width/diameter perp. to Q (cm)
1	% sample width/diameter along Q (cm)
1	% sample height (cm)
1.000	% =0 for circular detector, =1 for rectangular detector
3.500	% width/diameter of the detector (cm)
17.000	% height/diameter of the detector (cm)
0.300	% thickness of monochromator (cm)
15.000	% width of monochromator (cm)
13.000	% height of monochromator (cm)
0.300	% thickness of analyser (cm)
15.000	% width of analyser (cm)
15.000	% height of analyser (cm)
100.000	% distance between source and monochromator (cm)
130.000	% distance between monochromator and sample (cm)
90.000	% distance between sample and analyser (cm)
70.000	% distance between analyser and detector (cm)
0.000	% horizontal curvature of monochromator 1/radius (cm-1)
0.013	% vertical curvature of monochromator (cm-1)
0.078	% horizontal curvature of analyser (cm-1)
0.000	% vertical curvature of analyser (cm-1)

Table C.2: ***Values of the Rescal 'Instrument' variables***

Bibliography

[1] S.A. McEnroe et al., Journal of Physics, Conference Series 17 (2005) 154.

[2] S.A. McEnroe, P. Robinson and P.T. Panish, American Mineralogist 86 (2001) 1447.

[3] S.A. McEnroe et al., Geophysical Research Letters 31 (2004) L19601.

[4] P. Robinson et al., Nature 418 (2002) 517.

[5] S. Blundell, Magnetism in Condensed Matter (Oxford University Press, 2001).

[6] P. Robinson et al., American Mineralogist 89 (2004) 725.

[7] A.H. Morrish, Canted Antiferromagnetism: Hematite (World Scientific, Singapore, 1994).

[8] P.J. Flanders, Journal of Applied Physics 43 (1972) 2430.

[9] F.J. Morin, Physical Review 78 (1950) 819.

[10] Y. Bando et al., Journal of the Physical Society of Japan 20 (1965) 2086.

[11] N. Yamamoto, Journal of the Physical Society of Japan 12 (1957) 1083.

[12] S.N. Klausen et al., Physical Reviev B 70 (2004).

[13] G. Shirane et al., J. Phys. Chem. Solids 10 (1959) 35.

[14] Y. Yamaguchi et al., Solid State Communications 59 (1986) 865.

[15] Y. Ishikawa and S. Akimoto, Journal of the Physical Society of Japan 24 (1968) 23.

[16] C. Frandsen et al., Geophysical Research Letters 34 (2007).

[17] P. Robinson et al., Geophys J. Int. 165 (2006) 17.

[18] R. Harrison, Personal communication, 2009.

[19] D.J. Dunlop and . Özden Özdemir, Rock Magnetism (Cambridge University Press, Singapore, 1997).

[20] K. Lefmann, Neutron Scattering: Theory, Instrumentation and Simulation (Copenhagen University, Copenhagen, 2008).

[21] G.L. Squires, Introduction to the Theory of Thermal Neutron Scattering (Cambridge University Press, Cambridge, 1978).

[22] J. Chadwick, Nature 129 (1932).

[23] Homepage of the Paul Scherrer Institut: http://www.psi.ch/.

[24] R.L. Liboff, Intrudoctory Quantum Mechanics, 8th ed. (Addison Wesley, San Francisco, 2003).

[25] C. Kittel, Introduction to Solid State Physics, 8th ed. (John Wiley and Sons, Inc., Hoboken, NJ, 2005).

[26] M. Blume, Physical Review 130 (1963) 1670.

[27] R.M. Moon, T. Riste and W.C. Koehler, Physical Review 181 (1969) 920.

[28] R. Pike and P. Sabatier, Scattering: Scattering and inverse scattering in pure and applied science (Academic Press, 2002).

[29] B.N. Brockhouse, International Atomic Energy Agency (Vienna 1961) 113.

[30] G. Shirane, S.M. Shapiro and J.M. Tranquada, Neutron Scattering with a Triple-Axis Spectrometer (Cambridge University Press, Cambridge UK, 2002).

[31] Homepage of TASP: http://spectroscopy.web.psi.ch/tasp/.

[32] P. Böni and P. Keller, PSI Procedings 02 (1996) 35.

[33] Homepage of SANS-I: http://kur.web.psi.ch/sans1/.

[34] J. Kohlbrecher and W. Wagner, Journal of Applied Crystallography 33 (2000) 804.

[35] V.K. Aswal et al., Nuclear Instruments and Methods in Physics Research A 586 (2008) 86.

[36] B.E. Warren, X-Ray Diffraction (Dover, 1990).

[37] MATLAB homepage of ILL: http://www.ill.eu/instruments-support/computing-for-science/cs-software/all-software/matlab-ill/.

[38] E. Farhi, Personal communication, 2009.

[39] B.A. Wechsler and C.T. Prewitt, American Mineralogist 69 (1984) 176.